ACADEMIC
PRESS

Spin exchange interactions and magnetic structures of extended magnetic solids with localized spins: theoretical descriptions on formal, quantitative and qualitative levels

Myung-Hwan Whangbo,* Hyun-Joo Koo, and Dadi Dai

Department of Chemistry, North Carolina State University, Raleigh, NC 27695-8204, USA

Abstract

Low-energy excitation energies of a magnetic solid with localized spins are probed by magnetic susceptibility, neutron scattering and Raman scattering measurements, and are analyzed using a spin Hamiltonian with a set of spin exchange parameters. The nature and values of the spin exchange parameters deduced from this analysis depend on what spin exchange paths one includes in the spin Hamiltonian. In this article, we review how spin exchange interactions of magnetic solids with localized spins are described on formal, quantitative and qualitative theoretical levels, investigate antisymmetric and anisotropic interactions for general spin dimers, and discuss the spin exchange interactions and magnetic structures of various extended magnetic solids on the basis of spin dimer analysis. Strongly interacting spin exchange paths of a magnetic solid are determined by the overlap between its magnetic orbitals, so that the strongly interacting spin unit of a magnetic solid does not necessarily have the same geometrical feature as does the arrangement of its magnetic ions or spin-carrying molecules. Therefore, in interpreting results of magnetic susceptibility, inelastic neutron scattering or Raman scattering measurements, it is essential to employ a set of spin exchange parameters chosen on the basis of proper electronic structure considerations. Spin dimer analyses based on extended Hückel tight binding calculations provide a reliable and expedient means to study the relative strengths of superexchange and super-superexchange spin exchange interactions.
© 2003 Elsevier Inc. All rights reserved.

Keywords: Magnetic solids; Spin exchange interactions; Magnetic structures

1. Introduction

A magnetic solid with localized spins has low-lying excited states resulting from their weak interactions. The low-energy excitation energies associated with these magnetic states are probed by performing magnetic susceptibility, inelastic neutron scattering or Raman scattering measurements. In magnetic susceptibility experiments, which are carried out as a function of temperature under a probing magnetic field, the low-energy excitation energies are deduced indirectly by studying the temperature dependence of the Boltzmann populations of the low-lying excited states. In inelastic neutron scattering and Raman scattering experiments, the low-energy excitation energies are detected directly by measuring the energies of the inelastically scattered neutrons and photons, respectively. Inelastic neutron scattering measurements are carried out at very low temperatures (e.g., 10–15 K) to avoid complications resulting from inelastic neutron–phonon interactions. In Raman scattering experiments, both magnetic and vibrational excitations occur so that it is necessary to identify the peaks of magnetic excitations from a resulting Raman spectrum, for which the magnetic excitation energies observed from magnetic susceptibility or inelastic neutron scattering measurements are invaluable.

To determine the nature and strengths of the interactions between localized spins in a magnetic solid, results of magnetic susceptibility, inelastic neutron scattering and Raman scattering experiments are analyzed in terms of a Heisenberg spin Hamiltonian $\hat{H}$, which is written as a sum of bilinear isotropic spin exchange interactions between adjacent spin sites i and j, $J_{ij}\hat{S}_i \cdot \hat{S}_j$, where $\hat{S}_i$ and $\hat{S}_j$ are the spin operators

*Corresponding author. Fax: +1-919-515-7832.
E-mail address: mike_whangbo@ncsu.edu (M.-H. Whangbo).

at the sites i and j, respectively, and J_{ij} is the spin exchange parameter. This phenomenological Hamiltonian expresses excitation energies of a magnetic solid in terms of a set of spin exchange parameters J_{ij}. Thus in analyzing experimental results in terms of $\hat{H}$, the spin exchange parameters J_{ij} become numerical fitting parameters needed to reproduce the experimental results. The nature and values of these "experimental" J_{ij} parameters depend on what spin exchange paths one includes in the spin Hamiltonian, and more than one set of J_{ij} values can lead to an equally acceptable fitting. It is essential to examine the electronic structure of a magnetic solid to obtain a meaningful set of spin exchange parameters.

Concerning how the signs of spin exchange interactions depend on the electronic structures of the spin exchange paths, qualitative relationships were first developed by Goodenough [1], and were extended by Kanamori [2]. On the basis of electronic structure considerations, Anderson [3] laid a theoretical foundation for describing bilinear isotropic spin exchange interactions. Certain physical phenomena of magnetic solids are not explained in terms of isotropic spin exchange interactions alone. To explain these phenomena, Moriya [4] introduced antisymmetric and anisotropic interactions between spins. A more general treatment of isotropic, antisymmetric and anisotropic interactions was given by Erdös [5]. Some compounds have negligible antisymmetric and anisotropic interactions but their magnetic properties are not well explained in terms of bilinear isotropic interactions alone. For such instances it was found necessary to include biquadratic interactions between spins [6]. A general description of biquadratic interactions was given by Griffith [7].

Over the years a number of studies [8–13] have investigated how isotropic spin exchange interactions described by Heisenberg Hamiltonians are related to the electronic structures of magnetic systems. Through these studies, it became possible to think about spin exchange interactions in terms of qualitative chemical concepts such as overlap and orbital interaction [8,9]. They also made it possible to calculate quantitatively the strengths of spin exchange interactions using state-of-art electronic structure computations on the basis of either the configuration interaction (CI) wave function or the density functional theory (DFT) method [14–23].

In choosing a correct set of spin exchange paths to analyze experimental data and hence correctly explaining the physical properties of a magnetic solid, it is sufficient to know the relative strengths of its spin exchange interactions. In a magnetic solid of transition metal ions M whose first coordinate spheres are made up of main group ligand atoms L, spin exchange interactions between adjacent metal ions may take place through $M-L-M$ superexchange (SE) paths or $M-L\cdots L-M$ super-superexchange (SSE) paths. The relative strengths of SE interactions can be guessed using Goodenough rules [24] in terms of the $\angle M-L-M$ angle, the symmetry properties of the metal d-orbitals containing unpaired spins, and the number of unpaired spins at the metal site M. There have been no such qualitative rules for predicting the relative magnitudes of SSE interactions. As a result, in assigning strongly interacting spin exchange paths of a magnetic solid, SSE interaction paths have often been neglected, and the assignment has been guided by the ease and/or the novelty of the eigenvalue problem the supposed spin lattice generates. Consequently, as exemplified by the studies of vanadyl pyrophosphate $(VO)_2P_2O_7$, the magnetic properties of a magnetic system can be explained in terms of a spin lattice model totally irrelevant for the system [25,26]. Therefore, it is essential to assign spin lattices of magnetic solids with the help of appropriate electronic structure considerations because a SSE interaction can be stronger than any SE interaction [26–28]. Our studies [26] on numerous magnetic solids have shown that one can estimate the relative strengths of SE and SSE interactions almost semiquantitatively using spin dimer analyses based on extended Hückel [29] tight-binding (EHTB) electronic structure calculations (see Section 6).

As discussed above, theoretical studies of magnetic solids include three important components, namely, studies of the eigenvalue structures of spin Hamiltonians, quantitative calculations of spin exchange interactions in terms of first-principles electronic structure computations, and qualitative estimations of the relative strengths of spin exchange interactions using semi-empirical electronic structure calculations. In this work we will review the essential issues concerning these three aspects of theoretical studies, present results of our investigation on antisymmetric and anisotropic interactions for general spin dimers, and review the spin exchange interactions and magnetic structures of various magnetic solids probed by spin dimer analyses using EHTB calculations. For early reviews, the readers are referred to the articles of Ginsberg [30], Griffith [7], and Hatfield [31] as well as the monographs of White [32], Bencini and Gatteschi [33], and Kahn [34].

Our work is organized as follows: Section 2 examines isotropic spin exchange interactions described by Heisenberg Hamiltonians. In Section 3 we investigate in some detail antisymmetric and anisotropic interactions for general spin dimers, and briefly discuss biquadratic interactions. Section 4 probes how spin exchange parameters are determined quantitatively using first-principles electronic structure calculations. The question of how to describe trends in spin exchange interactions on a qualitative level is probed in Section 5. In Section 6 we discuss the strengths and weaknesses of EHTB electronic structure calculations. In Section 7 we discuss the spin exchange interactions and magnetic

structures of various extended magnetic solids on the basis of spin dimer analyses using EHTB calculations. Finally, we summarize our conclusions in Section 8. Important results of our investigation on antisymmetric and anisotropic interactions are summarized in Appendix A, B, C.

2. Spin states and spin Hamiltonians

Spin exchange interactions described by Heisenberg Hamiltonians are isotropic. Ising Hamiltonians are obtained from Heisenberg Hamiltonians by neglecting all spin exchange interactions but those that occur along one direction (i.e., the z-direction by convention). Thus spin exchange interactions become highly anisotropic under Ising Hamiltonians. In calculating isotropic spin exchange parameters using first-principles electronic structure calculations (see Section 4), the spin states of Heisenberg Hamiltonians are employed if the corresponding electronic structures are generated by the CI wave function method. However, the spin states of Ising Hamiltonians are employed if highest-spin (HS) and broken-symmetry (BS) states generated by electronic structure calculations are used for analysis [10,11,21,23,35]. The latter is the case even when a magnetic system under consideration exhibits no magnetic anisotropy. Thus we will also discuss the spin states of Ising Hamiltonians for spin dimers and extended spin lattices.

2.1. Spin dimers

For a spin dimer consisting of M unpaired spins at spin site 1 and N unpaired spins at the spin site 2, it can be assumed that $M \geqslant N$ (Fig. 1). The number of the possible spin states is 2^M at site 1, and 2^N at site 2, so that the number of the possible spin states for the spin dimer is 2^{M+N}. Our discussion will be limited to the spin exchange interactions that result when each spin site has the highest-spin multiplicity. Thus the number of spin states to consider is reduced to $(M+1)$ at site 1 and $(N+1)$ at site 2, so there are $(M+1)(N+1)$ spin states to consider for the spin dimer. The spin states of a spin dimer can be described by the Heisenberg Hamiltonian $\hat{H} = -J\hat{\mathbf{S}}_1 \cdot \hat{\mathbf{S}}_2$, which can be written in three different forms.

$$\hat{H} = -J(\hat{S}_{1x}\hat{S}_{2x} + \hat{S}_{1y}\hat{S}_{2y} + \hat{S}_{1z}\hat{S}_{2z}), \qquad (2.1a)$$

$$\hat{H} = -\frac{1}{2}J(\hat{S}^2 - \hat{S}_1^2 - \hat{S}_2^2), \qquad (2.1b)$$

$$\hat{H} = -J[\hat{S}_{1z}\hat{S}_{2z} + \frac{1}{2}(\hat{S}_1^+\hat{S}_2^- + \hat{S}_1^-\hat{S}_2^+)], \qquad (2.1c)$$

where $\hat{\mathbf{S}} = \hat{\mathbf{S}}_1 + \hat{\mathbf{S}}_2$, and $\hat{S}_m^+$ and $\hat{S}_m^-$ are the ladder operators, i.e., $\hat{S}_m^+ = \hat{S}_{mx} + i\hat{S}_{my}$ and $\hat{S}_m^- = \hat{S}_{mx} - i\hat{S}_{my}$ ($m = 1, 2$). The Ising Hamiltonian $\hat{H}^{\text{Ising}} = -J\hat{S}_{1z}\hat{S}_{2z}$
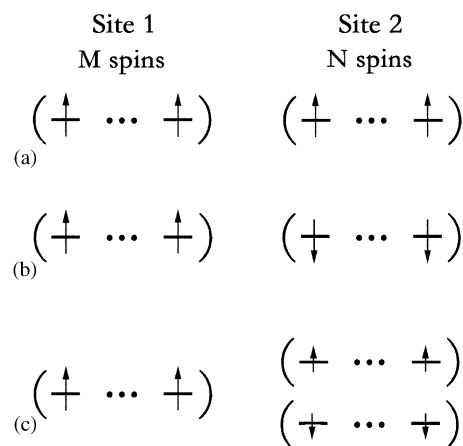

Fig. 1. Two spin states of a spin dimer that has M unpaired spins at the spin site 1 and N unpaired spins at the spin site 2: (a) the highest-spin state $|\text{HS}\rangle$ and (b) the broken-symmetry state $|\text{BS}\rangle$. Each spin site has the highest-spin arrangement, and the two spin sites interact ferromagnetically in $|\text{HS}\rangle$, and antiferromagnetically in $|\text{BS}\rangle$. In the transition state $|\text{TS}\rangle$ shown in (c), each of the $2N$ magnetic orbitals (α- and β-spin) of the spin site 2 has half an electron while the M unpaired electrons of the spin site 1 are accommodated in the α-spin magnetic orbitals.

results from Eq. (2.1a) by keeping only the interaction along the z-direction.

2.1.1. Heisenberg Hamiltonian

The spin states of a spin dimer are described by the spin wave functions $|S \ Ms\rangle$ using the quantum numbers S and Ms. The allowed values of S for the spin dimer are $S_{\max}, S_{\max} - 1, S_{\max} - 2, \ldots, S_{\min} + 1$, and $S_{\min}$, where $S_{\max} = (M+N)/2$ and $S_{\min} = (M-N)/2$. For a given S, the allowed values of Ms are $S, S-1, S-2, \ldots, -S+1$, and $-S$. Similarly, the spin wave functions for each spin site may be written as $|S_i \ Ms_i\rangle$ ($i = 1, 2$). Since each spin site has the highest-spin configuration, $S_1 = M/2$ and $S_2 = N/2$. Each wave function $|S \ Ms\rangle$ of the spin dimer can be expanded as a linear combination of product functions $|S_1 \ Ms_1\rangle|S_2 \ Ms_2\rangle$, namely [23,35],

$$|S \ Ms\rangle = \sum_{Ms_1}\sum_{Ms_2}\langle S_1 \ Ms_1 \ S_2 \ Ms_2|S \ Ms\rangle$$
$$\times |S_1 \ Ms_1\rangle|S_2 \ Ms_2\rangle, \qquad (2.2a)$$

where Ms_1 and Ms_2 run over the values satisfying the condition $Ms_1 + Ms_2 = Ms$, and the Clebsch–Gordon coefficients $\langle S_1 \ Ms_1 \ S_2 \ Ms_2|S \ Ms\rangle$ are expressed in terms of the $3 - j$ symbols as [36,37]

$$\langle S_1 \ Ms_1 \ S_2 \ Ms_2|S \ Ms\rangle$$
$$= (-1)^{-S_1+S_2-Ms}\sqrt{2S+1}\begin{pmatrix} S_1 & S_2 & S \\ Ms_1 & Ms_2 & -Ms \end{pmatrix}. \qquad (2.2b)$$

The expressions of the spin wave functions $|S \ Ms\rangle$ for $M = N = 1-3$ are listed in Table 1, and those for

Table 1
Spin wave functions $|S \quad Ms\rangle$ ($S = S_{max}, S_{max} - 1, \ldots, 0$) of spin dimers for which $M = N$ as a linear combination of the products of the spin functions of the spin sites 1 and 2

(a) $M = N = 1$

$|S \quad Ms\rangle$

$$|1 \quad \pm 1\rangle = \left|\frac{1}{2} \quad \pm\frac{1}{2}\right\rangle_1 \left|\frac{1}{2} \quad \pm\frac{1}{2}\right\rangle_2$$

$$|1 \quad 0\rangle = \sqrt{\frac{1}{2}}\left|\frac{1}{2} \quad \frac{1}{2}\right\rangle_1 \left|\frac{1}{2} \quad -\frac{1}{2}\right\rangle_2 + \sqrt{\frac{1}{2}}\left|\frac{1}{2} \quad -\frac{1}{2}\right\rangle_1 \left|\frac{1}{2} \quad \frac{1}{2}\right\rangle_2$$

$$|0 \quad 0\rangle = \sqrt{\frac{1}{2}}\left|\frac{1}{2} \quad \frac{1}{2}\right\rangle_1 \left|\frac{1}{2} \quad -\frac{1}{2}\right\rangle_2 - \sqrt{\frac{1}{2}}\left|\frac{1}{2} \quad -\frac{1}{2}\right\rangle_1 \left|\frac{1}{2} \quad \frac{1}{2}\right\rangle_2$$

(b) $M = N = 2$

$|S \quad Ms\rangle$

$$|2 \quad \pm 2\rangle = |1 \quad \pm 1\rangle_1 |1 \quad \pm 1\rangle_2$$

$$|2 \quad \pm 1\rangle = \sqrt{\frac{1}{2}}|1 \quad \pm 1\rangle_1 |1 \quad 0\rangle_2 + \sqrt{\frac{1}{2}}|1 \quad 0\rangle_1 |1 \quad \pm 1\rangle_2$$

$$|2 \quad 0\rangle = \sqrt{\frac{1}{6}}|1 \quad 1\rangle_1 |1 \quad -1\rangle_2 + \sqrt{\frac{1}{6}}|1 \quad -1\rangle_1 |1 \quad 1\rangle_2 + \sqrt{\frac{2}{3}}|1 \quad 0\rangle_1 |1 \quad 0\rangle_2$$

$$|1 \quad \pm 1\rangle = \pm\sqrt{\frac{1}{2}}|1 \quad \pm 1\rangle_1 |1 \quad 0\rangle_2 \mp \sqrt{\frac{1}{2}}|1 \quad 0\rangle_1 |1 \quad \pm 1\rangle_2$$

$$|1 \quad 0\rangle = \sqrt{\frac{1}{2}}|1 \quad 1\rangle_1 |1 \quad -1\rangle_2 - \sqrt{\frac{1}{2}}|1 \quad -1\rangle_1 |1 \quad 1\rangle_2$$

$$|0 \quad 0\rangle = \sqrt{\frac{1}{3}}|1 \quad 1\rangle_1 |1 \quad -1\rangle_2 + \sqrt{\frac{1}{3}}|1 \quad -1\rangle_1 |1 \quad 1\rangle_2 - \sqrt{\frac{1}{3}}|1 \quad 0\rangle_1 |1 \quad 0\rangle_2$$

(c) $M = N = 3$

$|S \quad Ms\rangle$

$$|3 \quad \pm 3\rangle = \left|\frac{3}{2} \quad \pm\frac{3}{2}\right\rangle_1 \left|\frac{3}{2} \quad \pm\frac{3}{2}\right\rangle_2$$

$$|3 \quad \pm 2\rangle = \sqrt{\frac{1}{2}}\left|\frac{3}{2} \quad \pm\frac{3}{2}\right\rangle_1 \left|\frac{3}{2} \quad \pm\frac{1}{2}\right\rangle_2 + \sqrt{\frac{1}{2}}\left|\frac{3}{2} \quad \pm\frac{1}{2}\right\rangle_1 \left|\frac{3}{2} \quad \pm\frac{3}{2}\right\rangle_2$$

$$|3 \quad \pm 1\rangle = \sqrt{\frac{1}{5}}\left|\frac{3}{2} \quad \pm\frac{3}{2}\right\rangle_1 \left|\frac{3}{2} \quad \mp\frac{1}{2}\right\rangle_2 + \sqrt{\frac{1}{5}}\left|\frac{3}{2} \quad \mp\frac{1}{2}\right\rangle_1 \left|\frac{3}{2} \quad \pm\frac{3}{2}\right\rangle_2 + \sqrt{\frac{3}{5}}\left|\frac{3}{2} \quad \pm\frac{1}{2}\right\rangle_1 \left|\frac{3}{2} \quad \pm\frac{1}{2}\right\rangle_2$$

$$|3 \quad 0\rangle = \frac{1}{2}\sqrt{\frac{1}{5}}\left|\frac{3}{2} \quad \frac{3}{2}\right\rangle_1 \left|\frac{3}{2} \quad -\frac{3}{2}\right\rangle_2 + \frac{1}{2}\sqrt{\frac{1}{5}}\left|\frac{3}{2} \quad -\frac{3}{2}\right\rangle_1 \left|\frac{3}{2} \quad \frac{3}{2}\right\rangle_2 + \frac{1}{2}\sqrt{\frac{1}{5}}\left|\frac{3}{2} \quad -\frac{3}{2}\right\rangle_1 \left|\frac{3}{2} \quad \frac{3}{2}\right\rangle_2 + \frac{1}{2}\sqrt{\frac{1}{5}}\left|\frac{3}{2} \quad -\frac{3}{2}\right\rangle_1 \left|\frac{3}{2} \quad \frac{3}{2}\right\rangle_2 + \frac{3}{2}\sqrt{\frac{1}{5}}\left|\frac{3}{2} \quad -\frac{1}{2}\right\rangle_1 \left|\frac{3}{2} \quad \frac{1}{2}\right\rangle_2$$

$$|2 \quad \pm 2\rangle = \pm\sqrt{\frac{1}{2}}\left|\frac{3}{2} \quad \pm\frac{3}{2}\right\rangle_1 \left|\frac{3}{2} \quad \pm\frac{1}{2}\right\rangle_2 \mp \sqrt{\frac{1}{2}}\left|\frac{3}{2} \quad \pm\frac{1}{2}\right\rangle_1 \left|\frac{3}{2} \quad \pm\frac{3}{2}\right\rangle_2$$

$$|2 \quad \pm 1\rangle = \pm\sqrt{\frac{1}{2}}\left|\frac{3}{2} \quad \pm\frac{3}{2}\right\rangle_1 \left|\frac{3}{2} \quad \mp\frac{1}{2}\right\rangle_2 \mp \sqrt{\frac{1}{2}}\left|\frac{3}{2} \quad \mp\frac{1}{2}\right\rangle_1 \left|\frac{3}{2} \quad \pm\frac{3}{2}\right\rangle_2$$

$$|2 \quad 0\rangle = \frac{1}{2}\left|\frac{3}{2} \quad \frac{3}{2}\right\rangle_1 \left|\frac{3}{2} \quad -\frac{3}{2}\right\rangle_2 - \frac{1}{2}\left|\frac{3}{2} \quad -\frac{3}{2}\right\rangle_1 \left|\frac{3}{2} \quad \frac{3}{2}\right\rangle_2 + \frac{1}{2}\left|\frac{3}{2} \quad \frac{1}{2}\right\rangle_1 \left|\frac{3}{2} \quad -\frac{1}{2}\right\rangle_2 - \frac{1}{2}\left|\frac{3}{2} \quad -\frac{1}{2}\right\rangle_1 \left|\frac{3}{2} \quad \frac{1}{2}\right\rangle_2$$

$$|1 \quad \pm 1\rangle = \sqrt{\frac{3}{10}}\left|\frac{3}{2} \quad \pm\frac{3}{2}\right\rangle_1 \left|\frac{3}{2} \quad \mp\frac{1}{2}\right\rangle_2 + \sqrt{\frac{3}{10}}\left|\frac{3}{2} \quad \mp\frac{1}{2}\right\rangle_1 \left|\frac{3}{2} \quad \pm\frac{3}{2}\right\rangle_2 - \sqrt{\frac{2}{5}}\left|\frac{3}{2} \quad \pm\frac{1}{2}\right\rangle_1 \left|\frac{3}{2} \quad \pm\frac{1}{2}\right\rangle_2$$

$$|1 \quad 0\rangle = \frac{3}{2}\sqrt{\frac{1}{5}}\left|\frac{3}{2} \quad \frac{3}{2}\right\rangle_1 \left|\frac{3}{2} \quad -\frac{3}{2}\right\rangle_2 + \frac{3}{2}\sqrt{\frac{1}{5}}\left|\frac{3}{2} \quad -\frac{3}{2}\right\rangle_1 \left|\frac{3}{2} \quad \frac{3}{2}\right\rangle_2 - \frac{1}{2}\sqrt{\frac{1}{5}}\left|\frac{3}{2} \quad \frac{1}{2}\right\rangle_1 \left|\frac{3}{2} \quad -\frac{1}{2}\right\rangle_2 - \frac{1}{2}\sqrt{\frac{1}{5}}\left|\frac{3}{2} \quad -\frac{1}{2}\right\rangle_1 \left|\frac{3}{2} \quad \frac{1}{2}\right\rangle_2$$

$$|0 \quad 0\rangle = \frac{1}{2}\left|\frac{3}{2} \quad \frac{3}{2}\right\rangle_1 \left|\frac{3}{2} \quad -\frac{3}{2}\right\rangle_2 - \frac{1}{2}\left|\frac{3}{2} \quad -\frac{3}{2}\right\rangle_1 \left|\frac{3}{2} \quad \frac{3}{2}\right\rangle_2 - \frac{1}{2}\left|\frac{3}{2} \quad \frac{1}{2}\right\rangle_1 \left|\frac{3}{2} \quad -\frac{1}{2}\right\rangle_2 + \frac{1}{2}\left|\frac{3}{2} \quad -\frac{1}{2}\right\rangle_1 \left|\frac{3}{2} \quad \frac{1}{2}\right\rangle_2$$

$M = N = 4, 5$ can be found in Ref. [35]. For various cases, the HS state depicted in Fig. 1a is given by one $|S_1 \quad Ms_1\rangle|S_2 \quad Ms_2\rangle$ term,

$$|\text{HS}\rangle = \left|\frac{1}{2}M, \frac{1}{2}M\right\rangle_1 \left|\frac{1}{2}N, \frac{1}{2}N\right\rangle_2. \qquad (2.3)$$

All other spin states $|S \quad Ms\rangle$ are expressed as a linear combination of more than one $|S_1 \quad Ms_1\rangle|S_2 \quad Ms_2\rangle$ term [35].

The spin wave functions are eigenfunctions of the $\hat{S}^2$ operator such that $\hat{S}^2|S \quad Ms\rangle = S(S+1)|S \quad Ms\rangle$, and $\hat{S}_i^2|S_i \quad Ms_i\rangle = S_i(S_i+1)|S_i \quad Ms_i\rangle$ ($i = 1, 2$). Thus from Eqs. (2.1a) and (2.2a), we obtain

$$\hat{H}|S \quad Ms\rangle = -\frac{1}{2}J[S(S+1) - S_1(S_1+1) - S_2(S_2+1)]$$
$$\times |S \quad Ms\rangle \equiv E_s(S)|S \quad Ms\rangle \qquad (2.4)$$

That is, the spin wave functions $|S \quad Ms\rangle$ are the eigenfunctions of the Heisenberg Hamiltonian.

S=5 E=-25J/4

S=4 E=-4J

S=3 E=-9J/4

S=2 E=-J

S=4 E=-5J/4

S=1 E=-J/4

S=3 E=0

S=0 E=3J/4

S=1 E=J

S=2 E=3J/4

S=0 E=2J

S=1 E=11J/4

S=2 E=3J

S=3 E=11J/4

S=0 E=15J/4

S=1 E=5J

S=0 E=6J

S=2 E=23J/4

S=1 E=31J/4

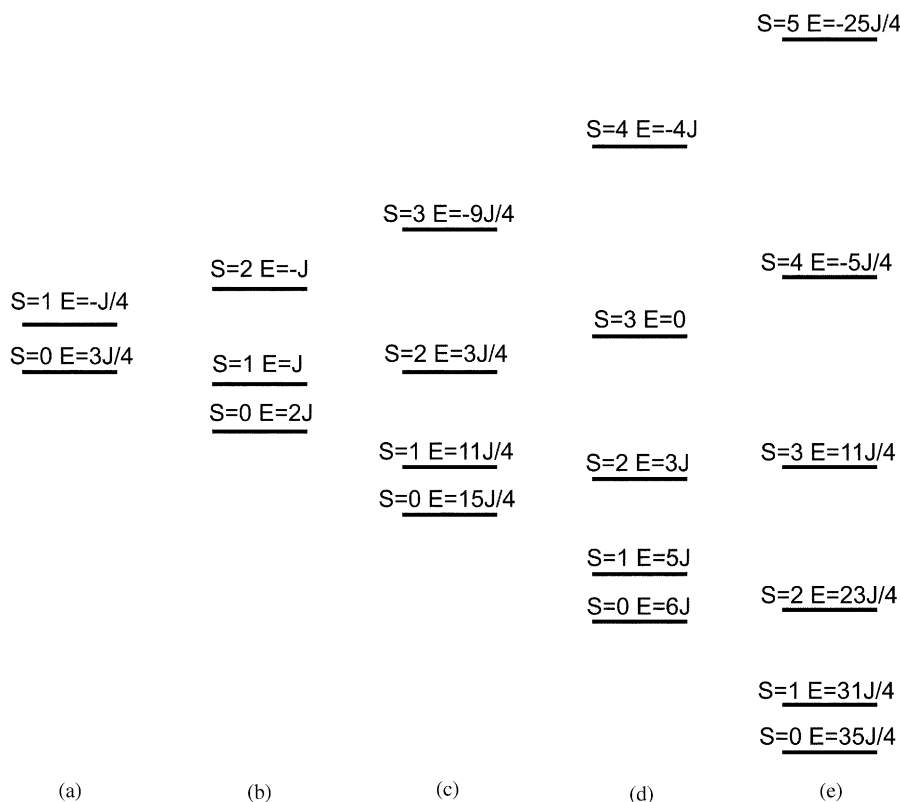S=0 E=35J/4

(a)   (b)   (c)   (d)   (e)

Fig. 2. Eigenvalues $E(S)$ of the Heisenberg spin Hamiltonian $\hat{H} = -J\hat{S}_1 \cdot \hat{S}_2$ for $M = N = 1-5$. In this plot the value of J was assumed to be negative.

The eigenvalue $E_s(S)$ depends only on S, because S_1 and S_2 are constants (i.e., $S_1 = \frac{1}{2}M$ and $S_2 = 1/2 N$). All the $E_s(S)$ values for the case of $M = N = 1-5$ are graphically presented in Fig. 2. For the HS spin state, $S = S_{max} = \frac{1}{2}(M + N) = S_1 + S_2$. For the lowest-spin state, $S = S_{min} = \frac{1}{2}(M - N) = S_1 - S_2$. Therefore the eigenvalues of these states are given by [35]

$$E_s(S_{max}) \equiv E_s(\text{HS}) = -\frac{1}{4} MNJ, \tag{2.5a}$$

$$E_s(S_{min}) = \frac{1}{4} MNJ + \frac{1}{2} NJ \tag{2.5b}$$

and the energy separation between adjacent eigenstates follows the Landé's interval rule [35,38].

$$E_s(S) - E_s(S - 1) = -\frac{1}{2} J[S(S + 1) - (S - 1)S] = -JS. \tag{2.5c}$$

Each energy level $E_s(S)$ consists of $2S + 1$ substates (i.e., $Ms = S, S-1, S-2, \ldots, -S + 2, -S + 1, -S$). The weighted sum of all the eigenvalues is found to be zero

[36], namely,

$$\sum_{S=|M-N|/2}^{(M+N)/2} (2S + 1)$$
$$\times \left(-\frac{1}{2} J\lfloor S(S + 1) - S_1(S_1 + 1) - S_2(S_2 + 1)\rfloor\right) = 0. \tag{2.6}$$

The energy gap ΔE_s between the ground and the first excited spin states plays an important role in determining the J value experimentally, and also in calculating the J value by first-principles electronic structure calculations using the CI wave function method. The ground spin state is the lowest spin state (i.e., S_{min}) for an antiferromagnetic system (i.e., $J < 0$), and the highest spin state (i.e., S_{max}) for the ferromagnetic system (i.e., $J > 0$). Thus from Eqs. (2.4) and (2.5), we obtain [35]

$$\Delta E_s = \begin{cases} -[1 + \frac{1}{2}(M - N)]J & (\text{for } J < 0), \\ [N + \frac{1}{2}(M - N)]J & (\text{for } J > 0). \end{cases} \tag{2.7}$$

When $M = N$, therefore, the first excitation energy ΔE_s is $-J$ for an antiferromagnetic system while it is NJ for a ferromagnetic system.

2.1.2. Broken symmetry spin states and Heisenberg spin Hamiltonian

For the spin dimer with M spins at spin site 1 and N spins at spin site 2, the wave function of its BS spin state depicted in Fig. 1b is given by [23,35]

$$|BS\rangle = \left|\frac{1}{2}M, \frac{1}{2}M\right\rangle_1 \left|\frac{1}{2}N, -\frac{1}{2}N\right\rangle_2. \qquad (2.8)$$

To understand how the BS spin state is related to the Heisenberg Hamiltonian $\hat{H} = -J\hat{S}_1 \cdot \hat{S}_2$, it is necessary to expand the BS spin state in terms of the eigenstates of $\hat{H}$. By using the orthonormal property of spin wave functions, one can derive the following expression from Eq. (2.2a):

$$|S_1 \quad Ms_1\rangle|S_2 \quad Ms_2\rangle = \sum_{S=|S_1-S_2|}^{S_1+S_2} (-1)^{-S_1+S_2-Ms}\sqrt{2S+1}$$

$$\times \begin{pmatrix} S_1 & S_2 & S \\ Ms_1 & Ms_2 & -Ms \end{pmatrix} |S \quad Ms\rangle, \qquad (2.9)$$

where $Ms = Ms_1 + Ms_2$. Thus, the wave function of the BS spin state is expressed as [35]

$$|BS\rangle = \sum_{S=|M-N|/2}^{(M+N)/2} C(S,M,N)\left|S \quad \frac{1}{2}(M-N)\right\rangle. \qquad (2.10a)$$

If $M = N$, this is simplified as

$$|BS\rangle = \sum_{S=0}^{N} C(S,N,N)|S \quad 0\rangle \sum_{S=0}^{N} \sqrt{2S+1}$$

$$\times \begin{pmatrix} \frac{1}{2}N & \frac{1}{2}N & S \\ \frac{1}{2}N & -\frac{1}{2}N & 0 \end{pmatrix} |S \quad 0\rangle. \qquad (2.10b)$$

The decompositions of the BS spin states in terms of the eigenstates of the Heisenberg Hamiltonian $\hat{H} = -J\hat{S}_1 \cdot \hat{S}_2$ are listed in Table 2 for cases of $M = N = 1-5$, and in Table 3 for cases of $M > N$ [35].

In general, the BS spin state is not an eigenstate of $\hat{S}^2$. It was found that the expectation value of $\hat{S}^2$ for the BS

spin state is given by [35]

$$\langle BS|\hat{S}^2|BS\rangle = \frac{1}{4}(M-N)^2 + \frac{1}{2}(M+N). \qquad (2.11)$$

Thus $\langle BS|\hat{S}^2|BS\rangle = N$ when $M = N$. This explains why in DFT calculations the BS electronic states have the expectation value $\langle \hat{S}^2 \rangle \approx 1$ for $M = N = 1$, and $\langle \hat{S}^2 \rangle \approx 2$ for $M = N = 2$ (for a recent review, see Ref. [22]). The operators $\hat{S}^2$ and $\hat{H} = -J\hat{S}_1 \cdot \hat{S}_2$ commute. Thus the BS spin state is not an eigenstate of $\hat{H}$ because it is not an eigenstate of $\hat{S}^2$. The expectation value of $\hat{H}$ for the BS spin state is given by [23,35]

$$\langle BS|\hat{H}|BS\rangle \equiv E_s(BS) = \frac{1}{4}MNJ. \qquad (2.12)$$

From Eqs. (2.5a) and (2.12), therefore, the spin exchange parameter J is related to the energy difference between the BS and HS spin states as [23,35]

$$E_s(BS) - E_s(HS) = \frac{1}{2}MNJ. \qquad (2.13)$$

For the eigenstates of the spin Hamiltonian $\hat{H} = -J\hat{S}_1 \cdot \hat{S}_2$, Eq. (2.7) shows that the weighted sum of the eigenvalues of all $(M+1)(N+1)$ spin states is zero. An analogous relationship exists for the HS and BS spin states. Namely, as shown in Eqs. (2.5a) and (2.12), the energies of the BS and HS states are the same in magnitude, but opposite in sign so that the sum of their energies is zero [35].

2.1.3. Broken symmetry spin states and the Ising spin Hamiltonian

The Heisenberg Hamiltonian $\hat{H}$ does not commute with the Ising Hamiltonian $\hat{H}^{Ising}$, so the eigenstates of $\hat{H}$ are not necessarily the eigenstates of $\hat{H}^{Ising}$, and vice versa. Each spin state $|S_1 \quad Ms_1\rangle|S_2 \quad Ms_2\rangle$ is an eigenstate of $\hat{H}^{Ising}$ with eigenvalue $-Ms_1 Ms_2 J$, namely [35],

$$\hat{H}^{Ising}|S_1 \quad Ms_1\rangle|S_2 \quad Ms_2\rangle$$
$$= -Ms_1 Ms_2 J|S_1 \quad Ms_1\rangle|S_2 \quad Ms_2\rangle. \qquad (2.14)$$

Table 2
Coefficients for the expansion of a BS spin state in terms of the eigenstates $|S \quad 0\rangle$ ($S = S_{max}, S_{max} - 1, \ldots, 0$) of the spin Hamiltonian $\hat{H} = -J\hat{S}_1 \cdot \hat{S}_2$ for the case of $M = N$

	BS state	$\|0 \quad 0\rangle$	$\|1 \quad 0\rangle$	$\|2 \quad 0\rangle$	$\|3 \quad 0\rangle$	$\|4 \quad 0\rangle$	$\|5 \quad 0\rangle$
$N=1$	$\left\|\frac{1}{2} \quad \frac{1}{2}\right\rangle_1\left\|\frac{1}{2} \quad -\frac{1}{2}\right\rangle_2$	$\sqrt{\frac{1}{2}}$	$\sqrt{\frac{1}{2}}$				
$N=2$	$\|1 \quad 1\rangle_1\|1 \quad -1\rangle_2$	$\sqrt{\frac{1}{3}}$	$\sqrt{\frac{1}{2}}$	$\sqrt{\frac{1}{6}}$			
$N=3$	$\left\|\frac{3}{2} \quad \frac{3}{2}\right\rangle_1\left\|\frac{3}{2} \quad -\frac{3}{2}\right\rangle_2$	$\frac{1}{2}$	$\frac{3}{2}\sqrt{\frac{1}{5}}$	$\frac{1}{2}$	$\frac{1}{2}\sqrt{\frac{1}{5}}$		
$N=4$	$\|2 \quad 2\rangle_1\|2 \quad -2\rangle_2$	$\sqrt{\frac{1}{5}}$	$\sqrt{\frac{2}{5}}$	$\sqrt{\frac{2}{7}}$	$\sqrt{\frac{1}{10}}$	$\sqrt{\frac{1}{70}}$	
$N=5$	$\left\|\frac{5}{2} \quad \frac{5}{2}\right\rangle_1\left\|\frac{5}{2} \quad -\frac{5}{2}\right\rangle_2$	$\sqrt{\frac{1}{6}}$	$\sqrt{\frac{5}{14}}$	$\frac{5}{2}\sqrt{\frac{1}{21}}$	$\frac{1}{6}\sqrt{5}$	$\frac{1}{2}\sqrt{\frac{1}{7}}$	$\frac{1}{6}\sqrt{\frac{1}{7}}$

Table 3
Decomposition of a BS spin state in terms of the eigenstates $|S(M - N)/2\rangle$ ($S = S_{max}, S_{max} - 1, \ldots, S_{min}$) of the spin Hamiltonian $\hat{H} = -J\hat{S}_1 \cdot \hat{S}_2$ for the case of $M \neq N$

Cases	BS state
$M = 2, N = 1$	$\lvert 1 \ \ 1 \rangle_1 \left\lvert \frac{1}{2} \ \ -\frac{1}{2} \right\rangle_2 = \sqrt{\frac{2}{3}} \left\lvert \frac{1}{2} \ \ \frac{1}{2} \right\rangle + \sqrt{\frac{1}{3}} \left\lvert \frac{3}{2} \ \ \frac{1}{2} \right\rangle$
$M = 3, N = 1$	$\left\lvert \frac{3}{2} \ \ \frac{3}{2} \right\rangle_1 \left\lvert \frac{1}{2} \ \ -\frac{1}{2} \right\rangle_2 = \sqrt{\frac{3}{4}} \lvert 1 \ \ 1 \rangle + \sqrt{\frac{1}{4}} \lvert 2 \ \ 1 \rangle$
$M = 4, N = 1$	$\lvert 2 \ \ 2 \rangle_1 \left\lvert \frac{1}{2} \ \ -\frac{1}{2} \right\rangle_2 = \sqrt{\frac{4}{5}} \left\lvert \frac{3}{2} \ \ \frac{3}{2} \right\rangle + \sqrt{\frac{1}{5}} \left\lvert \frac{5}{2} \ \ \frac{3}{2} \right\rangle$
$M = 5, N = 1$	$\left\lvert \frac{5}{2} \ \ \frac{5}{2} \right\rangle_1 \left\lvert \frac{1}{2} \ \ -\frac{1}{2} \right\rangle_2 = \sqrt{\frac{5}{6}} \lvert 2 \ \ 2 \rangle + \sqrt{\frac{1}{6}} \lvert 3 \ \ 2 \rangle$
$M = 3, N = 2$	$\left\lvert \frac{3}{2} \ \ \frac{3}{2} \right\rangle_1 \lvert 1 \ \ -1 \rangle_2 = \sqrt{\frac{1}{2}} \left\lvert \frac{1}{2} \ \ \frac{1}{2} \right\rangle + \sqrt{\frac{2}{5}} \left\lvert \frac{3}{2} \ \ \frac{1}{2} \right\rangle + \sqrt{\frac{1}{10}} \left\lvert \frac{5}{2} \ \ \frac{1}{2} \right\rangle$
$M = 4, N = 2$	$\lvert 2 \ \ 2 \rangle_1 \lvert 1 \ \ -1 \rangle_2 = \sqrt{\frac{3}{5}} \lvert 1 \ \ 1 \rangle + \sqrt{\frac{1}{3}} \lvert 2 \ \ 1 \rangle + \sqrt{\frac{1}{15}} \lvert 3 \ \ 1 \rangle$
$M = 5, N = 2$	$\left\lvert \frac{5}{2} \ \ \frac{5}{2} \right\rangle_1 \lvert 1 \ \ -1 \rangle_2 = \sqrt{\frac{2}{3}} \left\lvert \frac{3}{2} \ \ \frac{3}{2} \right\rangle + \sqrt{\frac{2}{7}} \left\lvert \frac{5}{2} \ \ \frac{3}{2} \right\rangle + \sqrt{\frac{1}{21}} \left\lvert \frac{7}{2} \ \ \frac{3}{2} \right\rangle$
$M = 4, N = 3$	$\lvert 2 \ \ 2 \rangle_1 \left\lvert \frac{3}{2} \ \ -\frac{3}{2} \right\rangle_2 = \sqrt{\frac{2}{5}} \left\lvert \frac{1}{2} \ \ \frac{1}{2} \right\rangle + \sqrt{\frac{2}{5}} \left\lvert \frac{3}{2} \ \ \frac{1}{2} \right\rangle + \sqrt{\frac{6}{35}} \left\lvert \frac{5}{2} \ \ \frac{1}{2} \right\rangle + \sqrt{\frac{1}{35}} \left\lvert \frac{7}{2} \ \ \frac{1}{2} \right\rangle$
$M = 5, N = 3$	$\left\lvert \frac{5}{2} \ \ \frac{5}{2} \right\rangle_1 \left\lvert \frac{3}{2} \ \ -\frac{3}{2} \right\rangle_2 = \sqrt{\frac{1}{2}} \lvert 1 \ \ 1 \rangle + \sqrt{\frac{5}{14}} \lvert 2 \ \ 1 \rangle + \sqrt{\frac{1}{8}} \lvert 3 \ \ 1 \rangle + \sqrt{\frac{1}{56}} \lvert 4 \ \ 1 \rangle$
$M = 5, N = 4$	$\left\lvert \frac{5}{2} \ \ \frac{5}{2} \right\rangle_1 \lvert 2 \ \ -2 \rangle_2 = \sqrt{\frac{1}{3}} \left\lvert \frac{1}{2} \ \ \frac{1}{2} \right\rangle + \sqrt{\frac{8}{21}} \left\lvert \frac{3}{2} \ \ \frac{1}{2} \right\rangle + \sqrt{\frac{3}{14}} \left\lvert \frac{5}{2} \ \ \frac{1}{2} \right\rangle + \sqrt{\frac{4}{63}} \left\lvert \frac{7}{2} \ \ \frac{1}{2} \right\rangle + \sqrt{\frac{1}{126}} \left\lvert \frac{9}{2} \ \ \frac{1}{2} \right\rangle$

Thus the HS and BS spin states are eigenstates of $\hat{H}^{Ising}$. The HS spin state is an eigenstate of both $\hat{H}$ and $\hat{H}^{Ising}$ with the same eigenvalue. The eigenvalue of $\hat{H}^{Ising}$ for the BS spin state is the same as the expectation value of $\hat{H}$ for the BS spin state [35].

For a given eigenstate $|S \ \ Ms\rangle$ of the Heisenberg Hamiltonian $\hat{H}$, the expectation value of the Ising Hamiltonian, i.e., $\langle S \ \ Ms|\hat{H}^{Ising}|S \ \ Ms\rangle$, is written as

$$\langle S \ \ Ms|\hat{H}^{Ising}|S \ \ Ms\rangle$$
$$= -\sum_{Ms1}\sum_{Ms2}\langle S_1 \ \ Ms_1 \ \ S_2 \ \ Ms_2|S \ \ Ms\rangle^2 Ms_1 Ms_2 J$$
(2.15)

by combining Eqs. (2.2a) and (2.14). For $M = N = 1-2$, the $\langle S \ \ Ms|\hat{H}^{Ising}|S \ \ Ms\rangle$ value for a certain eigenstate $|S \ \ Ms\rangle$ is the same as the energy of the BS spin state given by Eq. (2.12). However, this is not true any more for $M = N \geqslant 3$. Therefore, the meaning of a BS spin state cannot be related to an expectation value $\langle S \ \ Ms|\hat{H}^{Ising}|S \ \ Ms\rangle$, but should be discussed as an eigenstate of an Ising Hamiltonian [35].

2.2. Extended spin lattices

2.2.1. Ising Hamiltonian and ordered spin states

The Ising Hamiltonian for an extended spin lattice is written as

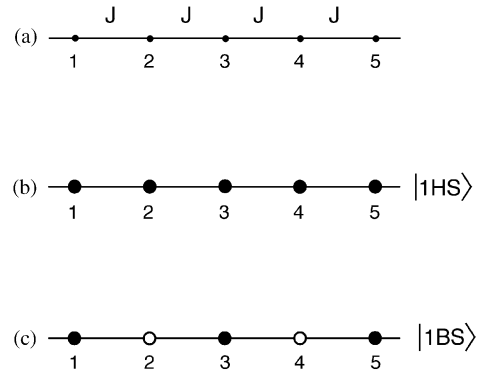$$\hat{H}^{Ising} = -\sum_{i<j} J_{ij}\hat{S}_{iz}\hat{S}_{jz}.$$
(2.16)

Fig. 3. (a) 1D uniform chain with one spin exchange parameter J. (b) Spin arrangement of $|1HS\rangle$. (c) Spin arrangement of $|1BS\rangle$.

It is relatively straightforward to determine the energies of various ordered spin states of a magnetic solid in terms of this Hamiltonian [21]. For example, consider a one-dimensional (1D) uniform magnetic chain described by one spin exchange parameter J (Fig. 3a), which has n spin sites ($n \rightarrow \infty$). For this chain the Ising Hamiltonian becomes

$$\hat{H}_1^{Ising} = -J\sum_{i=1}^{n-1}\hat{S}_{iz}\hat{S}_{(i+1)z}.$$
(2.17)

The HS and BS states shown in Fig. 3a and b are two ordered spin states of this uniform chain.

$$|1HS\rangle = |\uparrow\rangle_1|\uparrow\rangle_2|\uparrow\rangle_3|\uparrow\rangle_4\cdots|\uparrow\rangle_{n-1}|\uparrow\rangle_n,$$
(2.18a)

$$|1BS\rangle = |\uparrow\rangle_1|\downarrow\rangle_2|\uparrow\rangle_3|\downarrow\rangle_4\cdots|\uparrow\rangle_{n-1}|\downarrow\rangle_n.$$
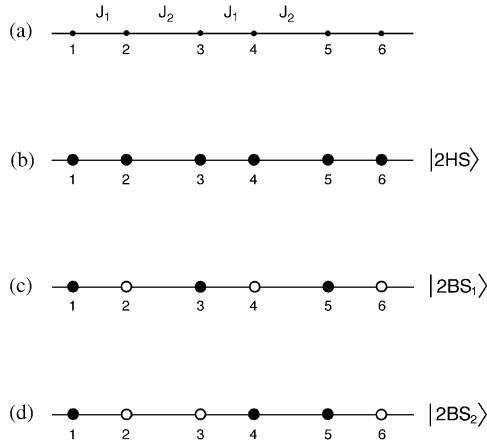(2.18b)

Fig. 4. (a) 1D alternating chain with two spin exchange parameters J_1 and J_2. (b) Spin arrangement of $|2\mathrm{HS}\rangle$. (c) Spin arrangement of $|2\mathrm{BS}_1\rangle$. (d) Spin arrangement of $|2\mathrm{BS}_2\rangle$.

Then the energies of these states per spin site are calculated to be

$$E_s(1\mathrm{HS}) \equiv \frac{1}{n}\langle 1\mathrm{HS}|\hat{H}_1^{\mathrm{Ising}}|1\mathrm{HS}\rangle = -\frac{1}{4}J, \qquad (2.19\mathrm{a})$$

$$E_s(1\mathrm{BS}) \equiv \frac{1}{n}\langle 1\mathrm{BS}|\hat{H}_1^{\mathrm{Ising}}|1\mathrm{BS}\rangle = \frac{1}{4}J. \qquad (2.19\mathrm{b})$$

As another example, consider a 1D alternating magnetic chain described by two spin exchange parameters J_1 and J_2 (Fig. 4a), which has n spin sites ($n \to \infty$). For this 1D magnetic chain the Ising Hamiltonian is written as

$$\hat{H}_2^{\mathrm{Ising}} = -\sum_{i=1}^{n/2}(J_1\hat{S}_{(2i)z}\hat{S}_{(2i-1)z} + J_2\hat{S}_{(2i)z}\hat{S}_{(2i+1)z}). \qquad (2.20)$$

The HS and the BS states shown in Fig. 4b–d are three ordered spin states of this chain.

$$|2\mathrm{HS}\rangle = |\uparrow\rangle_1|\uparrow\rangle_2|\uparrow\rangle_3|\uparrow\rangle_4 \cdots |\uparrow\rangle_{n-1}|\uparrow\rangle_n, \qquad (2.21\mathrm{a})$$

$$|2\mathrm{BS}_1\rangle = |\uparrow\rangle_1|\downarrow\rangle_2|\uparrow\rangle_3|\downarrow\rangle_4 \cdots |\uparrow\rangle_{n-1}|\downarrow\rangle_n, \qquad (2.21\mathrm{b})$$

$$|2\mathrm{BS}_2\rangle = |\uparrow\rangle_1|\downarrow\rangle_2|\downarrow\rangle_3|\uparrow\rangle_4|\uparrow\rangle_5|\downarrow\rangle_6 \cdots |\uparrow\rangle_{n-1}|\downarrow\rangle_n. \qquad (2.21\mathrm{c})$$

Then the energies of these states per spin site are calculated to be

$$E_s(2\mathrm{HS}) \equiv \frac{1}{n}\langle 2\mathrm{HS}|\hat{H}_2^{\mathrm{Ising}}|2\mathrm{HS}\rangle = -\frac{1}{8}(J_1 + J_2), \qquad (2.22\mathrm{a})$$

$$E_s(2\mathrm{BS}_1) \equiv \frac{1}{n}\langle 2\mathrm{BS}_1|\hat{H}_2^{\mathrm{Ising}}|2\mathrm{BS}_1\rangle = \frac{1}{8}(J_1 + J_2), \qquad (2.22\mathrm{b})$$

$$E_s(2\mathrm{BS}_2) \equiv \frac{1}{n}\langle 2\mathrm{BS}_2|\hat{H}_2^{\mathrm{Ising}}|2\mathrm{BS}_2\rangle = \frac{1}{8}(J_1 - J_2). \qquad (2.22\mathrm{c})$$

2.2.2. Heisenberg spin Hamiltonian

By analogy with Eq. (2.1c) the Heisenberg spin Hamiltonian $\hat{H}$ for an extended magnetic solid can be rewritten as

$$\begin{aligned}\hat{H} &= -\sum_{i<j} J_{ij}\hat{S}_i \cdot \hat{S}_j \\ &= -\sum_{i<j} J_{ij}[\hat{S}_{iz}\hat{S}_{jz} + \frac{1}{2}(\hat{S}_i^+\hat{S}_j^- + \hat{S}_i^-\hat{S}_j^+)].\end{aligned} \qquad (2.23)$$

It is a non-trivial task to determine the eigenvalue spectrum of this Hamiltonian [39,40]. As an example, consider a magnetic solid that has n spin sites per repeat unit cell and one unpaired spin per spin site. Then the eigenstates of this Hamiltonian can be generated as linear combinations of all possible product spin functions (e.g., $|\uparrow\rangle_1|\downarrow\rangle_2|\uparrow\rangle_3 \cdots |\uparrow\rangle_n$, $|\uparrow\rangle_1|\downarrow\rangle_2|\downarrow\rangle_3 \cdots |\uparrow\rangle_n$, etc.), which are obtained by using either the $|\uparrow\rangle$ or $|\downarrow\rangle$ spin state at each spin site $i(=1, 2, \ldots, n)$. Then, the number of basis functions needed to represent a unit cell of n spin sites is 2^n so that the matrix representation of $\hat{H}$ using these basis functions has the dimension $2^n \times 2^n$. The latter increases exponentially with increasing n so that the resulting matrix quickly becomes too large to diagonalize. Furthermore, the diagonalization can only be carried out numerically as a function of the ratios of spin exchange parameters (i.e., the relative strengths of spin exchange interactions). Therefore, to gain insight into how the eigenvalue spectrum depends on the spin exchange paths, it is necessary to repeat calculations for a large number of different ratios. As a consequence, the eigenvalue structures of Heisenberg Hamiltonians can be determined only for simple extended spin lattices.

3. Interactions beyond bilinear isotropic spin exchange

In the present section we discuss antisymmetric (or asymmetric), anisotropic and biquadratic interactions between spins and examine how these interactions modify the eigenvalue structures of Heisenberg Hamiltonians. For simplicity, our discussion will be confined to spin dimers with $M = N = 1-5$.

Moriya [4] showed that the most general bilinear expression of a spin Hamiltonian $\hat{H}$ for the exchange interaction between two spin sites in orbital singlet states with total spin operators $\hat{S}_1$ and $\hat{S}_2$ is

$$\hat{H} = -J \quad \hat{S}_1 \cdot \hat{S}_2 + \vec{D} \cdot (\hat{S}_1 \times \hat{S}_2) + \hat{S}_1 \cdot \Gamma \cdot \hat{S}_2, \qquad (3.1)$$

where the first term describes isotropic interaction ($\hat{H}_{\mathrm{iso}}$), the second term the antisymmetric interaction ($\hat{H}_{\mathrm{anti}}$), and the third term the anisotropic interaction ($\hat{H}_{\mathrm{aniso}}$).

$$\hat{H}_{\mathrm{iso}} = -J \quad \hat{S}_1 \cdot \hat{S}_2, \qquad (3.2\mathrm{a})$$

$$\hat{H}_{\mathrm{anti}} = \vec{D} \cdot (\hat{S}_1 \times \hat{S}_2), \qquad (3.2\mathrm{b})$$

$$\hat{H}_{\mathrm{aniso}} = \hat{S}_1 \cdot \Gamma \cdot \hat{S}_2. \qquad (3.2\mathrm{c})$$

This expression was obtained by considering the spin–orbit interaction as a perturbation and calculating the second order perturbation energy to terms bilinear in isotropic spin exchange interaction and spin–orbit coupling. In cases of orbital singlet ground states, and spin–orbit coupling small compared with the crystal field splitting of the orbital states, it has been customary to estimate the magnitudes of the D_i and Γ_{ij} elements by [4,30]

$$D_i \approx (\Delta g/g)J, \quad \Gamma_{ij} \approx (\Delta g/g)^2 J \tag{3.3}$$

with $\Delta g = |g - 2|$. Δg is the contribution of the orbital moment to the g factor and is of the order of $\lambda/\Delta E$, where λ is the spin–orbit coupling constant and ΔE is the crystal field splitting. Under the conditions where Eq. (3.3) is valid, $\Delta g/g \approx 0.1$ at most so that the isotropic term dominates in Eq. (3.1). However, it has been pointed out [33] that the estimation by Eq. (3.3) can be completely wrong.

The general expression of a spin Hamiltonian, Eq. (3.1), is also derived without resorting to perturbation theory. By considering the spin exchange parameter $\boldsymbol{J}$ and the spin operators $\hat{\boldsymbol{S}}_1$ and $\hat{\boldsymbol{S}}_2$ as tensors, Erdös [5] wrote a spin Hamiltonian as

$$\hat{H} = \sum_{\mu} \sum_{v} J_{\mu v} \hat{S}_{1\mu} \hat{S}_{2v} \quad (\mu, v = x, y, z) 6pt$$
$$= J_{xx}\hat{S}_{1x}\hat{S}_{2x} + J_{xy}\hat{S}_{1x}\hat{S}_{2y} + J_{xz}\hat{S}_{1x}\hat{S}_{2z}$$
$$+ J_{yx}\hat{S}_{1y}\hat{S}_{2x} + J_{yy}\hat{S}_{1y}\hat{S}_{2y} + J_{yz}\hat{S}_{1y}\hat{S}_{2z}$$
$$+ J_{zx}\hat{S}_{1z}\hat{S}_{2x} + J_{zy}\hat{S}_{1z}\hat{S}_{2y} + J_{zz}\hat{S}_{1z}\hat{S}_{2z}$$
$$= (\hat{S}_{1x} \quad \hat{S}_{1y} \quad \hat{S}_{1z}) \begin{pmatrix} J_{xx} & J_{xy} & J_{xz} \\ J_{yx} & J_{yy} & J_{yz} \\ J_{zx} & J_{zy} & J_{zz} \end{pmatrix} \begin{pmatrix} \hat{S}_{2x} \\ \hat{S}_{2y} \\ \hat{S}_{2z} \end{pmatrix}$$
$$= \hat{S}_1 \cdot J \cdot \hat{S}_2 \tag{3.4}$$

and showed that this expression is equivalent to Eq. (3.1). For example, the Heisenberg Hamiltonian is written as [5]

$$\hat{H}_{\text{iso}} = -J \ \hat{\boldsymbol{S}}_1 \cdot \hat{\boldsymbol{S}}_2$$
$$= \frac{1}{3}(J_{xx} + J_{yy} + J_{zz})(\hat{S}_{1x}\hat{S}_{2x} + \hat{S}_{1y}\hat{S}_{2y} + \hat{S}_{1z}\hat{S}_{2z}) \tag{3.5}$$

so that $J = -\frac{1}{3}(J_{xx} + J_{yy} + J_{zz})$. (The sign convention for J used in the present work is opposite to that employed in Ref. [5]). The eigenstates $|S \ Ms\rangle$ of this isotropic Hamiltonian were discussed in some detail in the previous section.

3.1. Antisymmetric interactions

In terms of the $J_{\mu v}$ parameters the antisymmetric Hamiltonian $\hat{H}_{\text{anti}}$ is expressed as [5]

$$\hat{H}_{\text{anti}} = \frac{1}{2}(J_{yz} - J_{zy})(\hat{S}_{1y}\hat{S}_{2z} - \hat{S}_{1z}\hat{S}_{2y})$$
$$+ \frac{1}{2}(J_{zx} - J_{xz})(\hat{S}_{1z}\hat{S}_{2x} - \hat{S}_{1x}\hat{S}_{2z})$$
$$+ \frac{1}{2}(J_{xy} - J_{yx})(\hat{S}_{1x}\hat{S}_{2y} - \hat{S}_{1y}\hat{S}_{2x})$$
$$= D_x(\hat{S}_{1y}\hat{S}_{2z} - \hat{S}_{1z}\hat{S}_{2y}) + D_y(\hat{S}_{1z}\hat{S}_{2x} - \hat{S}_{1x}\hat{S}_{2z})$$
$$+ D_z(\hat{S}_{1x}\hat{S}_{2y} - \hat{S}_{1y}\hat{S}_{2x})$$
$$= (D_x \quad D_y \quad D_z) \begin{pmatrix} \begin{vmatrix} \hat{S}_{1y} & \hat{S}_{1z} \\ \hat{S}_{2y} & \hat{S}_{2z} \end{vmatrix} \\ \begin{vmatrix} \hat{S}_{1z} & \hat{S}_{1x} \\ \hat{S}_{2z} & \hat{S}_{2x} \end{vmatrix} \\ \begin{vmatrix} \hat{S}_{1x} & \hat{S}_{1y} \\ \hat{S}_{2x} & \hat{S}_{2y} \end{vmatrix} \end{pmatrix}$$
$$= \boldsymbol{D} \cdot (\hat{\boldsymbol{S}}_1 \times \hat{\boldsymbol{S}}_2), \tag{3.6}$$

where $D_x = \frac{1}{2}(J_{yz} - J_{zy})$, $D_y = \frac{1}{2}(J_{zx} - J_{xz})$ and $D_z = \frac{1}{2}(J_{xy} - J_{yx})$. The antisymmetric vector coupling constant $\boldsymbol{D}$ between two spin sites A and B has the following properties [4,41]:

(a) When a center of inversion is located at the midpoint between A and B, $\boldsymbol{D} = 0$.
(b) When a mirror plane perpendicular to AB bisects AB, $\boldsymbol{D}$ is parallel to the mirror plane.
(c) When there is a mirror plane including A and B, $\boldsymbol{D}$ is perpendicular to the mirror plane.
(d) When a two-fold rotation axis perpendicular to AB passes through the midpoint of AB, $\boldsymbol{D}$ is perpendicular to the two-fold axis.
(e) When there is an n-fold axis ($n \geqslant 2$) along AB, $\boldsymbol{D}$ is parallel to AB.

If a coordinate system is chosen such that the z-axis is parallel to the vector $\boldsymbol{D}$, then $D_x = D_y = 0$. Thus by using the notation $D = D_z = |\boldsymbol{D}|$, the Hamiltonian $\hat{H}_{\text{anti}}$ is simplified as [5]

$$\hat{H}_{\text{anti}} = D_z(\hat{S}_{1x}\hat{S}_{2y} - \hat{S}_{1y}\hat{S}_{2x}) = D_z(\hat{S}_1^+\hat{S}_2^- - \hat{S}_1^-\hat{S}_2^+)$$
$$= D_z(\hat{S}_{1x}\hat{S}_{2y} - \hat{S}_{1y}\hat{S}_{2x}). \tag{3.7}$$

When we consider only isotropic interactions using the Hamiltonian $\hat{H}_{HDVV}$, the spin states $|S \ Ms\rangle$ with different Ms values are degenerate with energy $-\frac{1}{2}J[S(S + 1) - S_1(S_1 + 1) - S_2(S_2 + 1)]$ (Section 2.1.1). This degeneracy is lifted when both isotropic and antisymmetric interactions are included using the

Hamiltonian $\hat{H}_{\mathrm{iso/anti}} = \hat{H}_{\mathrm{iso}} + \hat{H}_{\mathrm{anti}}$, because spin states $|S \ Ms\rangle$ with different S values can interact through $\hat{H}_{\mathrm{anti}}$. The interaction between eigenstates $|S \ Ms\rangle$ and $|S' \ Ms'\rangle$ is determined by the matrix elements [5] where $Ms_1 + Ms_2 = Ms$. These matrix elements have the following properties [5]:

$$
\begin{aligned}
&\langle S' \quad Ms'|\hat{H}_{\mathrm{anti}}|S \quad Ms\rangle \\
&= \frac{i}{2}D\langle S' \quad Ms'|\hat{S}_1^+\hat{S}_2^- - \hat{S}_1^-\hat{S}_2^+|S \quad Ms\rangle \\
&= \frac{i}{2}D \sum_{Ms_1=-S_1}^{S_1} \sum_{Ms_2=-S_2}^{S_2} C(S_1 Ms_1, S_2 Ms_2; SMs) \\
&\quad \times [C(S_1 Ms_1 + 1, S_2 Ms_2 - 1; S'Ms)\sqrt{(S_1 + Ms_1 + 1)(S_1 - Ms_1)(S_2 - Ms_2 + 1)(S_2 + Ms_2)} \\
&\quad - C(S_1 Ms_1 - 1, S_2 Ms_2 + 1; S'Ms)\sqrt{(S_1 - Ms_1 + 1)(S_1 + Ms_1)(S_2 + Ms_2 + 1)(S_2 - Ms_2)}],
\end{aligned} \tag{3.8}
$$

(a) $\langle S \quad Ms|\hat{H}_{\mathrm{anti}}|S \quad Ms\rangle = 0.$
(b) $\langle S' \quad Ms'|\hat{H}_{\mathrm{anti}}|S \quad Ms\rangle = 0$, when $Ms' \neq Ms$.
(c) $\langle S' \quad Ms|\hat{H}_{\mathrm{anti}}|S \quad Ms\rangle = 0$, when $|S' - S| \geqslant 3$ or when $S' + S$ is even.
(d) $\langle S' - Ms|\hat{H}_{\mathrm{anti}}|S - Ms\rangle = (-1)^{S'+S+1}\langle S' \quad Ms|\hat{H}_{\mathrm{anti}}|S \quad Ms\rangle.$

All the non-zero matrix elements $\langle S' \quad Ms'|\hat{H}_{\mathrm{anti}}|S \quad Ms\rangle$ for spin dimers with $S_1 = S_2 = 1/2, 1, 3/2, 2$ and $5/2$ (i.e., $M = N = 1-5$) are listed in Appendix A. Using these matrix elements, the eigenvalues of $\hat{H}_{\mathrm{iso/anti}}$ can be determined in terms of the ratio $x = |D/J|$. The eigenvalues of $\hat{H}_{\mathrm{iso/anti}}$ have analytical expressions for $S_1 = S_2 = 1/2$ and 1. This is not true for most cases of $S_1 = S_2 = 3/2, 2$ and $5/2$. To provide pseudo-analytical expressions for the latter, we first determine the eigenvalues of $\hat{H}_{\mathrm{iso/anti}}$ numerically by diagonalizing its matrix representation as a function of x and then fit the resulting eigenvalues with the polynomial function of x^2 of the following type

$$E(x) = J(c_0 + c_1 x^2 + c_2 x^4 + c_3 x^6 + c_4 x^8) \tag{3.9}$$

for various regions of x (i.e., 0.0–0.5, 0.5–1.0, 1.0–1.5, and 1.5–2.0). The eigenvalues of $\hat{H}_{\mathrm{iso/anti}}$ that we obtained for $S_1 = S_2 = 1/2, 1, 3/2, 2$ and $5/2$ in this way are summarized in Appendix B, and are plotted as a function of $x = |D/J|$ in Fig. 5.

For the sake of simplicity, the quantum numbers S and Ms were used in Appendix B and Fig. 5 to label the eigenstates of $\hat{H}_{\mathrm{iso/anti}}$ even when the states $|S \ Ms\rangle$ are not eigenstates of $\hat{H}_{\mathrm{iso/anti}}$. For example, for $S_1 = S_2 = 1/2$, the eigenstates $|0 \ 0\rangle$ and $|1 \ 0\rangle$ of $\hat{H}_{\mathrm{iso}}$ interact through $\hat{H}_{\mathrm{anti}}$ so that the eigenstates of $\hat{H}_{\mathrm{iso/anti}}$ become linear combinations of $|0 \ 0\rangle$ and $|1 \ 0\rangle$. If $x \ll 1$, the mixing between $|0 \ 0\rangle$ and $|1 \ 0\rangle$ is weak so that one eigensate of $\hat{H}_{\mathrm{iso/anti}}$ is represented largely by $|0 \ 0\rangle$, and the other eigenstate largely by $|1 \ 0\rangle$. Consequently, the use of the notation $E(S \ Ms)$ for an eigenstate of $\hat{H}_{\mathrm{iso/anti}}$ indicates that the spin state $|S \ Ms\rangle$ is its major component when $x \ll 1$, if it interacts with other $|S' \ Ms\rangle$ states.

3.2. Anisotropic interactions

There are two ways of discussing anisotropic interactions between spins. As shown by Erdös [5], one may derive an explicit form of a Hamiltonian designed to describe anisotropic interactions starting from the general expression of the spin Hamiltonian $\hat{H} = \hat{\boldsymbol{S}}_1 \cdot J \cdot \hat{\boldsymbol{S}}_2$ given in Eq. (3.4). This formal approach does not provide insight into how magnetic isotropy comes about. Alternatively, one may first determine the ground orbital state of a magnetic ion under the effect of the crystal field and spin–orbit coupling and then examine the spin exchange interactions between adjacent ions on the basis of their ground orbital states. Ultimately, the two approaches lead to an identical form of a Hamiltonian needed to discuss anisotropic interactions. Nevertheless, the second approach is more informative because anisotropic properties of a magnetic solid at low temperatures are primarily determined by the ground orbital states of its magnetic ions.

3.2.1. Intersite interactions

In terms of the $J_{\mu\nu}$ parameters the anisotropic Hamiltonian $\hat{H}_{\mathrm{aniso}}$ is written as [5]

$$
\begin{aligned}
\hat{H}_{\mathrm{aniso}} = {} & (J_{xx} + J)\hat{S}_{1x}\hat{S}_{2x} + \frac{1}{2}(J_{xy} + J_{yx})\hat{S}_{1x}\hat{S}_{2y} \\
& + \frac{1}{2}(J_{xz} + J_{zx})\hat{S}_{1x}\hat{S}_{2z} + \frac{1}{2}(J_{xy} + J_{yx})\hat{S}_{1y}\hat{S}_{2x} \\
& + (J_{yy} + J)\hat{S}_{1y}\hat{S}_{2y} + \frac{1}{2}(J_{yz} + J_{zy})\hat{S}_{1z}\hat{S}_{2y} \\
& + \frac{1}{2}(J_{xz} + J_{zx})\hat{S}_{1z}\hat{S}_{2x} + \frac{1}{2}(J_{yz} + J_{zy})\hat{S}_{1z}\hat{S}_{2y} \\
& + (J_{zz} + J)\hat{S}_{1z}\hat{S}_{2z},
\end{aligned}
$$

$$(\hat{S}_{1x} \quad \hat{S}_{1y} \quad \hat{S}_{1z})$$

$$\times \begin{pmatrix} (J_{xx} + J) & \frac{1}{2}(J_{xy} + J_{yx}) & \frac{1}{2}(J_{xz} + J_{zx}) \\ \frac{1}{2}(J_{xy} + J_{yx}) & (J_{yy} + J) & \frac{1}{2}(J_{yz} + J_{zy}) \\ \frac{1}{2}(J_{xz} + J_{zx}) & \frac{1}{2}(J_{yz} + J_{zy}) & (J_{zz} + J) \end{pmatrix}$$

$$\times \begin{pmatrix} \hat{S}_{2x} \\ \hat{S}_{2y} \\ \hat{S}_{2z} \end{pmatrix} = \hat{\boldsymbol{S}}_1 \cdot \boldsymbol{\Gamma} \cdot \hat{\boldsymbol{S}}_2, \tag{3.10}$$

where $\boldsymbol{\Gamma}$ is the symmetric anisotropic tensor coupling constant. Under crystal symmetries in which the matrix elements $\Gamma_{xy} = \Gamma_{yz} = \Gamma_{zx} = 0$, this Hamiltonian is simplified as [5]

$$\hat{H}_{\text{aniso}} = (J_{xx} + J)\hat{S}_{1x}\hat{S}_{2x} + (J_{yy} + J)\hat{S}_{1y}\hat{S}_{2y}$$
$$+ (J_{zz} + J)\hat{S}_{1z}\hat{S}_{2z}. \tag{3.11a}$$

After some algebra the above equation is modified as

$$\hat{H}_{\text{aniso}} = \frac{1}{4}(J_{xx} - J_{yy})(\hat{S}_1^+ \hat{S}_2^+ + \hat{S}_1^- \hat{S}_2^-)$$
$$+ (J_{zz} + J)[\hat{S}_{1z}\hat{S}_{2z} - \frac{1}{4}(\hat{S}_1^+ \hat{S}_2^- + \hat{S}_1^- \hat{S}_2^+)]. \tag{3.11b}$$

This expression corresponds to Eq. (8.4) of Ref. [5] (this latter equation has a typo, i.e., the term "J_{zz}" should be replaced with "$(J_{zz} - J)$" under the sign convention of J employed in Ref. [5]. This equation has been used without correction [30,32]).

The eigenstates $|S \quad Ms\rangle$ of $\hat{H}_{\text{iso}}$ can interact via $\hat{H}_{\text{aniso}}$. Non-zero matrix elements $\langle S' \quad Ms|\hat{H}_{\text{aniso}}|S \quad Ms\rangle$ are [5]

$$\langle S' \quad Ms|\hat{H}_{\text{aniso}}|S \quad Ms\rangle$$
$$= (J_{zz} + J) \sum_{Ms_1=-S_1}^{S_1} \sum_{Ms_2=-S_2}^{S_2} C(S_1 Ms_1, S_2 Ms_2; SMs)$$
$$\times [Ms_1 Ms_2 C(S_1 Ms_1, S_2 Ms_2; S'Ms)$$
$$- \frac{1}{4} C(S_1 Ms_1 + 1, S_2 Ms_2 - 1; S'Ms)$$
$$\times \sqrt{(S_1 + Ms_1)(S_1 - Ms_1)(S_2 + Ms_2)(S_2 - Ms_2 + 1)}$$
$$- \frac{1}{4} C(S_1 Ms_1 - 1, S_2 Ms_2 + 1; S'Ms)$$
$$\times \sqrt{(S_1 + Ms_1)(S_1 - Ms_1 + 1)(S_2 + Ms_2 + 1)(S_2 - Ms_2)}] \tag{3.12a}$$

and

$$\langle S' \quad Ms \pm 2|\hat{H}_{\text{aniso}}|S \quad Ms\rangle = \frac{1}{4}(J_{xx} - J_{yy})$$
$$\times \sum_{Ms_1=-S_1}^{S_1} \sum_{Ms_2=-S_2}^{S_2} C(S_1 Ms_1, S_2 Ms_2; SMs)$$
$$\times C(S_1 Ms_1 \pm 1, S_2 Ms_2 \pm 1; S'Ms \pm 2)$$
$$\times \sqrt{(S_1 \pm Ms_1 + 1)(S_1 \mp Ms_1)(S \pm Ms_2 + 1)(S_2 \mp Ms_2)}, \tag{3.12b}$$

where $Ms_1 + Ms_2 = Ms$. Thus, for $S_1 = S_2 = 1/2$, for example, the eigenvalues of the Hamiltonian $\hat{H}_{\text{iso/aniso}} + \hat{H}_{\text{iso}} + \hat{H}_{\text{aniso}}$ are given by

$$E(0 \quad 0) = \frac{3}{4}J,$$

$$E(1 \quad 0) = -\frac{3}{4}J - \frac{1}{2}J_{zz},$$

$$E(1 \quad 1) = \frac{1}{4}J_{zz} + \frac{1}{4} + (J_{xx} - J_{yy}),$$

$$E(1 \quad -1) = \frac{1}{4}J_{zz} - \frac{1}{4}(J_{xx} - J_{yy}). \tag{3.13}$$

It is clear from Eq. (3.11a) that the anisotropic term $\hat{H}_{\text{aniso}}$ vanishes when $J_{xx} = J_{yy} = J_{zz} = -J$. Under this condition, $E(0 \quad 0) = \frac{3}{4}J$, and $E(1 \quad 0) = E(1 \quad 1) = E(1 \quad -1) = -\frac{1}{4}J$, as expected.

To examine the effect of anisotropic interactions in more detail for spin dimers with $S_1 = S_2 = 1/2 - 5/2$, it is convenient to simplify the expression of $\hat{H}_{\text{iso/aniso}}$ further. From Eqs. (3.5) and (3.11b), $\hat{H}_{\text{iso/aniso}}$ is rewritten as

$$\hat{H}_{\text{iso/aniso}} = J_{xx}\hat{S}_{1x}\hat{S}_{2x} + J_{yy}\hat{S}_{1y}\hat{S}_{2y} + J_{zz}\hat{S}_{1z}\hat{S}_{2z}. \tag{3.14a}$$

Under the condition that $J_{xx} = J_{yy}$, this equation becomes

$$\hat{H}_{\text{iso/aniso}} = -J[\alpha\hat{S}_{1z}\hat{S}_{2z} + \beta(\hat{S}_{1x}\hat{S}_{2x} + \hat{S}_{1y}\hat{S}_{2y})], \tag{3.14b}$$

$$= -J[\alpha\hat{S}_{1z}\hat{S}_{2z} + \frac{1}{2}\beta(\hat{S}_1^+ \hat{S}_2^- + \hat{S}_1^- \hat{S}_2^+)] \tag{3.14c}$$

with $\alpha J = -J_{zz}$ and $\beta J = -J_{xx} = -J_{yy}$. Then the coefficients α and β account for various cases of anisotropic exchange interactions. For example, an Ising Hamiltonian results when $\alpha = 1$ and $\beta = 0$, an XY Hamiltonian when $\alpha = 0$ and $\beta = 1$, and a Heisenberg Hamiltonian when $\alpha = 1$ and $\beta = 1$. On the basis of Eq. (3.14c) we evaluate the matrix elements $\langle S' \quad Ms|\hat{H}_{\text{iso/aniso}}|S \quad Ms\rangle$ as a function of α and β. The non-zero matrix elements for the cases $S_1 = S_2 = 1/2, 1, 3/2, 2$ and $5/2$ are summarized in Appendix C, and the associated eigenvalues of $\hat{H}_{\text{iso/aniso}}$ in Appendix D. Fig. 6 shows how the eigenvalues of the isotropic Hamiltonian ($\alpha = \beta = 1$) vary as the strength of anisotropic interactions is gradually increased towards the Ising Hamiltonian ($\alpha = 1 \to 0$), and toward the XY Hamiltonian ($\beta = 1 \to 0$).
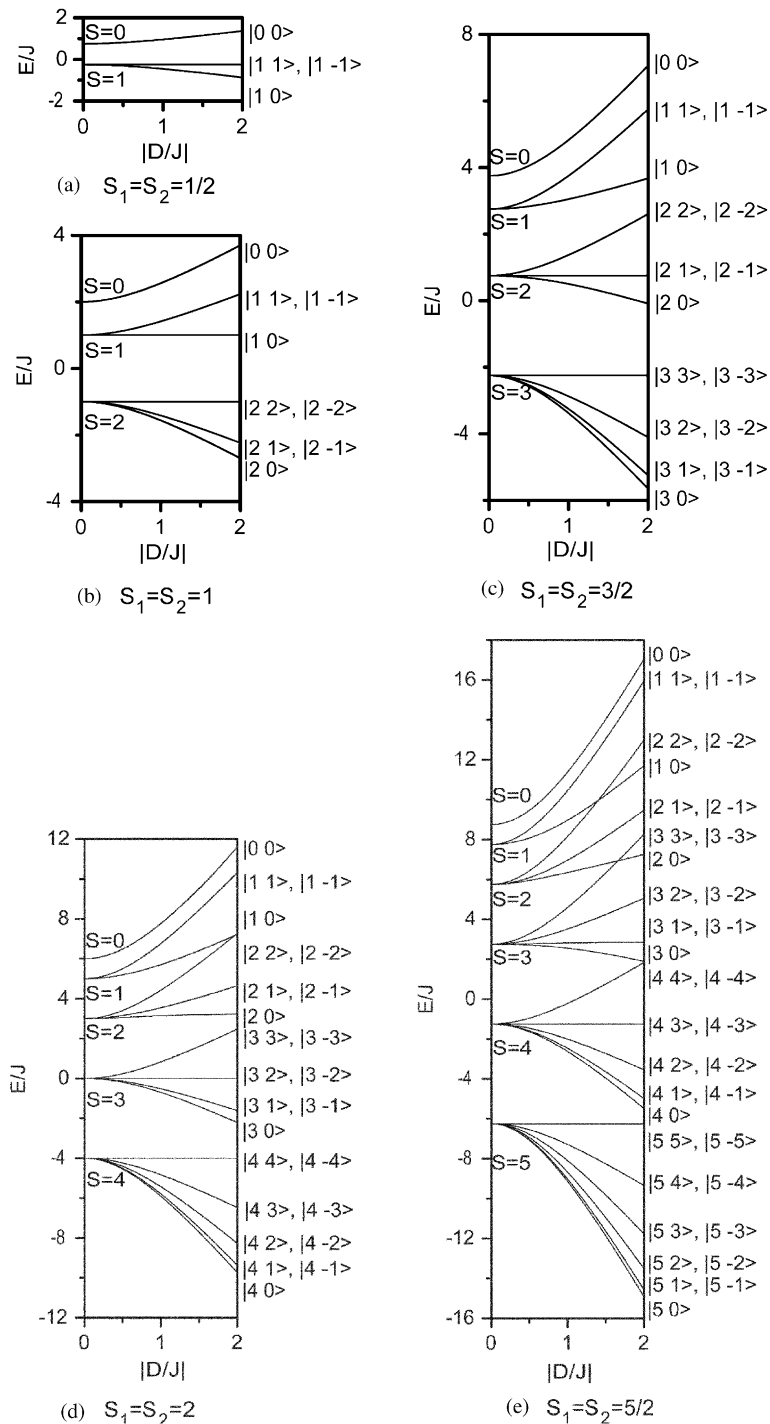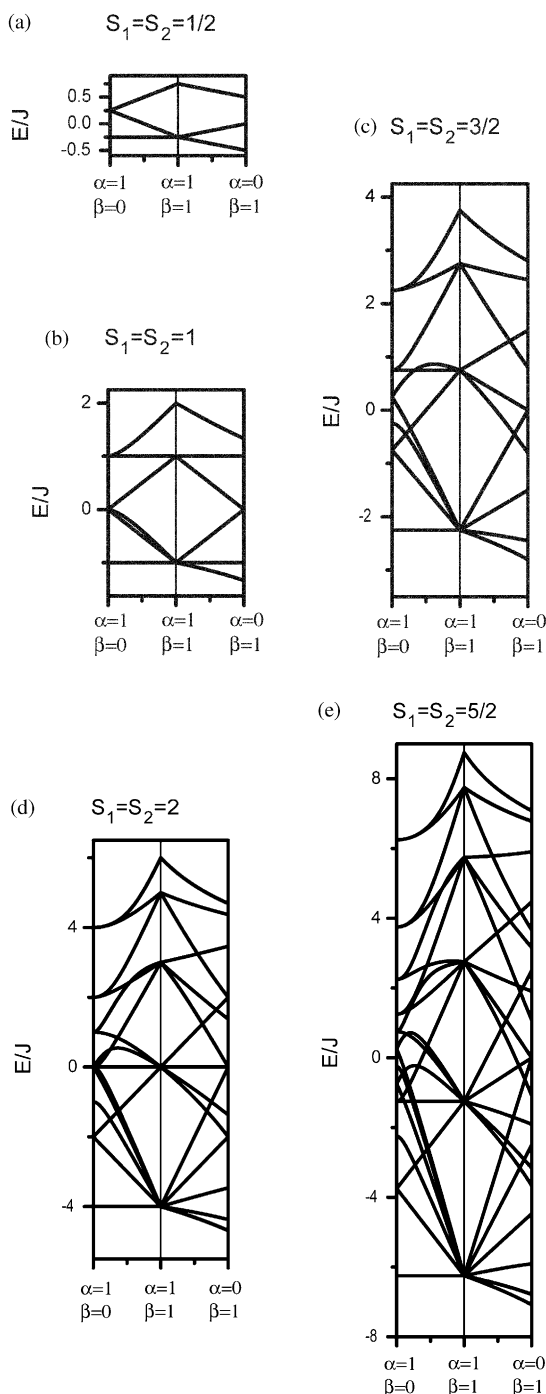
Fig. 5. Eigenvalues of the Hamiltonian $\hat{H}_{\text{iso/anti}}$ for a spin dimer with $M = N = 1-5$ as a function of $x = |D/J|$. In this plot the value of J was assumed to be positive.

It is of interest to rewrite Eq. (3.14b) as

$$\hat{H}_{\text{iso/aniso}} = -J\alpha\hat{S}_1 \cdot \hat{S}_2 + J(\alpha - \beta)(\hat{S}_{1x}\hat{S}_{2x} + \hat{S}_{1y}\hat{S}_{2y}).$$
$$(3.14d)$$

The ratio $(\alpha - \beta)/\alpha$ plays an important role in describing magnetic systems that exhibit strong magnetic anisotropy. This will be discussed further in Section 3.2.3.

3.2.2. Single ion anisotropy

The Hamiltonian describing a single ion can be divided into three components, i.e., $\hat{H}_{\text{free-ion}}$, $\hat{H}_{\text{cf}}$ and $\hat{H}_{\text{so}}$. The $\hat{H}_{\text{free-ion}}$ term represents the Hamiltonian of a free ion, $\hat{H}_{\text{cf}}$ the crystal field, and $\hat{H}_{\text{so}} = \lambda\hat{\boldsymbol{L}} \cdot \hat{\boldsymbol{S}}$ the spin–orbit coupling (here $\hat{\boldsymbol{L}}$ represents the orbital angular momentum operator). Suppose that the eigenstates of $\hat{H}_1 = \hat{H}_{\text{free-ion}} + \hat{H}_{\text{cf}}$ were determined, and $|n\rangle$ and $|m\rangle$

(a) $S_1 = S_2 = 1/2$

(b) $S_1 = S_2 = 1$

(c) $S_1 = S_2 = 3/2$

(d) $S_1 = S_2 = 2$

(e) $S_1 = S_2 = 5/2$

Fig. 6. Eigenvalues of the Hamiltonian $\hat{H}_{\text{iso/aniso}}$ for a spin dimer with $M = N = 1-5$ as a function of the coefficients α and β that convert the Heisenberg Hamiltonian ($\alpha = 1$, $\beta = 1$) into the Ising Hamiltonian ($\alpha = 1$, $\beta = 0$) and the XY Hamiltonian ($\alpha = 0$, $\beta = 1$). In this plot the value of J was assumed to be positive.

are the ground and excited states of $\hat{H}_1$ with the eigenvalues E_n and E_m, respectively. By considering how the spin–orbit coupling affects these states, the Hamiltonian describing the anisotropy of a single

magnetic ion is given by

$$\hat{\boldsymbol{S}} \cdot \boldsymbol{\Lambda} \cdot \hat{\boldsymbol{S}}$$

$$= (\hat{S}_x \quad \hat{S}_y \quad \hat{S}_z) \begin{pmatrix} \Lambda_{xx} & \Lambda_{xy} & \Lambda_{xz} \\ \Lambda_{yx} & \Lambda_{yy} & \Lambda_{yz} \\ \Lambda_{zx} & \Lambda_{zy} & \Lambda_{zz} \end{pmatrix} \begin{pmatrix} \hat{S}_x \\ \hat{S}_y \\ \hat{S}_z \end{pmatrix}, \quad (3.15)$$

where Λ is a symmetric and traceless tensor (i.e., $\Lambda_{\mu v} = \Lambda_{v\mu}$, and $\sum_\mu \Lambda_{\mu\mu} = 0$), and the $\Lambda_{\mu v}$ elements ($\mu, v = x, y, z$) are [33, Chapter 2].

$$\Lambda_{\mu v} = \lambda^2 \sum_{m \neq n} \frac{\langle n | \hat{L}_\mu | m \rangle \langle m | \hat{L}_v | n \rangle}{E_n - E_m}. \quad (3.16)$$

If all the off-diagonal elements $\Lambda_{\mu v}$ ($\mu \neq v$) are neglected, $\hat{\boldsymbol{S}} \cdot \boldsymbol{\Lambda} \cdot \hat{\boldsymbol{S}}$ becomes

$$\hat{\boldsymbol{S}} \cdot \boldsymbol{\Lambda} \cdot \hat{\boldsymbol{S}} \approx \Lambda_{xx} \hat{S}_x^2 + \Lambda_{yy} \hat{S}_y^2 + \Lambda_{zz} \hat{S}_z^2. \quad (3.17a)$$

This equation is rewritten as

$$\hat{\boldsymbol{S}} \cdot \boldsymbol{\Lambda} \cdot \hat{\boldsymbol{S}} = \left(\frac{3}{2} \Lambda_{zz}\right)\left(\hat{S}_z^2 - \frac{1}{3}\hat{S}^2\right)$$
$$+ \frac{1}{2}(\Lambda_{xx} - \Lambda_{yy})(\hat{S}_x^2 - \hat{S}_y^2) \quad (3.17b)$$

which is derived from Eqs. (3.11b) after replacing the $J_{\mu\mu} + J$ term with $\Lambda_{\mu\mu}$ ($\mu = x, y, z$) under the constraint that the two spin sites are identical. The Hamiltonian $\hat{\boldsymbol{S}} \cdot \boldsymbol{\Lambda} \cdot \hat{\boldsymbol{S}}$ describes the anisotropic interaction of a single magnetic ion. Since the $\hat{S}^2$ term describes isotropic interactions, it may be omitted from Eq. (3.17b). Then, $\hat{\boldsymbol{S}} \cdot \boldsymbol{\Lambda} \cdot \hat{\boldsymbol{S}}$ is simplified as

$$\hat{\boldsymbol{S}} \cdot \boldsymbol{\Lambda} \cdot \hat{\boldsymbol{S}} \simeq \frac{3}{2} \Lambda_{zz} \hat{S}_z^2 + \frac{1}{2}(\Lambda_{xx} - \Lambda_{yy})(\hat{S}_x^2 - \hat{S}_y^2)$$
$$= D' \hat{S}_z^2 + E'(\hat{S}_x^2 - \hat{S}_y^2), \quad (3.17c)$$

where $D' = \frac{3}{2} \Lambda_{zz}$, and $E' = \frac{1}{2}(\Lambda_{xx} - \Lambda_{yy})$. The Hamiltonian $\hat{\boldsymbol{S}} \cdot \boldsymbol{\Lambda} \cdot \hat{\boldsymbol{S}}$ is used to describe single-ion anisotropy and zero-field splitting [35, Sections 2.5 and 3.1]. This Hamiltonian acts on pure spin states of a single ion (i.e., the spin parts of the eigenstates of $\hat{H}_1 = \hat{H}_{\text{free-ion}} + \hat{H}_{\text{cf}}$) and accounts for the effect of spin–orbit coupling in terms of the parameters D' and E'.

3.2.3. Pseudo-spin approach to magnetic anisotropy

In understanding the phenomenon of strong anisotropy in magnetic solids at low temperatures, it is critical to know first the ground orbital state of each magnetic ion under the influence of the crystal field and spin–orbit coupling and then consider how adjacent ions interact in terms of their ground orbital states [42–44]. In this section we briefly discuss the pseudo-orbital pseudo-spin approach introduced by Lines [42] to explain the strong magnetic anisotropy of $CoCl_2$.

The building blocks of $CoCl_2$ are layers of composition $CoCl_2$ that are made up of edge-sharing $CoCl_6$ octahedra [45]. Each Co^{2+} ion, located at the center of a weakly distorted $CoCl_6$ octahedron, is in the high-spin

state. Thus the local d-block electronic structure of each Co^{2+} ion is described by the electron configuration $(t_{2g})^5(e_g)^2$ with three unpaired spins. The weak distortion of each $CoCl_6$ octahedron is trigonal in symmetry, namely, it is slightly flattened along the three-fold rotational axis that is perpendicular to the $CoCl_2$ layer [45]. To a first approximation, therefore, each Co^{2+} ion of $CoCl_2$ is in a cubic crystal field due to its octahedral coordination [33, Chapter 2, 42]. The weak distortion of each $CoCl_6$ octahedron adds a weak trigonal crystal field to each Co^{2+} ion [42]. The interactions between adjacent Co^{2+} ions leading to the magnetic anisotropy of $CoCl_2$ at low temperatures are primarily determined by the ground orbital state of each Co^{2+} ion. Therefore, it is essential to identify the nature of this ground state.

The ground orbital state of a free Co^{2+} (d^7) ion is ^4F (i.e., $L = 3$, $S = \frac{3}{2}$). In a cubic crystal field this state is split into $^4A_2$, $^4T_2$ and $^4T_1$ states. Of the three states, the ground orbital state is $^4T_1$, which is described by [46]

$$\phi_0 = \frac{2}{3}|3 \quad 0\rangle - \frac{1}{3}\sqrt{\frac{5}{2}}(|3 \quad 3\rangle - |3 \quad 3\rangle),$$

$$\phi_{+1} = \sqrt{\frac{5}{6}}|3 \quad 2\rangle + \sqrt{\frac{1}{6}}|3 \quad -1\rangle,$$

$$\phi_{-1} = \sqrt{\frac{5}{6}}|3 \quad -2\rangle - \sqrt{\frac{1}{6}}|3 \quad 1\rangle, \tag{3.18}$$

where the orbital momentum states $|L \quad m_L\rangle$ refer to those of a free ion. In terms of the momentum operator $\hat{L}_z$ of a free ion, it can be easily shown [42] that

$$\langle\phi_1|\hat{L}_z|\phi_1\rangle = -\frac{3}{2}, \quad \langle\phi_{-1}|\hat{L}_z|\phi_{-1}\rangle = \frac{3}{2},$$

$$\langle\phi_0|\hat{L}_z|\phi_0\rangle = 0. \tag{3.19}$$

In addition, all the matrix elements of $\hat{L}$ between the three states ϕ_0, ϕ_{+1} and ϕ_{-1} are exactly the same as those of $-\frac{3}{2}\hat{L}$ between the corresponding P (i.e., $L = 1, m_L = 1, 0, -1$) states of a free ion. Therefore, as far as the orbital triplet state $^4T_1$ is concerned, the orbital momentum of a Co^{2+} ion in a cubic crystal field can be discussed using the pseudo-orbital operator $-\frac{3}{2}\hat{L}$ with the effective orbital states $|L' \quad m_{L'}\rangle$, where $L' = 1$ and $m_{L'} = 1, 0, -1$ as if the Co^{2+} ion is a free ion [42,43]. Then, the orbital/spin states of $^4T_1$ can be represented by $|L' \quad m_{L'}\rangle|S \quad m_S\rangle$. Here $S = 3/2$ so that $m_S = 3/2, 1/2, -1/2, -3/2$. Because the L' and S values are fixed, the notations $|L' \quad m_{L'}\rangle|S \quad m_S\rangle$ can be simplified as $|m_{L'} \quad m_S\rangle$ [42]. Consequently, the ground orbital triplet state $^4T_1$ of a Co^{2+} ion in a cubic field is described by 12 $|m_{L'} \quad m_S\rangle$ functions ($m_{L'} = 1, 0, -1$; $m_S = 3/2, 1/2, -1/2, -3/2$).

As mentioned above, each Co^{2+} ion of $CoCl_2$ is under a weak trigonal crystal field due to the slight trigonal distortion of each $CoCl_6$ octahedron. This distortion and the spin–orbit coupling will split the 12 $|m_{L'} \quad m_S\rangle$ states of each Co^{2+} ion. To find the ground state of these split levels, we first note that in a trigonal crystal field the orbital triplet is split into an orbital doublet and an orbital singlet with energy separation δ. This is described by the operator $\hat{H}_{cf}$ defined by [42]

$$\hat{H}_{cf} = -\delta\left(\hat{L}_z^2 - \frac{2}{3}\right) \tag{3.20}$$

which places the states $|1 \quad m_S\rangle$ and $|-1 \quad m_S\rangle$ at $-\frac{1}{3}\delta$, and the state $|0 \quad m_S\rangle$ at $\frac{2}{3}\delta$. In describing the spin–orbit interaction of a Co^{2+} ion in a trigonal distortion in terms of $\hat{H}_{so}$, the pure orbital momentum operator $\hat{L}$ is replaced with the pseudo-orbital operator $-\frac{3}{2}k\hat{L}$, where the constant k (slightly smaller than unity) [43,47] is included to reflect the fact that a Co^{2+} ion of $CoCl_2$ in bonding interaction with the surrounding Cl^- ions has a smaller angular momentum (in magnitude) than does a free Co^{2+} ion. The latter observation comes about because the $3d$ orbitals of a Co^{2+} ion in the magnetic orbitals of $CoCl_2$ have a weight smaller than unity. Thus the Hamiltonian $\hat{H}_{so}$ is modified as

$$\hat{H}_{so} = -\frac{3}{2}k\lambda\hat{L}\cdot\hat{S}. \tag{3.21}$$

Then, the combined Hamiltonian $\hat{H}' = \hat{H}_{cf} + \hat{H}_{so}$ can be employed to find how the 12 $|m_{L'} \quad m_S\rangle$ states of $^4T_1$ are split by the trigonal distortion and the spin–orbit interaction [42].

$$\hat{H}' = -\delta\left(\hat{L}_z^2 - \frac{2}{3}\right) - \frac{3}{2}k\lambda\hat{L}\cdot\hat{S}$$

$$= -\delta\left(\hat{L}_z^2 - \frac{2}{3}\right) - \frac{3}{2}k\lambda\left[\hat{L}_z\hat{S}_z + \frac{1}{2}(\hat{L}^+\hat{S}^- + \hat{L}^-\hat{S}^+)\right]. \tag{3.22}$$

The matrix elements of $\hat{H}'$ for $|m_{L'} \quad m_S\rangle$ are found to be the same as those for $|-m_{L'} \quad -m_S\rangle$, that is, the 12 $|m_{L'} \quad m_S\rangle$ states are split into six spin doublets (i.e., six Kramers' doublets) [42]. Furthermore, calculations of the eigenvalues of $\hat{H}'$ as a function of the $\delta/k\lambda$ ratio reveal that the ground Kramers' doublet state is described by the two functions [42]

$$\psi_+ = c_1\left|-1 \quad \frac{3}{2}\right\rangle + c_2\left|0 \quad \frac{1}{2}\right\rangle + c_3\left|1 \quad -\frac{1}{2}\right\rangle,$$

$$\psi_- = c_1\left|1 \quad -\frac{3}{2}\right\rangle + c_2\left|0 \quad -\frac{1}{2}\right\rangle + c_3\left|-1 \quad \frac{1}{2}\right\rangle, \tag{3.23}$$

where the coefficients c_1, c_2 and c_3 are determined by the $\delta/(k\lambda)$ value applicable to $CoCl_2$.

Since the ground orbital state of each Co^{2+} ion in $CoCl_2$ has been identified, we are in a position to describe the magnetic anisotropy of $CoCl_2$. First, it is necessary to examine how adjacent Co^{2+} ions interact in terms of their ground Kramers' doublet states [42]. For this purpose, Lines determined the matrix elements of the spin operators $\hat{S}_x$, $\hat{S}_y$ and $\hat{S}_z$ using ψ_+ and ψ_- as basis functions, i.e., $\langle i|\hat{S}_\mu|j\rangle$, where $i, j = \psi_+, \psi_-$ and

$\mu = x, y, z$. By use of the relationships $\hat{S}_x = (\hat{S}^+ + \hat{S}^-)/2$ and $\hat{S}_y = (\hat{S}^+ + \hat{S}^-)/2i$, it is straightforward to find the following matrix representations of $\hat{S}_x$, $\hat{S}_y$ and $\hat{S}_z$ [42].

$$\boldsymbol{S}_x = \begin{pmatrix} 0 & q \\ q & 0 \end{pmatrix}, \quad \boldsymbol{S}_y = \begin{pmatrix} 0 & -iq \\ iq & 0 \end{pmatrix}, \quad \boldsymbol{S}_z = \begin{pmatrix} p & 0 \\ 0 & p \end{pmatrix},$$

(3.24a)

where the constants q and p are given by

$$p = \frac{3}{2}c_1^2 + \frac{1}{2}c_2^2 - \frac{1}{2}c_3^2, \quad q = c_2^2 + \sqrt{3}c_1c_3. \tag{3.24b}$$

At this point it is recalled that in terms of the spin states $|\frac{1}{2}\rangle$ and $|-\frac{1}{2}\rangle$ of a single electron as basis functions, the spin-half operators $\hat{s}_x$, $\hat{s}_y$ and $\hat{s}_z$ have the matrix representations given below.

$$s_x = \frac{1}{2}\begin{pmatrix} 0 & 1 \\ 1 & 0 \end{pmatrix}, \quad s_y = \frac{1}{2}\begin{pmatrix} 0 & -i \\ i & 0 \end{pmatrix}, \quad s_z = \frac{1}{2}\begin{pmatrix} 1 & 0 \\ 0 & 1 \end{pmatrix}.$$

(3.25)

Therefore, the true spin of the ground Kramers' doublet state can be formally replaced by the pseudo-spin defined below

$$\hat{S}_x = 2q\hat{s}_x, \quad \hat{S}_y = 2q\hat{s}_y, \quad \hat{S}_z = 2p\hat{s}_z. \tag{3.26}$$

This relationship allows one to describe the anisotropic spin exchange interaction between nearest neighbor Co^{2+} ions of $CoCl_2$ formally by using the Heisenberg Hamiltonian $\hat{H} = -J\hat{S}_1 \cdot \hat{S}_2$. If the operators $\hat{S}_1$ and $\hat{S}_2$ are replaced with the pseudo-spin operators, one obtains the effective spin Hamiltonian

$$\hat{H} = -J[(2p)^2\hat{s}_{1z}\hat{s}_{2z} + (2q)^2(\hat{s}_{1x}\hat{s}_{2x} + \hat{s}_{1y}\hat{s}_{2y})]. \tag{3.27a}$$

This expression is rewritten as

$$\hat{H} = -J''(\hat{s}_1 \cdot \hat{s}_2) + D''(\hat{s}_{1x}\hat{s}_{2x} + \hat{s}_{1y}\hat{s}_{2y}) \tag{3.27b}$$

with $J'' = (2q)^2 J$ and $D'' = [(2q)^2 - (2p)^2]J$. The D''/J'' ratio can be deduced experimentally using magnetic susceptibility data, and provides a measure of the extent of the anisotropy in the spin exchange interaction. Note that Eq. (3.27b) is formally equivalent to Eq. (3.14d) with the relationship $D''/J'' = (\alpha - \beta)/\alpha$.

It is important to observe that the Heisenberg Hamiltonian $\hat{H} = -J \ \hat{S}_1 \cdot \hat{S}_2$ describes isotropic spin exchange interactions when the spin operators $\hat{S}_1$ and $\hat{S}_2$ refer to pure spin operators. However, this Hamiltonian can be employed to describe anisotropic interactions if $\hat{S}_1$ and $\hat{S}_2$ are replaced with the pseudo-spin operators, because the effect of spin–orbit coupling and crystal field has already been included in the pseudo-spin operators at each spin site. The pseudo-spin approach is convenient because the anisotropy of a magnetic system at low temperatures depends primarily on the ground orbital state of each magnetic ion, and because the ground orbital state can be easily identified by

analyzing how the crystal field and spin–orbit coupling split the ground orbital state of a free magnetic ion.

3.3. Biquadratic spin exchange

As for the isotropic spin exchange, we note that the scalar product operator $\hat{S}_1 \cdot \hat{S}_2$ is not the only possible one that commutes with the $\hat{S}^2$ operator. In particular, the operator $\hat{H}_{LQ}$ given as the sum of the bilinear and biquadratic exchange interactions,

$$\hat{H}_{LQ} = -J\hat{S}_1 \cdot \hat{S}_2 - j(\hat{S}_1 \cdot \hat{S}_2)^2 \tag{3.27}$$

also has this property. For a certain magnetic system in which both antisymmetric and anisotropic interactions are negligible, the temperature variation of the magnetic susceptibility is not well described by the Heisenberg Hamiltonian, which predicts that the energy interval between successive spin states is identical (i.e., $-JS$). In this case it has been found that the operator $\hat{H}_{LQ}$ provides an accurate description of the magnetic susceptibility [31]. The eigenstates $|S \ Ms\rangle$ of $\hat{H}_{HDVV}$ are still eigenstates of $\hat{H}_{LQ}$ with the eigenvalues

$$E(S) = -\frac{1}{2}J[S(S+1) - S_1(S_1+1) - S_2(S_2+1)]$$
$$- \frac{1}{4}j[S(S+1) - S_1(S_1+1) - S_2(S_2+1)]^2$$

(3.28a)

so that the energy interval between successive states is given by

$$E(S) - E(S-1) = -JS - jS[S^2 - S_1(S_1+1) - S_2(S_2+1)] \tag{3.28b}$$

By using Racah's irreducible tensor method, Griffith has shown a general approach to calculate the energy levels from Hamiltonian $\hat{H}_{12} = \sum_{k \geqslant 1} j_k(\hat{S}_1 \cdot \hat{S}_2)^k$ for a spin dimer and a spin trimer [31].

4. Quantitative calculations of isotropic spin exchange interactions

Isotropic spin exchange parameters of an extended magnetic solid can be quantitatively calculated using first principles electronic structure computations. Conceptually, these quantitative approaches can be classified into the "mapping" and "direct" methods. In the mapping method [10–23], the energies of several electronic states of a magnetic solid or its fragments are determined by electronic structure calculations, and the energy differences between these electronic states are mapped onto those between the corresponding spin states determined by an appropriate spin Hamiltonian. In the direct method [48–51], spin exchange parameters of a magnetic solid are directly calculated from its

ground state electronic structure on the basis of electronic band structure calculations.

4.1. Mapping method

Two different approaches to an extended magnetic solid are employed in the mapping analysis, i.e., the spin dimer and band structure approaches. In the spin dimer approach [16,17], one defines the spin dimer for each superexchange path of interest as the structural fragment containing the two interacting spin sites. Then the energies of two different electronic states of the spin dimer are determined by first principles electronic structure calculations to carry out the mapping analysis. Therefore, the spin dimer approach reduces the problem of studying an extended magnetic solid to that of a number of spin dimers representing various spin exchange paths of the solid. In the band structure approach [21], the electronic energies of a magnetic solid are determined for a number of states with different spin arrangements on the basis of electronic band structure calculations.

4.1.1. Spin dimer approach

The ground and the first excited electronic states of a spin dimer can be calculated by using the CI wave function method. Then the excitation energy ΔE_e between these two electronic states is set equal to the excitation energy ΔE_s between the ground and the first excited spin states determined by the Heisenberg spin Hamiltonian $-J\hat{S}_1 \cdot \hat{S}_2$. Thus from Eq. (2.7), the spin exchange parameter for the spin dimer is expressed as [35]

$$J = \begin{cases} -\dfrac{\Delta E_e}{1 + \dfrac{1}{2}(M-N)} & \text{(for } J<0\text{),} \\[4ex] \dfrac{\Delta E_e}{N + \dfrac{1}{2}(M-N)} & \text{(for } J>0\text{).} \end{cases} \qquad (4.1)$$

However, if the HS and BS electronic states of a spin dimer are determined by using the DFT method, the energy difference, $E_e(\text{BS}) - E_e(\text{HS})$, between these two electronic states is equated to that between the HS and BS spin states determined by the Ising spin Hamiltonian $-J\hat{S}_{1z} \cdot \hat{S}_{2z}$. Thus from Eq. (2.13), the spin exchange parameter for the spin dimer is expressed as [23,35]

$$J = \frac{2[E_e(\text{BS}) - E_e(\text{HS})]}{MN}. \qquad (4.2)$$

In DFT the total energy of an electronic state can be expanded in Taylor series with respect to the electron occupation numbers. The transition state (TS) of a spin dimer (Fig. 1c) can be defined as the state in which each of the $2N$ magnetic orbitals (α- and β-spin) of the spin site 2 has half an electron and the M unpaired electrons

of the spin site 1 are accommodated in the α-spin magnetic orbitals. Then, the energy difference between the HS and BS electronic states is expressed as [23]

$$E_e(\text{BS}) - E_e(\text{HS})$$
$$= \sum_{j=1}^{N} (\varepsilon_j^\beta - \varepsilon_j^\alpha)\Big|_{n_i^\alpha = 1/2,\ n_i^\beta = 1/2 \ (\text{all } i=1-N)}, \qquad (4.3)$$

where ε_j^γ ($\gamma = \alpha, \beta$) is the jth magnetic orbital (spin γ) energy of the TS. Thus, from Eqs. (2.12) and (2.13), the spin exchange parameter J is related to the orbital energy differences of the TS as follows [23].

$$J = \frac{2}{MN} \sum_{j=1}^{N} (\varepsilon_j^\beta - \varepsilon_j^\alpha)\Big|_{n_i^\alpha = 1/2,\ n_i^\beta = 1/2 \ (\text{all } i=1-N)}. \qquad (4.4)$$

4.1.2. Band structure approach

As discussed in Section 2.2.1, the energies of various ordered spin states of a magnetic solid can be readily expressed in terms of the spin exchange parameters when the Ising Hamiltonian, Eq. (2.15), is employed. Thus if the energies of the corresponding electronic states are calculated by performing electronic band structure calculations on the basis of either DFT or unrestricted Hartree–Fock theory [21], then the values of the spin exchange parameters can be determined by mapping analysis. Let us denote the electronic energies corresponding to the spin state energies $E_s(1\text{HS})$ and $E_s(1\text{BS})$ of the 1D uniform chain (Fig. 3) as $E_e(1\text{HS})$ and $E_e(1\text{BS})$, respectively. Likewise, we denote the electronic energies corresponding to the spin state energies $E_s(2\text{HS})$, $E_s(2\text{BS}_1)$ and $E_s(2\text{BS}_2)$ of the 1D alternating chain (Fig. 4) as $E_e(2\text{HS})$, $E_e(2\text{BS}_1)$ and $E_e(2\text{BS}_2)$, respectively. Then, from Eq. (2.19) the J value of the 1D uniform magnetic chain is calculated as

$$J = 2[E_e(1\text{BS}) - E_e(1\text{HS})]. \qquad (4.5)$$

From Eq. (2.22) the J_1 and J_2 values of the 1D alternating magnetic chain are calculated as

$$J_1 = 4[E_e(2\text{BS}_2) - E_e(2\text{HS})], \qquad (4.6a)$$

$$J_2 = 4[E_e(2\text{BS}_1) - E_e(2\text{BS}_2)]. \qquad (4.6b)$$

4.2. Direct method

In the direct method [48–51], the spin exchange parameters of an extended magnetic solid are calculated from its ground state electronic structure determined by DFT electronic band structure calculations. In the muffin-tin potential approximation [52], wave functions in each atomic sphere are expanded in terms of localized orthonormal basis $|inlm\sigma\rangle$ (i denotes the atom site, n the principal quantum number, l the orbital quantum number, m the magnetic quantum number, and σ the spin index). Within the linear muffin-tin orbital (LMTO)

method [52], Liechtenstein et al. [48] showed that spin exchange parameters of a magnetic solid are second derivatives of the ground-state electronic energy with respect to the magnetic-moment rotation. In terms of LMTO calculations using the LDA + U functional [53], the spin exchange parameters of several extended magnetic solid are determined quantitatively by the direct method [49–51]. In this approach the spin exchange parameter J_{ij} between two magnetic ions i and j of a magnetic solid is given by [49–51]

$$J_{ij} = \sum_{\{m\}} I^i_{mm'} \chi^{ij}_{mm'm''m'''} I^j_{m''m'''}, \tag{4.7}$$

where $\chi^{ij}_{mm'm''m'''}$ is the intersite susceptibility calculated in terms of the band orbitals and energies. The spin-dependent potential $I^i_{mm'}$ for the ith atom in the unit cell is expressed as

$$I^i_{mm'} = V^{i\uparrow}_{mm'} - V^{i\downarrow}_{mm'} \tag{4.8}$$

in terms of the LDA + U potential $V^{i\sigma}_{mm'}$ ($\sigma = \uparrow, \downarrow$) at the spin site i. This direct method has led to quantitative descriptions of spin exchange interactions for several extended magnetic solids [49–51]. Nevertheless, it is noted that the LDA + U potential $V^{i\sigma}_{mm'}$ contains two empirical parameters, i.e., the screened Coulomb potential U and exchange potential J. For d electrons these parameters are related to the Slater integrals [54] F^k as $U = F^0$ and $J = (F^2 + F^4)/14$. Namely, the values of J_{ij} calculated by using Eq. (4.7) depend on these empirical parameters.

5. Qualitative description of spin exchange interactions

This section is concerned with the question of how to discuss trends in spin exchange interactions of magnetic solids on a qualitative level. In essence, electron localization is responsible for spin exchange interactions of magnetic solids. Thus we first consider the electronic structure of a dimer with one electron and one orbital per site to discuss how electron localization comes about. Then we examine its implications and discuss qualitative aspects of spin exchange interactions of general spin dimers.

5.1. Electron localization and spin exchange interaction

Consider that a spin dimer has two equivalent spin sites with one electron and one orbital per site (Fig. 7a). The interaction between the two site orbitals leads to two molecular levels ψ_1 and ψ_2 with energies e_1 and e_2, respectively. The molecular orbitals ψ_1 and ψ_2 represent bonding and antibonding levels, respectively. Three electron configurations of interest for this spin dimer are the triplet configuration Φ_T and the singlet config-
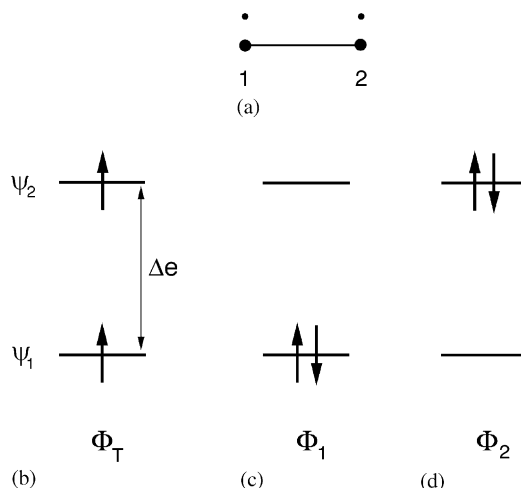
Fig. 7. Three electronic configurations of a dimer with one electron and one orbital per site: (a) Schematic representation of a dimer. (b) Triplet state $(\psi_1)^1(\psi_2)^1$. (c) Singlet configuration $(\psi_1)^2$. (d) Singlet configuration $(\psi_2)^2$.

urations Φ_1 and Φ_2 (Fig. 7b–d). When there occurs a strong chemical bonding between the two sites, the orbital energy difference $\Delta e = e_2 - e_1$ becomes large, and the CI between Φ_1 and Φ_2 is negligible so that the ground singlet state Φ_S of the spin dimer is well approximated by Φ_1. In this case of large Δe, the singlet state Φ_S is more stable than the triplet state Φ_T, and the two electrons are regarded as delocalized [55].

The orbital energy difference Δe between the levels ψ_1 and ψ_2 is small, when chemical bonding interaction between the spin sites is weak so that the two electrons of the dimer are considered as localized. In this case, the two singlet configurations Φ_1 and Φ_2 become close in energy, so the CI between Φ_1 and Φ_2 becomes strong and the ground singlet state Φ_S is described by the linear combination [8,56]

$$\Phi_s = C_1\Phi_1 - C_2\Phi_2, \tag{5.1}$$

where the mixing coefficients C_1 and C_2 have the same sign and are similar in magnitude (e.g., $C_1 = C_2 = 1/\sqrt{2}$ if $\Delta e = 0$). Using this CI wave function for the singlet state, Hay et al. [8] analyzed the energy difference between the triplet and singlet electronic states, $\Delta E_e = E_T - E_S$, under the assumptions that the orbitals ψ_1 and ψ_2 are determined from a self-consistent-field (SCF) calculation for the triplet state, and that these orbitals are linear combinations of two orthogonal orbitals χ_1 and χ_2 located at the spin sites 1 and 2, respectively.

$$\psi_1 = \frac{1}{\sqrt{2}}(\chi_1 + \chi_2), \quad \psi_2 = \frac{1}{\sqrt{2}}(\chi_1 - \chi_2),$$

$$\langle \chi_1 | \chi_2 \rangle = 0. \tag{5.2}$$

Their analysis showed that the energy difference ΔE_e is expressed as

$$\Delta E_e = E_T - E_s = -2K_{12} + \frac{(\Delta e)^2}{U_{11} - J_{12}}, \tag{5.3}$$

where K_{12} is the exchange repulsion integral, and U_{11} and J_{12} are the Coulomb repulsion integrals, associated with the site orbitals χ_1 and χ_2.

$$K_{12} = \langle 12|12 \rangle, \quad U_{11} = \langle 11|11 \rangle, \quad J_{12} = \langle 12|12 \rangle. \tag{5.4}$$

According to Eq. (4.1), the exchange parameter J of the Heisenberg Hamiltonian $\hat{H} = -J\hat{S}_1 \cdot \hat{S}_2$ is equal to

$$J = -\Delta E_e = 2K_{12} - \frac{(\Delta e)^2}{U_{11} - J_{12}}. \tag{5.5}$$

The spin exchange parameter J consists of two terms of opposite signs, so that it is convenient to write J as

$$J = J_F + J_{AF}, \tag{5.6}$$

where the ferromagnetic term J_F (>0) and the antiferromagnetic term J_{AF} (<0) are

$$J_F = 2K_{12}, \tag{5.6b}$$

$$J_{AF} = \frac{(\Delta e)^2}{U_{11} - J_{12}}. \tag{5.6c}$$

Eq. (5.6) provides a basis for discussing spin exchange interactions in terms of chemical concepts such as symmetry and overlap [8,9,34]. In general, the exchange integral K_{12} is very small so that the spin exchange cannot be ferromagnetic (i.e., $J > 0$) unless the antiferromagnetic term J_{AF} either vanishes or is very small in magnitude by symmetry. For various spin exchange paths of a magnetic solid and for a series of closely related magnetic solids, the $(U_{11} - J_{12})$ term of J_{AF} is nearly constant and can be considered as the effective on-site repulsion U_{eff}. Thus, Eq. (5.6c) is rewritten as

$$J_{AF} \approx \frac{(\Delta e)^2}{U_{eff}} \tag{5.6d}$$

and the variation of the J_{AF} values is mainly governed by that of the $(\Delta e)^2$ values. In the tight-binding approximation, the orbital energy difference Δe is related to the hopping integral t between the spin sites as

$$\Delta e = 2t \tag{5.7}$$

so that

$$J_{AF} \approx \frac{4t^2}{U_{eff}}. \tag{5.6e}$$

If each spin site is represented by non-orthogonal orbitals ϕ_1 and ϕ_2 (instead of the orthogonal orbitals χ_1 and χ_2), then the hopping integral is proportional to the overlap integral S between them [56, Chapter 2]

$$t \propto S = \langle \phi_1|\phi_2 \rangle. \tag{5.8}$$

Consequently,

$$J_{AF} \propto -(\Delta e)^2 \propto -S^2. \tag{5.9}$$

For an antiferromagnetic exchange interaction (i.e., $J < 0$), the J_{AF} term dominates over the J_F term because the latter is very small. Therefore, trends in antiferromagnetic exchange interactions can be discussed on the basis of the trends in the corresponding J_{AF} values [26]. The latter can be estimated by calculating the associated Δe or t values (Section 6). More general cases of spin exchange interactions will be discussed in Section 5.4.

5.2. Electron correlation and orbital occupancy

It is important to consider the effect of electron correlation (i.e., electron–electron repulsion leading to electron localization) on electronic configurations from the viewpoint of one-electron orbital theory. We first examine the delocalized- and localized-electron states of a spin dimer discussed in the previous section, and then consider the corresponding states of a 1D chain.

In the case of large Δe, the ground singlet state Φ_S is well approximated by the configuration Φ_1, in which the orbital ψ_1 is doubly occupied (Fig. 7c). This occupancy is energetically favorable in terms of filling the lower-lying bonding level, but unfavorable because the double occupancy gives rise to on-site repulsion $U_{11} = \langle 11|11 \rangle$. The triplet configuration Φ_T, in which the orbitals ψ_1 and ψ_2 are each singly occupied (Fig. 7b), avoids the on-site repulsion at the expense of occupying the bonding and antibonding levels equally. The singlet state Φ_1 is more stable than the triplet state Φ_T if $2\Delta e > U_{11}$. The reverse is true if $2\Delta e < U_{11}$ [55]. The singlet configuration Φ_1 can be used to refer to the electron-delocalized state.

In the case of small Δe, the ground singlet state Φ_S represented by the CI wave function, Eq. (5.1). Although the configurations Φ_1 and Φ_2 each consist of doubly occupied orbitals, their weights in Φ_S are nearly the same when $\Delta e \approx 0$ so that the occupancy of the orbitals ψ_1 and ψ_2 orbital is essentially close to unity. In essence, this situation is similar to that of the triplet state Φ_T in which the orbitals ψ_1 and ψ_2 are each singly occupied. In this sense, the electron configuration Φ_T can be used to refer to the electron-localized state, regardless of whether the ground state is triplet or singlet [55].

It is important to recognize the solid-state counterpart of the above observations. Consider a 1D chain with one electron and one orbital per site (Fig. 8a). If electron correlation is neglected, the levels of the bottom half of the band are each doubly filled, thereby leading to a metallic state (Fig. 8b). Non-spin-polarized electronic band structure calculations predict that a system with a half-filled band is always metallic, which is obviously incorrect. By analogy with the spin dimer example

(a)

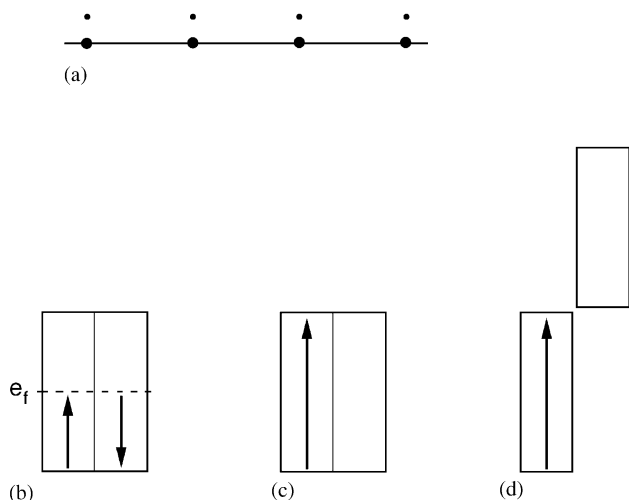(b)   (c)   (d)

Fig. 8. Metallic and magnetic insulating states of a 1D chain with one electron and one orbital per site: (a) Schematic representation of a 1D chain. (b) Metallic state. (c) Magnetic insulating state in non-spin-polarized representation. (d) Magnetic insulating state in spin-polarized representation.

(a)

(b)   (c)

Fig. 9. Orbital occupations of the electron-delocalized and electron-localized states of a dimer consisting with one electron and one orbital per site, where the two sites are equivalent: (a) Orbital interaction between the two sites leading to the bonding and antibonding levels of the dimer. (b) Orbital occupation of the electron-delocalized state. (c) Orbital occupation of the electron-localized state.

(a)   (b)
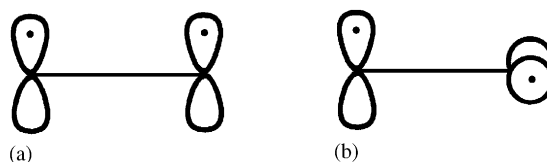
Fig. 10. Arrangements of two singly filled p-orbitals of a dimer: (a) Parallel arrangement. (b) Perpendicular arrangement.

discussed above, a magnetic insulating state can be represented by a band filling in which all the band levels are each singly filled with up-spin electrons (Fig. 8c) [55]. (From the viewpoint of spin-polarized representation, the latter is equivalent to filling all the up-spin band levels singly filled while leaving all the down-spin band levels unoccupied. In spin-polarized electronic band structure calculations for this formally ferromagnetic insulating state, the up-spin and down-spin bands become split in energy, Fig. 8d.) The metallic and magnetic insulating states are similar in that they possess a partially filled band, but they differ in the way the band levels are occupied. Given the bandwidth of the 1D chain as W, the metallic state is more stable than the magnetic insulating state if $W > U_{11}$, while the reverse is true if $W < U_{11}$ [55,57]. The bandwidth W is equal to $2\Delta e$. Therefore, the delocalized- and localized-electron states of a dimer are similar in nature to the metallic and magnetic insulating states of a solid, respectively [55].

5.3. Electron correlation and orbital ordering

Electron correlation has an important effect on the arrangement of singly filled orbitals between adjacent spin sites (i.e., orbital ordering) [49,58–60]. Suppose that the sites 1 and 2 of a spin dimer (Fig. 7a) are represented by the non-orthogonal orbitals ϕ_1 and ϕ_2, respectively. If the two sites are equivalent, the energies of the orbitals ϕ_1 and ϕ_2 are the same (i.e., e_1^0). The interaction between the two orbitals give rise to the bonding level e_1 and the antibonding level e_2 such that the stabilization of the bonding level is smaller in magnitude than the destabilization of the antibonding level, i.e.,

$(e_2 - e_1^0) > (e_1^0 - e_1)$ (Fig. 9a) [56, Chapter 2]. As discussed in the previous section, the delocalized state (Fig. 9b) is more stable than the localized state (Fig. 9c) if $U_{11} < 2\Delta e$ whereas the reverse is true if $U_{11} > 2\Delta e$ [55]. In the delocalized state, the two-electron two-orbital interaction stabilizes the system by $\Delta E = (2e_1 - 2e_1^0) \propto -S$, which is enhanced by increasing the overlap [56, Chapter 2]. For the localized state, the two-electron two-orbital interaction destabilizes the system by $\Delta E = (e_2 + e_1) - 2e_1^0 \propto S^2$, which is reduced by decreasing the overlap [56, Chapter 2]. As an example, consider the arrangements of two singly filled p orbitals. When $U_{11} < 2\Delta e$, the stabilization is maximum in the parallel arrangement (Fig. 10a) but vanishes in the orthogonal arrangement (Fig. 10b). When $U_{11} > 2\Delta e$, however, the destabilization is maximum in the parallel arrangement (Fig. 10a) and vanishes in the orthogonal arrangement (Fig. 10b). The orbital ordering phenomenon is observed in magnetic solids of transition metal elements when their magnetic ions have partially filled degenerate d-block levels [49,58–60]. This phenomenon is a manifestation of the fact that in electron-localized states (i.e., $U_{11} > 2\Delta e$) a net destabilization results from a two-electron two-orbital interaction, and this destabilization

is reduced by decreasing the overlap between the two orbitals (see Section 7.4) [60].

5.4. Analysis of spin exchange interactions

5.4.1. Spin dimer approach

As discussed in Section 5.1, the magnitude of J_{AF} for a spin dimer can be estimated in terms of the spin orbital interaction energy Δe when the two spin sites are equivalent (Fig. 11a). If the two spin sites of a spin dimer are not equivalent, the extent of the spin exchange interaction is estimated by calculating the net spin orbital interaction energy $[(\Delta e)^2 - (\Delta e^0)^2]^{1/2}$ [26,61] or $(\Delta e - \Delta e^0)$ where Δe^0 is the energy difference between the two non-equivalent magnetic orbitals (Fig. 11b). The Δe^0 value can be estimated from the energies of the magnetic orbitals calculated for the spin monomers (i.e., the structural units containing one spin site) representing the two spin sites. Obviously, $\Delta e^0 = 0$, when the two spin sites are equivalent. For simplicity of our notation, we will use the symbol $\Delta\varepsilon$ to represent Δe for the case of two equivalent spin sites, and $[(\Delta e)^2 - (\Delta e^0)^2]^{1/2}$ for the case of two non-equivalent spin sites.

In principle, the J_{AF} term can be described in terms of the hopping integral t rather than the spin–orbital interaction energy $\Delta\varepsilon$. For a spin dimer representing an SSE interaction (through an $M-L\cdots L-M$ spin exchange path), the hopping integral t can be determined by performing fragment molecular orbital analysis [56, Chapter 3, 62]. Such a spin dimer is made up of two separate spin monomers with no shared atom between them. Thus the magnetic orbitals for the two spin sites can be defined by performing tight-binding electronic structure calculations for the corresponding spin monomers, and the hopping integral t is determined as the interaction energy integral between the two magnetic orbitals. For a spin dimer representing an SE interaction (through an $M-L-M$ spin exchange path), the two spin monomers of the spin dimer share an atom or more. Thus, the shared atoms have to be used in defining the magnetic orbitals of both spin sites by
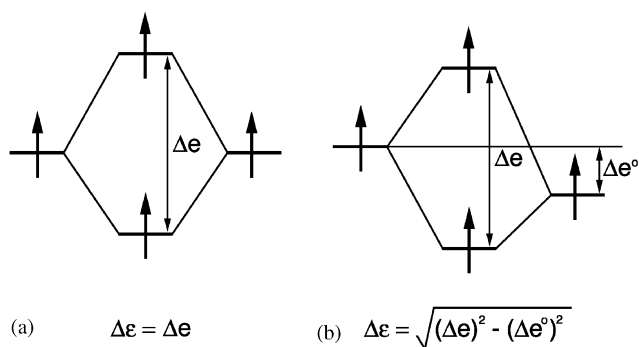
electronic structure calculations. Consequently, the hopping integral t for SE interactions cannot be determined by fragment molecular orbital analysis even with tight-binding electronic structure calculations. This is why SE interactions are discussed in terms of the spin orbital interaction energies $\Delta\varepsilon$ calculated for spin dimers, and the corresponding hopping integrals t are then estimated as $\Delta\varepsilon/2$.

When two adjacent spin sites have M and N unpaired spins, respectively, the overall spin exchange parameter J is then described by [63]

$$J = \frac{1}{MN} \sum_{\mu=1}^{M} \sum_{v=1}^{N} J_{\mu v}. \tag{5.10}$$

Therefore, the trends in spin exchange parameters can be discussed in terms of the sum of the spin–orbital interaction energy squares [64–66],

$$\langle(\Delta\varepsilon)^2\rangle = \frac{1}{MN} \sum_{\mu=1}^{M} \sum_{v=1}^{N} (\Delta\varepsilon_{\mu v})^2. \tag{5.11a}$$

From the viewpoint of non-orthogonal magnetic orbitals, the antiferromagnetic contribution of each term $\Delta\varepsilon_{\mu v}$ is zero when the magnetic orbitals ϕ_μ and ϕ_v are different in symmetry so that $S_{\mu v} = 0$, and is negligible when ϕ_μ and ϕ_v are different in shape so that $S_{\mu v}$ is negligibly small. Therefore, only the "diagonal" terms $\Delta\varepsilon_{\mu\mu}$ can contribute significantly in Eq. (5.11a) [64–66]. This point is discussed further below by considering spin dimers consisting of transition metal ions located at octahedral sites [67]. It should be noted that for SSE interactions the $\langle(\Delta\varepsilon)^2\rangle$ value can be evaluated as follows

$$\langle(\Delta\varepsilon)^2\rangle = \frac{1}{MN} \sum_{\mu=1}^{M} \sum_{v=1}^{N} 4(t_{\mu v})^2 \tag{5.11b}$$

by calculating the $t_{\mu v}$ values on the basis of fragment molecular orbital analysis. Here the $t_{\mu v}$ has the meaning of the hopping integral between the magnetic orbitals ϕ_μ and ϕ_v.

When the two spin sites have high-spin d^5 ions (i.e., $M = N = 5$), the d-electron configuration of each spin site is $(t_{2g})^3(e_g)^2$ (Fig. 12a). Thus each spin site has three magnetic orbitals (ϕ_1, ϕ_2, ϕ_3) from the t_{2g}-block levels and two magnetic orbitals (ϕ_4, ϕ_5) from the e_g-block levels. In terms of these magnetic orbitals, the $(t_{2g})^3(e_g)^2$ configuration is expressed as $(\phi_1)^1(\phi_2)^1(\phi_3)^1(\phi_4)^1(\phi_5)^1$. Then the $\langle(\Delta\varepsilon)^2\rangle$ value for the interaction between two adjacent high-spin d^5 ions is approximated by

$$\langle(\Delta\varepsilon)^2\rangle \approx \frac{1}{5\times 5} \sum_{\mu=1}^{5} (\Delta\varepsilon_{\mu\mu})^2. \tag{5.12}$$

To examine the spin exchange interactions between spin sites containing different numbers of unpaired spins ($M \neq N$), it is convenient to define the following energy
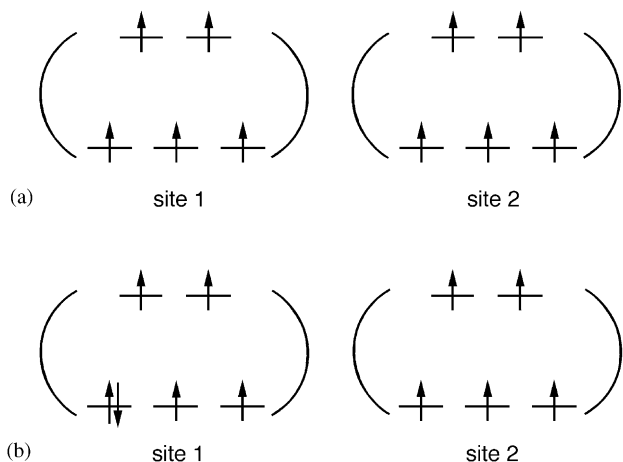

(a) $\Delta\varepsilon = \Delta e$ (b) $\Delta\varepsilon = \sqrt{(\Delta e)^2 - (\Delta e^\circ)^2}$

Fig. 11. Spin orbital interactions energies $\Delta\varepsilon$. (a) Spin dimer with two equivalent spin sites. (b) Spin dimer with two non-equivalent spin sites.

Fig. 12. Spin dimers composed of magnetic metal ions at octahedral sites. (a) Two spin sites have high-spin d^5 ions (i.e., $M = N = 5$). (b) One spin site has a high-spin d^6 ion ($M = 4$), and the other site a high-spin d^5 ion ($N = 5$).

terms

$$(\Delta\varepsilon_{t2g})^2 = (\Delta\varepsilon_{11})^2 + (\Delta\varepsilon_{22})^2 + (\Delta\varepsilon_{33})^2,$$
$$(\Delta\varepsilon_{eg})^2 = (\Delta\varepsilon_{44})^2 + (\Delta\varepsilon_{55})^2. \tag{5.13}$$

As an example, consider the interaction of a high-spin d^6 ($S = 2$) ion with a high-spin d^5 ($S = 5/2$) ion (Fig. 12b). A high-spin d^6 ($S = 2$) ion is described by the configuration $(t_{2g})^4(e_g)^2$. From the viewpoint of the magnetic orbitals ϕ_μ ($\mu = 1-5$), the three configurations

$$(\phi_1)^2(\phi_2)^1(\phi_3)^1(\phi_4)^1(\phi_5)^1,$$

$$(\phi_1)^1(\phi_2)^2(\phi_3)^1(\phi_4)^1(\phi_5)^1,$$

$$(\phi_1)^1(\phi_2)^1(\phi_3)^2(\phi_4)^1(\phi_5)^1$$

should contribute equally to $(t_{2g})^4(e_g)^2$. The spin exchange between the high-spin d^6 ($S = 2$) and high-spin d^5 ($S = 5/2$) ions results only from interactions between singly filled orbitals. Consequently, the $\langle(\Delta\varepsilon)^2\rangle$ value for the spin exchange interaction can be approximated by

$$\langle(\Delta\varepsilon)^2\rangle \approx \frac{1}{4 \times 5}\left[\frac{2}{3}(\Delta\varepsilon_{t2g})^2 + (\Delta\varepsilon_{eg})^2\right]. \tag{5.14}$$

To generalize this analysis, we assume that one spin site has m_t and m_e unpaired spins in the t_{2g}- and e_g-block levels, respectively ($M = m_t + m_e$), while the other spin site has n_t and n_e unpaired spins in the t_{2g}- and e_g-block levels, respectively ($N = n_t + n_e$). Then it is straightforward to show that the $\langle(\Delta\varepsilon)^2\rangle$ value can be approximated by

$$\langle(\Delta\varepsilon)^2\rangle \approx \frac{1}{MN}\left[\frac{m_t}{3} \times \frac{n_t}{3}(\Delta\varepsilon_{t2g})^2 + \frac{m_e}{2} \times \frac{n_e}{2}(\Delta\varepsilon_{eg})^2\right]. \tag{5.15}$$

The analysis given above can be extended in a similar manner to other cases of magnetic transition metal ions [66].

From the spin orbital interaction energy $\Delta\varepsilon_{\mu\mu}$ calculated for a spin dimer, the corresponding hopping integral can be estimated as $t_{\mu\mu} = \Delta\varepsilon_{\mu\mu}/2$. Thus, each antiferromagnetic component of the $J_{\mu\mu}$ term $J_{\mu\mu,AF}$, is related to $\Delta\varepsilon_{\mu\mu}$ and $t_{\mu\mu}$ as follows

$$J_{\mu\mu,\text{AF}} \approx -\frac{(\Delta\varepsilon_{\mu\mu})^2}{U_{\text{eff}}} = -\frac{4(t_{\mu\mu})^2}{U_{\text{eff}}}. \tag{5.16}$$

Since the effective on-site repulsion is nearly constant for a given system, the antiferromagnetic component of the overall spin exchange parameter J of the spin dimer can be written as [66]

$$J_{\text{AF}} \approx \frac{\langle(\Delta\varepsilon)^2\rangle}{U_{\text{eff}}}. \tag{5.17}$$

It should be noted that $\langle(\Delta\varepsilon)^2\rangle$ reduces to $(\Delta\varepsilon)^2$ when $M = N = 1$.

5.4.2. Band structure approach

In discussing the magnetic properties of a magnetic insulator on the basis of first principles DFT electronic band structure calculations, it is common to calculate the electronic band structure for its normal metallic state and then extract information necessary for describing the magnetic properties from the partially filled bands of the metallic state [68]. The dispersion relations of the partial bands can be simulated with those of tight-binding bands that result from a set of hopping integrals t. Using a set of the hopping integrals t that provides the best fitting, one can discuss the J_{AF} values in terms of $-4t^2/U_{\text{eff}}$, where the effective on-site repulsion U_{eff} value is treated as an empirical parameter.

The ground electronic structure of a magnetic solid is not metallic, so it is conceptually unsatisfactory to deduce information about the magnetic insulating state using the electronic band structure of the metallic state. In the first principles DFT approach, a spin-ordered magnetic insulating state is described by spin-polarized electronic structure calculations. In such calculations, the dispersion relations of the up-spin bands are not exactly the same as those of the down-spin bands. Therefore, the use of the up- and down-spin bands in the fitting analysis will lead to two different sets of hopping integrals. In contrast, the electronic band structure of the normal metallic state provides one set of hopping integrals because the up- and down-spin bands have identical dispersion relations. Thus, though conceptually inelegant, it is convenient and expedient to use the electronic band structure of the metallic state in deducing information about the spin exchange parameters of a magnetic insulator. Even in this case, it should be pointed out that the hopping integrals t derived from the band structure approach are fitting

parameters, so their magnitudes depend on the set of hopping integrals used for the fitting. In addition, these t values do not provide direct information concerning how their magnitudes are governed by the local structural and electronic factors of the spin sites.

6. Extended Hückel tight binding method

Despite its highly semi-empirical nature, the EHTB method [29] has been indispensable over the past three decades and half in unraveling structure–property relationships in all kinds of materials, from molecules to solids, from organic to inorganic compounds [56,69]. In recent years, the EHTB method has also been found indispensable in understanding the trends in spin exchange interactions of various magnetic solids (see Section 7). Since this method does not include any electron correlation, one might question the validity of using this method in describing spin exchange interactions of magnetic solids, which are after all a manifestation of strong electron correlation. As discussed in Section 5.2, however, the essential consequence of electron correlation for a magnetic system is that its ground electronic state is described by an electron-localized configuration with an appropriate number of singly occupied levels. Therefore, use of EHTB calculations for magnetic solids becomes appropriate as long as one employs proper electron-localized configurations.

For strongly correlated systems, even the state-of-the-art DFT electronic structure calculations often fail to produce correct electron-localized states. Currently, this problem is fixed by using the LDA + U potential [53], which introduces empirical parameters into first-principles electronic structure calculations (Section 4.2). From the viewpoint of the ideal of first principles electronic structure theory, the LDA + U method is not elegant. Nevertheless, given a task to explain experimental observations, it is preferable to have correct explanations using an inelegant theory rather than incorrect explanations using an elegant theory. The validity of EHTB calculations should be viewed in this spirit. In understanding the relationships between crystal structures and physical properties of solid state materials, it is necessary to calculate their electronic structures (Fig. 13). What level of calculations to employ depends on what kinds of answers we seek from calculations. The EHTB method can be invaluable if one asks the kinds of qualitative questions that it can answer (for a recent review see Ref. [69]).

6.1. Basis of the EHTB method

In the EHTB method the molecular or crystal orbitals ψ_i ($i = 1, 2, \ldots, m$) of a system are expressed as linear combinations of its valence atomic orbitals $\chi_1, \chi_2, \chi_3, \ldots$
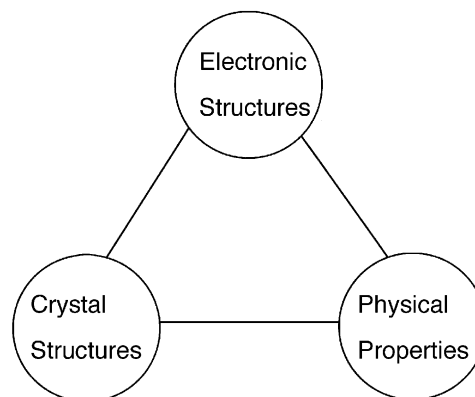
Fig. 13. Three elements of structure–property correlation studies.

and χ_m.

$$\psi_i = \sum_{\mu=1}^{m} C_{\mu i} \chi_\mu. \tag{5.18}$$

The valence atomic orbitals are approximated by Slater type orbitals (STOs). A single-zeta (SZ) STO, χ_μ, is defined by

$$\chi_\mu \propto r^{n-1} \exp(-\zeta r) Y(\theta, \phi), \tag{5.19a}$$

where n is the principal quantum number, ζ is the exponent, and $Y(\theta, \phi)$ is the spherical harmonics. In a double-zeta (DZ) STO, a linear combination of two exponential functions is used

$$\chi_\mu \propto r^{n-1} [c_1 \exp(-\zeta_1 r) + c_2 \exp(-\zeta_2 r)] Y(\theta, \phi). \tag{5.19b}$$

The orbital ψ_i is the eigenfunction of the effective one-electron Hamiltonian, H^{eff},

$$H^{\mathrm{eff}} \psi_i = e_i \psi_i. \tag{5.20}$$

In the EHTB method the explicit form of H^{eff} is not specified, but its matrix representation, $H_{\mu v} = \langle \chi_\mu | H^{\mathrm{eff}} | \chi_v \rangle$, in atomic orbital basis is defined semi-empirically. Namely, the diagonal element $H_{\mu\mu}$ is approximated by the valence state ionization potential (VSIP) of the atomic orbital χ_μ [70,71]

$$H_{\mu\mu} = -\mathrm{VSIP} \tag{5.21a}$$

and the off-diagonal elements $H_{\mu v}$ is approximated by the Wolfsberg–Helmholz formula [70],

$$H_{\mu v} = \frac{1}{2} K S_{\mu v} (H_{\mu\mu} + H_{vv}), \tag{5.21b}$$

where $S_{\mu v}$ is the overlap integral $S_{\mu v} = \langle \chi_\mu | \chi_v \rangle$ and $K = 1.75$. In the weighted Wolfsberg–Helmholz approximation [72], the coefficient K is replaced with another coefficient K', which is given by

$$K' = K + \varDelta^2 + \varDelta^4 (1 - K), \tag{5.22}$$

where $\varDelta = (H_{\mu\mu} - H_{vv})/(H_{\mu\mu} + H_{vv})$. The weighted Wolfsberg–Helmholz approximation is used to reduce the extent of counter-intuitive orbital mixing [72,73].

The energies e_i, and the atomic orbital coefficients $C_{\mu i}$ of the orbitals ψ_i are obtained by solving the set of simultaneous equations,

$$\sum_{\mu=1}^{m} (H_{\mu i} - e_i S_{\mu i}) C_{\mu i} = 0 \quad (i = 1, 2, \ldots, m). \quad (5.23)$$

The semi-empirical parameters of EHTB calculations are the ζ values for single-zeta STOs, the ζ_1, ζ_2, c_1 and c_2 values for double-zeta STOs, and the VSIP values of the valence atomic orbitals. These values can be taken from results of atomic electronic structure calculations using the Hartree–Fock method [74,75].

6.2. Strengths and weaknesses of the EHTB method

The approximations of the EHTB method leading to Eq. (5.23) are very crude, so it has serious drawbacks that first principles electronic structure theories do not have. For example, EHTB calculations cannot be used to predict either the optimum structure of a system or the relative energies of a system with different electron configurations. For systems of known geometry, however, EHTB calculations provide valuable information about their electronic properties. In EHTB calculations the total energy of a system is given by the sum of its occupied orbital energies. Thus, for a molecule with two electrons to fill its HOMO and LUMO, EHTB calculations predict that the closed-shell singlet state is always more stable than the triplet state in disagreement with experiment. When EHTB calculations give a small HOMO–LUMO gap for a molecule, one should expect that the ground state of the molecule might be a triplet state. Similarly, EHTB calculations predict that a solid with a partially filled band is always metallic in conflict with experiment. If EHTB calculations give a narrow partially filled band for a solid, one should expect that the solid might be a magnetic insulator rather than a metal.

The fact that EHTB calculations do not depend on the number of electrons in a system leads to advantages that no first principles theory can ever match:

(1) EHTB calculations are simple and hence enable the study of molecular and extended solids too large to study using first principles electronic structure calculations. The simplicity of the EHTB method does not necessarily mean that the electronic structures it generates are unreliable.
(2) The electronic structure of a complex system can be approximated by that of its appropriate fragment. For example, in an organic conducting salt (BEDT-TTF)$_2$X with mononegative anion X^-, layers of the (BEDT-TTF)$_2^+$ cations alternate with layers of the X^- anions. The cation layers are primarily responsible for the transport and magnetic properties of the salt, and are well separated from each other.

Therefore, the electronic structure of a (BEDT-TTF)$_2$X salt is well approximated by that of an isolated cation layer [76]. In EHTB calculations, this approximation is valid and simplifies the task of calculations enormously.

(3) The local electronic structure of a transition metal ion M surrounded with n main group ligand atoms L in its first coordination sphere is well approximated by the d-block electronic structure calculated for the complex ML_n. For the purpose of electron counting for the d-block levels, each ligand is treated as a closed shell anion. For example, the magnetic solid CaV_4O_9 (see Section 7.6) is made up of edge- and corner-sharing VO_5 square pyramids, and the vanadium and oxygen atoms of CaV_4O_9 have the oxidation states $+4$ and -2, respectively. Consequently, a spin monomer unit is represented by $(VO_5)^{6-}$, an edge-sharing spin dimer by $(V_2O_8)^{8-}$, a corner-sharing spin dimer by $(V_2O_9)^{10-}$. The highly charged anion state of these species does not present a computational problem in EHTB calculations, because the latter do not depend on the number of electrons a system has, unlike the case of first principles calculations. To carry out first-principles electronic structure calculations for a highly charged anion species, it is necessary to embed the anion in an appropriate matrix of positive point charges to create a realistic potential for each atom of the anion species [77]. A desirable outcome is not necessarily guaranteed from such first-principles calculations because SCF iterations may cause oscillations between two different states rather than converging to one state and because the state reached by SCF convergence may not be a physically meaningful one.

For the reasons presented above, EHTB calculations have been extensively used to study qualitative structure–property relationships in a variety of molecules and solids [56,69]. When results of EHTB calculations for molecules or solids of known structure are not consistent with their physical properties, it is necessary to examine several possible sources leading to this disagreement before resorting to first principles electronic structure calculations:

(1) The failure stems from the assumptions inherent in all electronic structure theories. As discussed in Sections 5.1 and 5.2, one needs to consider that the low-spin is not necessarily more stable than the high-spin states in a molecule, and that the metallic state is not necessarily more stable than the magnetic insulating states in a solid.
(2) The failure originates from the use of EHTB approximations. In this case, it is important to analyze the source of the failure from the viewpoint

of the atomic parameters employed (e.g., the VSIP values and the exponents of the STOs), modify the parameters appropriately, and repeat calculations. In spirit, this process is similar to what one does with first-principles calculations. For example, when a chosen basis set or correlation level does not give correct results, one tries another basis set or correlation level.

(3) Results of EHTB calculations for a system depend sensitively on the geometry used for calculations. Since EHTB calculations cannot be used for geometry optimization, it is critical to question if the geometry employed is reliable. This is particularly true for studies of spin exchange interactions [26].

(4) It is possible that experimental results under examination are incorrect. This is particularly true for electron transport and magnetic properties of solids that are easily affected by unsuspected impurities in samples.

6.3. Parameters of EHTB calculations

In general, results of EHTB calculations depend more sensitively on the exponents of STOs than on their VSIPs. For metallic compounds consisting of transition metal elements M and main group elements L, it was customary to use DZ-STOs for the d-orbitals of M and SZ-STOs for the s/p-orbitals of L [78]. However, use of DZ-STOs for both in EHTB calculations leads to a better agreement with experiment and first principles electronic structure calculations [79,80]. For conducting salts of organic donor molecules as well, use of DZ-STOs provides a better description of the overlap between adjacent molecules and hence a better description of their electronic structures [76,81]. In reproducing trends in spin exchange interactions of magnetic solids of transition metal elements, use of DZ-STOs for the d-orbitals of M and DZ-STOs for the s/p-orbitals of L is essential [26,82].

In a DZ-STO, Eq. (5.19b), the exponents ζ_1 and ζ_2 describe contracted and diffuse STOs, respectively (i.e., $\zeta_1 > \zeta_2$). The diffuse STO provides an orbital tail that enhances overlap between L atoms in the short $L \cdots L$ contacts of the $M-L \cdots L-M$ super-superexchange paths as well as that between M and L in the $M-L-M$ superexchange paths [26,82]. The spin–orbital interaction energy $\Delta\varepsilon$ values are affected most sensitively by the exponent ζ_2 of the diffuse p-orbital of L. The ζ_2 values taken from results of atomic electronic structure calculations [74,75] can be too diffuse. In this case, they can be increased as $(1+x)\zeta_2$, where one should determine the optimum x value by studying spin exchange interactions of a reference compound as a function of x [82]. For example, for the oxygen $2p$

orbital the x-value appropriate for spin exchange interactions of some magnetic oxides is found to be in the range of 0.10–0.13 [82]. Hereafter the oxygen $2p$ orbital for $x = 0$ will be referred to as the uncalibrated orbital, that for $x = 0.10 - 0.13$ as the calibrated orbital.

6.4. Comparison with the DFT method

In the CI wave function method, the Hartree–Fock equations solve the exact Hamiltonian (i.e., the molecular Hamiltonian) with approximate many-body wave functions (i.e., Slater determinants), and the exact solution can be achieved through systematic improvements in the form of many-body wave functions such as CI wave functions [83]. In this approach, atomic orbitals and hence molecular orbitals are used as basis functions to improve the form of many-body wave functions, so that orbital concepts as practiced by chemists disappear.

In contrast, approximations in DFT are introduced only in the exchange-correlation operator. The density functional equations solve an approximate many-body Hamiltonian with exact wave functions, and DFT approaches the exact solution by improving the exchange-correlation operator [83]. Therefore, orbital concepts as practiced by chemists remain valid in DFT. From the perspective of the EHTB method, first principles DFT electronic structure calculations are akin to doing EHTB calculations in which the parameters of calculations (i.e., the orbital exponents and VSIP values) are adjusted self-consistently as a function of electron density distribution. Results of DFT electronic structure calculations can be readily interpreted by employing the concepts of orbital interactions on the basis of EHTB calculations [84–86].

7. Spin dimer analysis of the spin exchange interactions and magnetic structures of extended magnetic solids

Over the past several years our studies [26] on numerous magnetic solids have shown that the relative strengths of SE and SSE interactions can be estimated almost semiquantitatively using spin dimer analyses based on EHTB calculations. In this section we survey the spin exchange interactions and magnetic structures of various magnetic solids studied by this method. When available, spin exchange parameters deduced from experiment and calculated from first principles electronic structure computations will be compared with the corresponding $\langle (\Delta\varepsilon)^2 \rangle$ values obtained by EHTB calculations. In this section, the s, p_x, p_y, p_z, d_{xy}, d_{xz}, d_{yz}, $d_{3z^2-r^2}$ and $d_{x^2-y^2}$ atomic orbitals will be referred as s, x, y, z, xy, xz, yz, $3z^2 - r^2$ and $x^2 - y^2$ orbitals, respectively.

7.1. Comparison between first principles and EHTB calculations

It is important to see how the $\langle(\Delta\varepsilon)^2\rangle$ values scale with the experimental spin exchange parameters J and the calculated J values obtained from first principles electronic structure computations. We examine this question by considering the two classes of magnetic solids whose experimental J values were examined by both first principles and EHTB electronic structure calculations.

The magnetic properties of three-dimensional (3D) perovskites $KNiF_3$ and $KCuF_3$ as well as the layered perovskites K_2NiF_4, K_2CuF_4 and La_2CuO_4 were exten-sively studied both theoretically [87–91] and experimen-tally [92–101]. These compounds are made up of corner-sharing ML_6 octahedra. The ML_6 octahedra of $KNiF_3$ are regular in shape [101], while those of K_2NiF_4 [102], K_2CuF_4 [103], La_2CuO_4 [104] and $KCuF_3$ [105] are distorted. The oxidation state of the transition metal atoms is $+2$ in these compounds. Thus each Cu^{2+} (d^9) ion has one unpaired spin, and each Ni^{2+} (d^8) ion two unpaired spins. As summarized in Table 4 and Fig. 14a, the experimental J values of these compounds are almost quantitatively reproduced by the calculated J values from first principles electronic structure computations [87–91]. Table 4 and Fig. 14b also show that the experimental J values and the calculated $\langle(\Delta\varepsilon)^2\rangle$ values have a good linear relationship.

The magnetic solids A_2MnF_5 ($A=$ Rb, Cs, NH_4, Na, Li) [106–110] contain MnF_5 chains made up of trans-corner sharing MnF_6 octahedra, and their high-spin Mn^{3+} (d^4) cations each have four unpaired spins. Each MnF_6
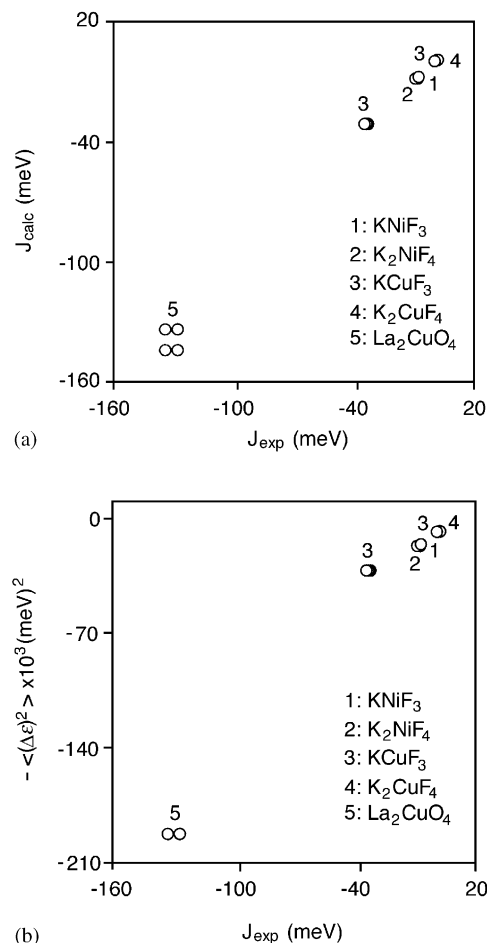
Fig. 14. Comparison of the experimental spin exchange parameters J_{exp} of perovskite magnetic solids with the calculated values J_{calc} obtained from first-principles electronic structure computations and the $\langle(\Delta\varepsilon)^2\rangle$ values obtained from EHTB calculations: (a) J_{exp} vs. J_{calc}. (b) J_{exp} vs. $\langle(\Delta\varepsilon)^2\rangle$.

octahedron has a Jahn–Teller distortion such that the two axial Mn–F bonds along the z-axis become longer than the four equatorial Mn–F bonds. Thus in the d-block levels of a distorted MnF_6 octahedron, the $x^2 - y^2$ level (contained in the equatorial plane) is empty while the remaining four d-levels are each singly filled, so that $M = N = 4$ for the spin dimers. Table 5 lists the intrachain J values of A_2MnF_5 ($A=$ Rb, Cs, NH_4, Na, Li) determined experimentally [106–110], those obtained by DFT electronic structure calculations [23], and the $\langle(\Delta\varepsilon)^2\rangle$ values. The J values from the DFT calculations are greater than the experimental ones (Fig. 15a) by a factor of ~ 3. The $\langle(\Delta\varepsilon)^2\rangle$ values show a good linear relationship with the experimental J values (Fig. 15b).

As can be seen from the above two examples, the $\langle(\Delta\varepsilon)^2\rangle$ values obtained from EHTB calculations scale linearly with the experimental spin exchange parameters J, and with the calculated J values from first principles electronic structure computations. This provides a

Table 4
Comparison of the experimental spin exchange parameters J_{exp} with the calculated J_{calc} values from first-principles computations and the $\langle(\Delta\varepsilon)^2\rangle$ values from EHTB calculations

Compound	J_{exp} (meV)	J_{calc} (meV)	$-\langle(\Delta\varepsilon)^2\rangle$ $(meV)^2$
K_2CuF_4	1.5[a], 1.9[b]	1.21[j]	−140
$KCuF_3$	−33[c], −34[d], −35[e]	−31.3[j]	−25,900
	0.34[e]	0.56[k]	−400
K_2NiF_4	−8.2[f], −9.5[f]	−8.10[j]	−9700
$KNiF_3$	−7.7[g]	−7.41[j]	−8600
La_2CuO_4	−128[h], −134[i]	−144.7[j]	−102,000

[a] Yamada [97].
[b] Hirakawa and Ikeda [98].
[c] Katoda [94].
[d] Hutchings et al. [95].
[e] Satija et al. [96].
[f] de Jong and Miedema [93].
[g] Lines [92].
[h] Singh et al. [99].
[i] Aeppli [100].
[j] Moreiro et al. [90].
[k] Moreiro and Illas [87].

Table 5
Comparison of the experimental spin exchange parameters J_{exp} of A_2MnF_5 ($A =$ Rb, Cs, NH_4, Na, Li) with the calculated J_{calc} values from DFT first-principles computations and the $\langle(\Delta\varepsilon)^2\rangle$ values from EHTB calculations

Compound	J_{exp} (K/k_B)	J_{calc} (K/k_B)	$-\langle(\Delta\varepsilon)^2\rangle$ (meV)^2
Rb_2MnF_5	−22.6[a]	−73[f]	−2280
Cs_2MnF_5	−19.4[a]	−63[f]	−1960
$(NH_4)_2MnF_5$	−11.2[b], −10.6[c], −10.45[d]	−43[f]	−500
Na_2MnF_5	−9.2[e], −8.6[d], −8.25[b]	−26[f]	−130
Li_2MnF_5	−6.3[b], −5.6[e]	−24[f]	−190

[a] Núñez and Roisnel [106].
[b] Sears and Hoard [107].
[c] Hirakawa and Ikeda [98].
[d] Emori et al. [110].
[e] Massa [109].
[f] Dai and Whangbo [23].

(a)

(b)
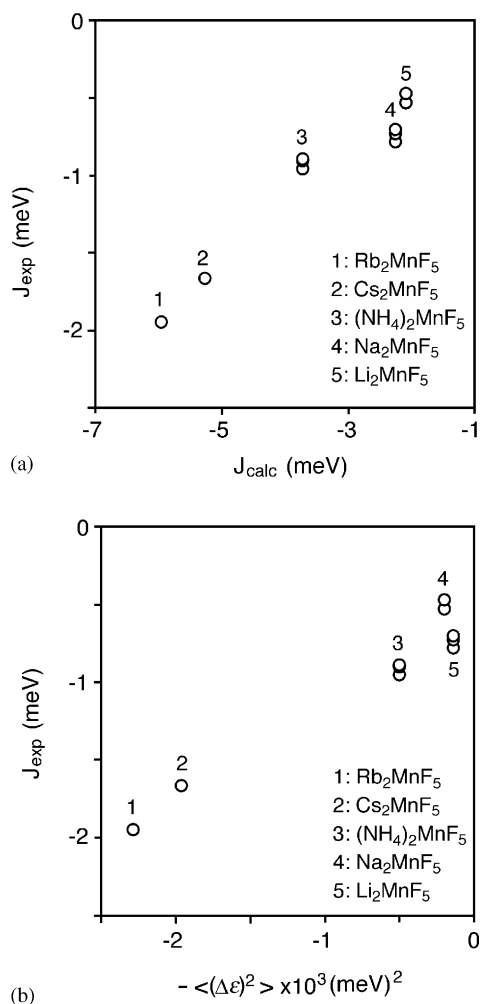
Fig. 15. Comparison of the experimental spin exchange parameters J_{exp} of A_2MnF_5 ($A =$ Rb, Cs, NH_4, Na, Li) with the calculated values J_{calc} obtained from first-principles electronic structure computations and the $\langle(\Delta\varepsilon)^2\rangle$ values obtained from EHTB calculations: (a) J_{exp} vs. J_{calc}. (b) J_{exp} vs. $\langle(\Delta\varepsilon)^2\rangle$.

justification for the use of $\langle(\Delta\varepsilon)^2\rangle$ values obtained from EHTB calculations in estimating the relative strengths of spin exchange interactions in magnetic solids. Additional examples of a good linear relationship between the $\langle(\Delta\varepsilon)^2\rangle$ and the experimental J values and that between the $\langle(\Delta\varepsilon)^2\rangle$ and the calculated J values are discussed in Sections 7.6 and 7.7.

7.2. Importance of bond length consideration

In predicting whether a given $M-L-M$ superexchange interaction is ferromagnetic or antiferromagnetic without any electronic structure calculations, Goodenough rules [24] are employed. Given the symmetry properties of the metal d-orbitals containing unpaired spins and the number of unpaired spins at the metal site M, these rules predict the sign of an $M-L-M$ superexchange (i.e., minus for antiferromagnetic and plus for ferromagnetic) on the basis of the $\angle M-L-M$ bond angle. An implicit assumption introduced in these rules is that there is no strong variation of the $M-L$ bond lengths in the $M-L-M$ superexchange paths to compare. When this assumption is not valid, it is critical to take into consideration how the $M-L$ bond length affects the strength of the $M-L-M$ superexchange. We illustrate this point by considering the magnetic structure of marokite $CaMn_2O_4$ [111].

$CaMn_2O_4$ consists of corner- and edge-sharing MnO_6 octahedra containing high-spin Mn^{3+} (d^4) ions. All the Mn^{3+} ions are equivalent in $CaMn_2O_4$, but the Jahn–Teller distortion of each MnO_6 octahedron makes all its six Mn–O bonds different [111] (e.g., 1.897, 1.910, 1.923, 1.958, 2.361 and 2.449 Å). Thus every Mn^{3+} ion has six different superexchange interactions with its neighboring Mn^{3+} ions. In these superexchange paths both the $\angle$ Mn–O–Mn bond angles and the Mn–O bond lengths vary widely. A perspective framework view of the Mn_2O_4 lattice is shown in Fig. 16, where the Mn sites labeled A through G specify the six different superexchange interactions that a given Mn^{3+} site can have, i.e., $(A-B)$, $(A-C)$, $(A-D)$, $(A-E)$, $(A-F)$ and $(A-G)$. Table 6 summarizes the geometrical parameters associated with these Mn–O–Mn superexchange paths [111]. It is noted that the Mn–O–Mn bridges are symmetric in the paths $(A-B)$ and $(A-C)$, slightly asymmetric in the path $(A-E)$, and highly asymmetric in the paths $(A-D)$, $(A-F)$ and $(A-G)$. In addition, in the symmetric and nearly symmetric superexchange paths, the Mn–O bond lengths increase in the order, $(A-C) < (A-E) < (A-B)$. Table 6 also lists the signs of the six superexchange interactions determined from the powder neutron diffraction study [111], and the signs of these interactions assigned on the basis of Goodenough rules [24,111].

The spin monomers of $CaMn_2O_4$ are given by $(MnO_6)^{9-}$, while the spin dimers with a corner- and edge-sharing MnO_6 octahedra by $(Mn_2O_{11})^{16-}$ and $(Mn_2O_{10})^{14-}$, respectively. Table 7 summarizes the $\langle (\Delta\varepsilon)^2 \rangle$ values calculated for the six superexchange paths [66]. The relative strengths of the spin exchange interactions, calculated using the largest $\langle (\Delta\varepsilon)^2 \rangle$ value as the reference, show that the strengths of the AFM interactions decrease in the order, $(A-C) > (A-E) > (A-B) \gg (A-D) > (A-G) > (A-F)$. This finding is
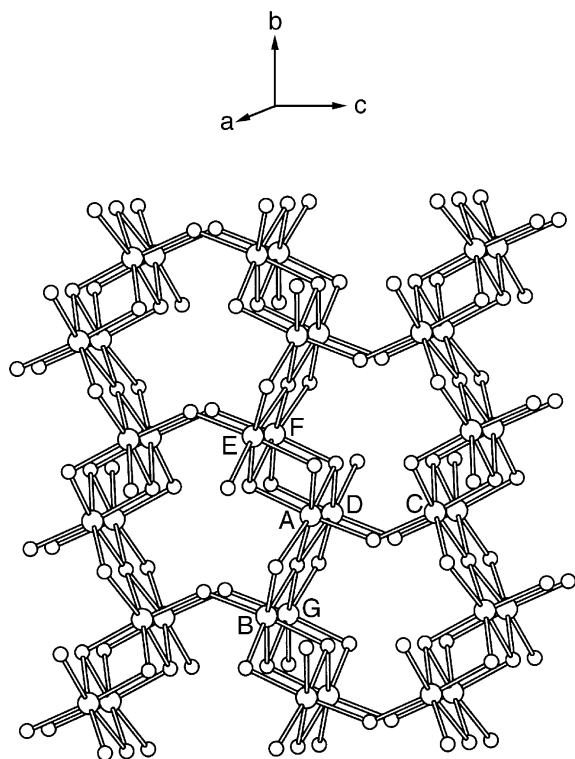
Fig. 16. Framework view of the 3D Mn_2O_4 lattice, where the large and small circles refer to Mn and O atoms, respectively. The Mn sites labeled A through G are used to specify six different superexchange interactions $(A-B)$, $(A-C)$, $(A-D)$, $(A-E)$, $(A-F)$ and $(A-G)$.

entirely consistent with the magnetic structure of $CaMn_2O_4$ determined by the neutron powder diffraction study [111].

The strongest AFM interaction occurs in the path $(A-C)$. The structure of the spin dimer representing the $(A-C)$ interaction is depicted in Fig. 17, where the four magnetic orbitals are xz, xy, yz and z^2. Note that the Mn–O–Mn bridge of this spin dimer is symmetric and is made up of the shortest Mn–O bonds. Consequently, two of the four magnetic orbitals (i.e., "xz" and "xy" orbitals) on each spin site give rise to two strong π-type orbital interactions through the Mn–O–Mn bridge (Fig. 18a and b) [78]. In each π-type orbital interaction, the $2p$ orbital of the bridging oxygen is absent in the lower level ψ_+, but contributes strongly out-of-phase to the Mn $3d$ orbitals in the upper level ψ_- because the Mn–O–Mn bridge is symmetric and because the Mn–O bonds are short (i.e., Mn–O = 1.897/1.897 Å, Table 6). Consequently, the energy split between the ψ_+ and ψ_- levels (i.e., the spin–orbital interaction energy $\Delta\varepsilon$) is large for the "xz" and "xy" magnetic orbitals. The remaining two magnetic orbitals (i.e., "yz" and "z^2" orbitals) of each spin site lead to a negligible $\Delta\varepsilon$ because the $2p$ orbital of the bridging oxygen cannot contribute to both ψ_+ and ψ_- by symmetry (Fig. 18c) and because the $2p$ orbital of the bridging oxygen contribute very

Table 7
$\langle (\Delta\varepsilon)^2 \rangle$ and relative $-J_{AF}$ values calculated for the six superexchange interactions of $CaMn_2O_4$

Interaction	$\langle (\Delta\varepsilon)^2 \rangle$[a]	Relative $-J_{AF}$[b]
$(A-B)$	1030	0.40
$(A-C)$	2540	1.00
$(A-D)$	570	0.22
$(A-E)$	1830	0.72
$(A-F)$	170	0.07
$(A-G)$	300	0.12

[a] These values, presented in units of $(meV)^2$, were calculated using the crystal structure of Ref. [111].
[b] The path $(A-C)$ was taken as the reference.

Table 6
Geometrical parameters associated with the six Mn–O–Mn superexchange paths of $CaMn_2O_4$[a,b]

Interaction	Mn–O–Mn (Å)	∠ Mn–O–Mn (deg)	Goodenough	Experiment
$(A-B)$	1.958/1.958	102.0	AFM	AFM
	2.445/2.445	76.9		
$(A-C)$	1.897/1.897	135.6	?	AFM
$(A-D)$	2.361/1.923	94.0	AFM	AFM
	1.958/2.445	90.6		
$(A-E)$	1.910/1.923	98.4	AFM	AFM
	1.923/1.910	98.4		
$(A-F)$	2.361/1.910	96.2	?	FM
	1.910/2.361	96.2		
$(A-G)$	1.958/2.445	167.5	FM	FM

[a] Taken from the crystal structure of Ref. [111].
[b] FM and AFM refer to ferromagnetic and antiferromagnetic, respectively.

weakly to both ψ_+ and ψ_- by orbital mismatch (Fig. 18d). Due to the two strong π-type orbital interactions, the spin exchange path $(A-C)$ becomes strongly antiferromagnetic.

The second strongest antiferromagnetic interaction occurs in the path $(A-E)$, where the two Mn–O–Mn bridges are only slightly asymmetric (Mn–O = 1.910/1.923 Å) and the bridging Mn–O bonds are relatively
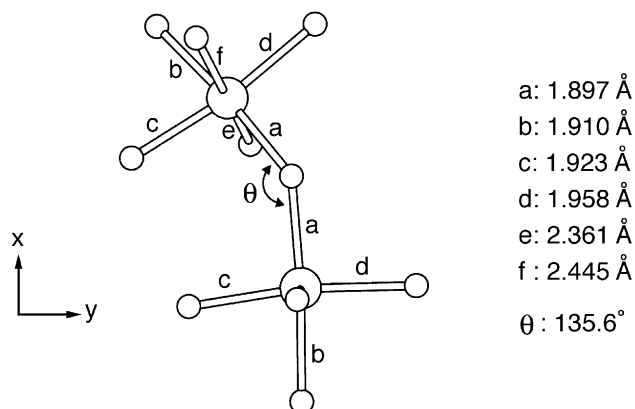

Fig. 17. Arrangements of the Mn–O bonds in the spin dimer representing the superexchange path $(A-C)$. The six Mn–O bonds of the lower-lying MnO$_6$ octahedron are aligned along the Cartesian coordinate axes as close as possible (i.e., the bonds b/a along the x-direction, the bonds c/d along the y-direction, and the bonds f/e along the z-direction).

a: 1.897 Å
b: 1.910 Å
c: 1.923 Å
d: 1.958 Å
e: 2.361 Å
f : 2.445 Å

θ : 135.6°

short. The third strongest antiferromagnetic interaction occurs in the path $(A-B)$, in which both Mn–O–Mn bridges are symmetric, and the bridging Mn–O bonds are relatively long (Mn–O = 1.958/1.958 Å) in one bridge and very long in another bridge (Mn–O = 2.445/2.445 Å). The decrease in the strength of the antiferromagnetic interaction in the order, $(A-C) > (A-E) > (A-B)$, is readily explained by considering that the extent of a π-type orbital interaction through a symmetric (or nearly symmetric) Mn–O–Mn bridge decreases with increasing the Mn–O bond length.

The fact that the paths $(A-F)$ and $(A-G)$ are FM, i.e., their antiferromagnetic interactions are very weak, can be easily understood because the Mn–O–Mn bridges are strongly asymmetric (e.g., Mn–O = 1.910/2.361 Å in the path $(A-F)$ and Mn–O = 1.958/2.445 Å in the path $(A-G)$) so that the energy split between the ψ_+ and ψ_- levels becomes very small for each magnetic orbital. The two Mn–O–Mn bridges of the path $(A-D)$ are quite asymmetric as well (i.e., Mn–O = 1.923/2.361 Å; 1.958/2.445 Å), so the extent of antiferromagnetic interaction in the path $(A-D)$ would be weak. On the basis of inspecting the asymmetry of the Mn–O–Mn bridges alone, it is impossible to predict if the antiferromagnetic interaction of the path $(A-D)$ will be as weak as those of the paths $(A-F)$ and $(A-G)$. Certainly, calculations of $\langle (\Delta\varepsilon)^2 \rangle$ allow one to estimate the relative strengths of such interactions.

Fig. 18. Pairs of the singly occupied molecular orbitals ψ_+ and ψ_- defining the spin orbital energies $\Delta\varepsilon$ in the spin dimer representing the superexchange path $(A-C)$. In (a)–(d), the symmetries of the magnetic orbitals at the spin sites were classified with respect to the d-block orbitals of the lower-lying MnO$_6$ octahedron in the spin dimer.
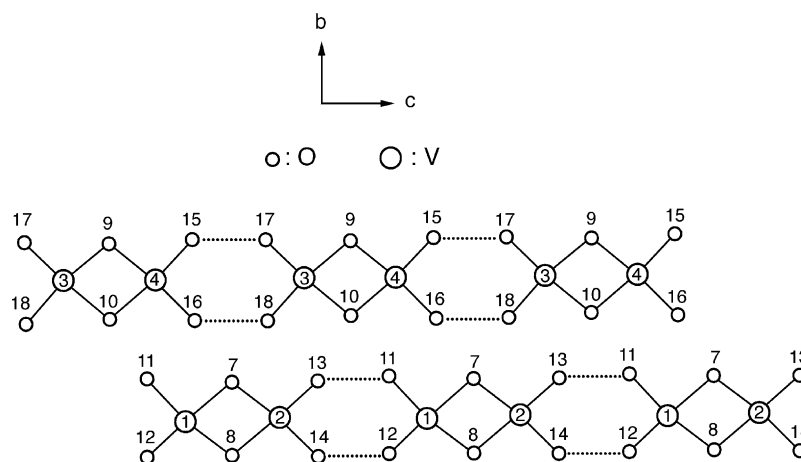
Fig. 19. Arrangements of the V and O atoms in the V1–V2 and V3–V4 ribbon-chains in the ambient pressure orthorhombic structure of $(VO)_2P_2O_7$. For simplicity, only the V and the basal oxygen atoms of the VO_5 square pyramids are shown.

7.3. Importance of super-superexchange interactions

7.3.1. Vanadyl pyrophosphate $(VO)_2P_2O_7$

The recent interest in the ambient pressure orthorhombic (APO) phase of vanadyl pyrophosphate (VPO), $(VO)_2P_2O_7$, has been in the area of its magnetic properties [25,26]. The magnetic susceptibility of VPO was found well described by the spin-1/2 alternating antiferromagnetic chain model [115], and subsequently by the spin ladder model [112,113], However, later studies showed conclusively that the spin-1/2 alternating antiferromagnetic chain model is correct for VPO [26,114,116].

The magnetic lattice of VPO is made up of VO_5 square pyramids containing V^{4+} (d^1) ions. The VO_5 square pyramids form V_2O_8 dimers by sharing one basal O–O edge. The structural feature of VPO leading to the spin-1/2 alternating antiferromagnetic chain model is the "ribbon-chains" along the crystallographic c-direction, in which adjacent V_2O_8 dimers are linked by two O–P–O bridges such that the basal planes of the dimers form ribbons. There are two non-equivalent ribbon-chains in the APO phase of VPO, as depicted in Fig. 19, where only the vanadium and the basal oxygen atoms of the VO_5 square pyramids are shown for simplicity. The perspective views along the b-direction of the V1–V2 and V3–V4 ribbon-chains are presented in Fig. 20. Along each ribbon-chain, the SE interactions, which occur through the V–O–V linkages within each V_2O_8 dimer, alternate with the SSE interactions, which occur through the V–O···O–V linkages between adjacent V_2O_8 dimers. A perspective view of how the V_2O_8 dimers repeat along the a-direction is shown in Fig. 21a, which has a ladder-like arrangement of the magnetic ions (Fig. 21b). The structural feature of the latter led to the interpretation of the magnetic property of VPO
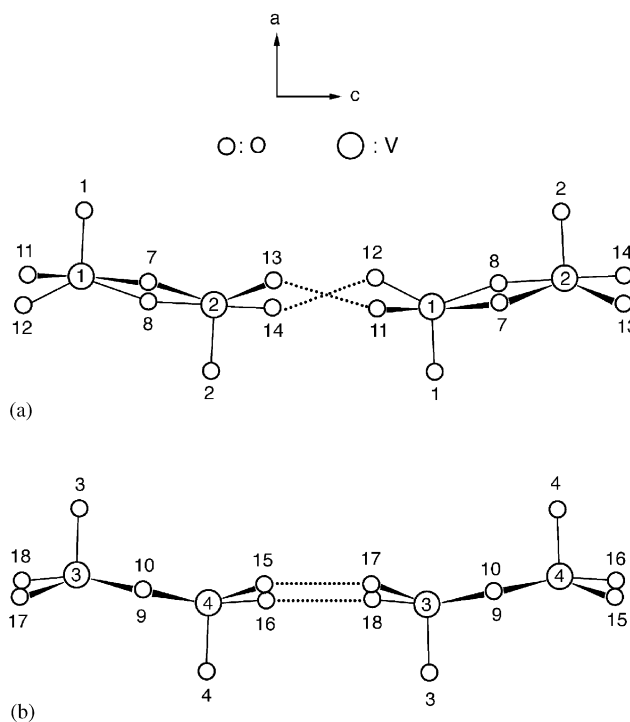
Fig. 20. Perspective views along the b-direction of the (a) V1–V2 and (b) V3–V4 ribbon-chains in the ambient pressure orthorhombic structure of $(VO)_2P_2O_7$. The O···O distances are as follows: O(11)···O(13) = 2.506 Å, O(12)···O(14) = 2.572 Å, O(15)···O(17) = q2.510 Å, O(16)···O(18) = 2.510 Å.

in terms of the ladder model [112,113], which was soon found to be incorrect for VPO [114,116].

The magnetic orbitals of the spin monomers, i.e., the $(VO_5)^{6-}$ square pyramids, are contained in the planes parallel to the basal planes (Fig. 22a). The spin dimers for SE and SSE paths are represented by $(V_2O_8)^{8-}$ and
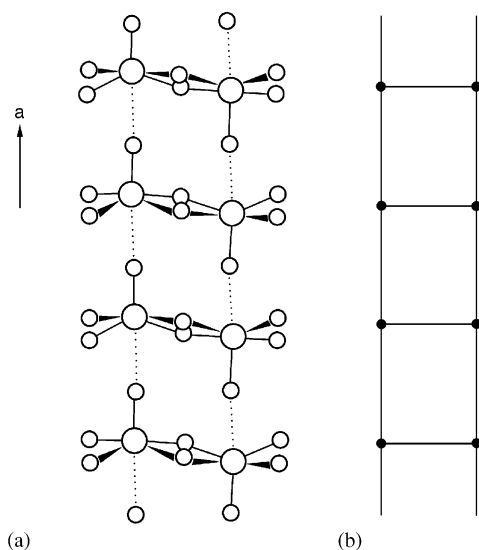
Fig. 21. (a) Perspective view of how the V_2O_8 dimers repeat along the a-direction in the ambient pressure orthorhombic structure of $(VO)_2P_2O_7$. (b) Ladder-like arrangement of the magnetic ions in (a).
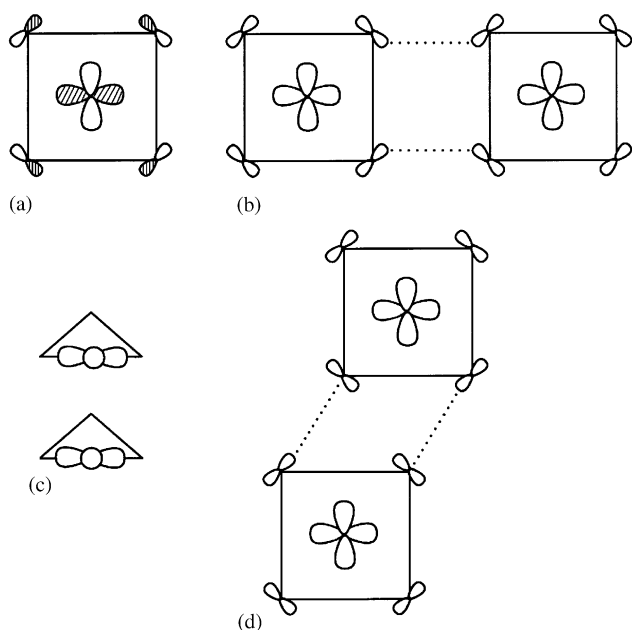
Fig. 22. (a) Magnetic orbital of a VO_5 square pyramid, in which the V $3d\ xy$ orbital is combined out-of-phase with the O $2p$ orbitals on the basal plane. (b) Overlap between two adjacent magnetic orbitals associated with an SSE interaction along a ribbon-chain. (c) δ-type overlap between the magnetic orbitals in a spin dimer along the a-direction. (d) Overlap between the magnetic orbitals associated with an SSE interaction between adjacent ribbon chains.

$(V_2O_{10})^{12-}$, respectively. Each SSE interaction along the ribbon-chain is determined by the overlap between the O $2p$ orbitals of the O$\cdots$O contacts in the two SSE paths V–O$\cdots$O–V (Fig. 22b). The O$\cdots$O distances of the V–O$\cdots$O–V paths are considerably shorter than the van der Waals distance (i.e., 2.80 Å). The magnitude of this

Table 8
Comparison of the $\Delta\varepsilon$ and J values calculated for the superexchange and super-superexchange interactions in the V3–V4 and V1–V2 ribbon chains of the ambient pressure structures of $(VO)_2P_2O_7$

Chain	Spin exchange	$\Delta\varepsilon$ (meV)	$-J/k_B$ (K)[a]	$-J/k_B$ (K)[b]
V3–V4	SSE	42	136	136
V3–V4	SE	33	84	92
V1–V2	SSE	35	94	103
V1–V2	SE	40	123	124

[a] The J values were calculated from the expression $J = -(\Delta\varepsilon)^2/U_{eff}$ with $U_{eff} = 151$ meV.
[b] The experimental values taken from Ref. [116].

interaction should increase, as the O$\cdots$O distances decrease, as the O_4 ring formed from the two O$\cdots$O contact units becomes more planar and rectangular, and as the basal planes of the two spin monomers become more parallel [26]. Along the a-direction, the two magnetic orbitals of a spin dimer have a δ-type interaction (Fig. 22c), so the associated $\Delta\varepsilon$ value is negligible. The interchain SSE interaction between magnetic orbitals is weak because along the short O$\cdots$O contact directions one oxygen p orbital lies almost in the nodal plane of the other oxygen p orbital (Fig. 22d) [117].

Only recently accurate crystal structures were determined for the APO phase of VPO [26,118], which led to accurate evaluations of the $(\Delta\varepsilon)^2$ values for the SE and SSE interactions (Table 8) [26]. The J/k_B value of the strongest antiferromagnetic interaction deduced experimentally is -136 K [114]. This J is reproduced by $J_{AF} = -(\Delta\varepsilon)^2/U_{eff}$ if the U_{eff} value is taken as 151 meV. Using this U_{eff} we calculate the J values expected for the SE and SSE interactions on the basis of the calculated $\Delta\varepsilon$ values (Table 8). These results lead to the conclusions: (1) The ribbon-chain with the larger spin gap is the V3–V4 ribbon-chain ($-J/k_B = 136$ K, 92 K), and that with the smaller spin gap is the V1–V2 ribbon-chain ($-J/k_B = 124$ K, 103 K). (2) The SSE interaction is stronger than the SE interaction in the larger spin-gap ribbon-chain, while the opposite is the case in the smaller spin-gap ribbon chain.

In understanding the relative strengths of the SE and SSE interactions of VPO, it is necessary to examine how strongly each ribbon-chain twists from the ideal ribbon structure by analyzing the O–O–O–O dihedral angles of the consecutive O_4 rings along the ribbon-chains (Table 9) [26]. In the O_4 rings associated with the SSE interactions the V3–V4 ribbon-chains are slightly twisted while the V1–V2 ribbon chains are strongly twisted. This makes the SSE interaction much stronger in the V3–V4 chain than in the V1–V2 chain. The two basal planes associated with the SE interaction are more twisted in the V3–V4 chain than in the V1–V2 chain. Thus the SE interaction is stronger in the V1–V2 chain than in the V3–V4 chain.

Table 9
O–O–O–O dihedral angles of the consecutive O_4 rings along the ribbon chains of the ambient pressure orthorhombic phase of $(VO)_2P_2O_7$

Chain	Dihedral angles (deg)
V3–V4[a]	(−7.7) (−6.8) **(−1.1)** (7.7) (6.8) **(1.1)**
V1–V2[b]	(4.7) (−4.8) **(27.0)** (−4.7) (4.8) **(−27.0)**

[a] The sequence of the O–O–O–O dihedral angles along the V3–V4 ribbon chain is defined as (17–18–10–9), (9–10–16–15), **(15–16–18–17)**, (17–18–10–9), (9–10–16–15), and **(15–16–18–17)**, where the numbers in the parentheses refer to the oxygen numbers of Fig. 19, and the dihedral angles associated with the super-superexchange paths are indicated by bold letters.

[b] The sequence of the O–O–O–O dihedral angles along the V1–V2 ribbon chain is defined as (11–12–8–7), (7–8–14–13), **(13–14–12–11)**, (11–12–8–7), (7–8–14–13), and **(13–14–12–11)**, where the numbers in the parentheses refer to the oxygen numbers of Fig. 19.

7.3.2. Vanadyl hydrogen phosphate $VO(HPO_4)\cdot0.5H_2O$

Vanadyl hydrogen phosphate (VHP), $VO(HPO_4)\cdot 0.5H_2O$, is a precursor to VPO. The ribbon-chain of VHP is depicted in Fig. 23a. Unlike the case of VPO, the ribbon-chains of VHP are strongly sinusoidal because the basal plane of each VO_5 square pyramid is inclined to the chain direction by $\sim 30°$ (Fig. 23b) [26]. Another difference between the ribbon-chains of VHP and VPO lies in the way the V atoms of each V_2O_8 dimer are located with respect to the basal planes; they reside on one side in VHP (Fig. 23b), but on opposite sides in VPO (Fig. 20) [26]. There are SE and SSE interactions to consider in each ribbon chain of VHP, but the magnetic susceptibility measurements [119] of VHP and the neutron scattering measurements [120] of its deuterium analogue, $VO(DPO_4)\cdot0.5D_2O$ (hereafter referred to as VDP), showed that the magnetic structures of VHP and VDP are described by the isolated dimer model. This implies that either the SE or the SSE interaction is strongly reduced. Calculations of the $\Delta\varepsilon$ values show [26] that the SE interaction should dominate over the SSE interaction in VHP, because the overlap between the two magnetic orbitals associated with the SSE interaction (Fig. 23b) is strongly reduced due to the large inclination angle. Consequently, both structural and electronic reasons show that the isolated spin dimers of VHP are formed by the SE interactions, not by the SSE interactions [26]. This conclusion disagrees with that deduced from the powder neutron scattering study [119]. It is necessary to resolve these irreconcilable by performing neutron scattering measurements on single crystal samples of VDP.

7.3.3. Structural features leading to strong super-superexchange interactions of V^{4+} and Cu^{2+} ions

As discussed in the previous section, the strength of a SSE interaction between V^{4+} ion sites surrounded with the main group ligands L depends critically on
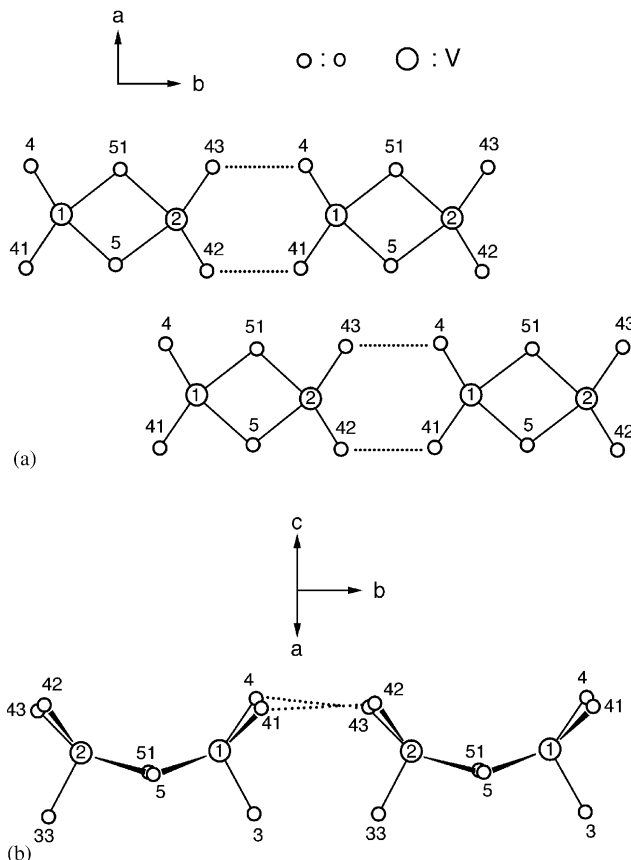
Fig. 23. (a) Arrangements of the V and O atoms in the ribbon-chains of $VO(HPO_4)\cdot0.5H_2O$. (b) Perspective view of the ribbon-chains of $VO(HPO_4)\cdot0.5H_2O$.

the overlap between their magnetic orbitals [26]. The magnetic orbital of a V^{4+} (d^1) ion is given by the xy orbital of V, which makes π-antibonding interactions with the p orbitals of the four ligands L in the basal plane (Fig. 22a). As depicted in Fig. 22b, the strength of a SSE interaction between two such magnetic orbitals increases with increasing the overlap between the p-orbital tails of the $L\cdots L$ contacts in the two $V-L\cdots L-V$ paths. This interaction becomes stronger as the L_4 ring formed from the two $L\cdots L$ contact units is more planar and rectangular, as the basal planes of the two spin monomers are more coplanar, and as the $L\cdots L$ contacts are shorter and lie within the van der Waals distance. When the latter conditions are met, a SSE interaction can be stronger than a SE interaction as found for VPO.

A similar situation is also found for spin exchange interactions involving Cu^{2+} (d^9) ions [27,28]. The magnetic orbital of a Cu^{2+} (d^9) ion is the $x^2 - y^2$ orbital of Cu, which makes sigma antibonding interactions with the p orbitals of the four ligands L (Fig. 24a). As depicted in Fig. 24b, the strength of a SSE interaction between two such magnetic orbitals increases with increasing the overlap between the two p orbital
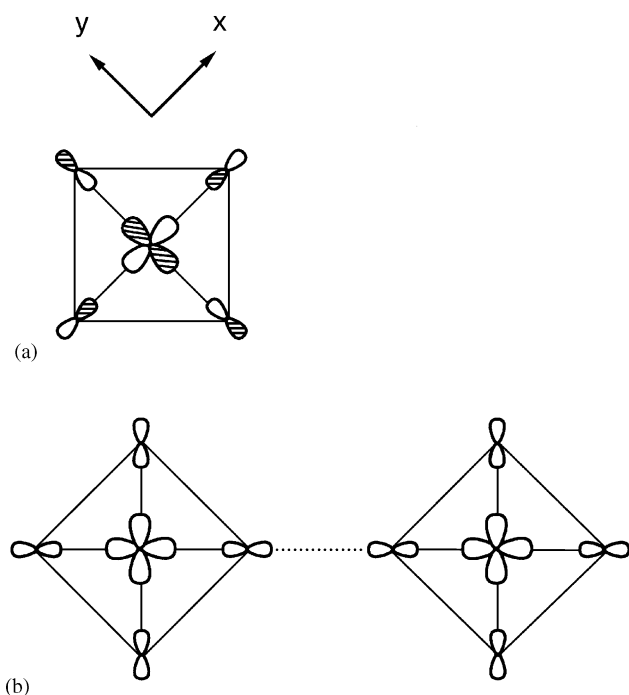
Fig. 24. (a) Magnetic orbital of a square planar CuL_4 unit containing a Cu^{2+} ion. (b) Arrangement of two magnetic orbitals in a SSE interaction having a linear $Cu-L\cdots L-Cu$ path.

tails of the $L\cdots L$ contact in one $Cu-L\cdots L-Cu$ path. This interaction becomes stronger as both $\angle Cu-L\cdots L$ bond angles become larger and as the $L\cdots L$ distance becomes shorter and lies within the van der Waals distance. The magnetic oxides $CuWO_4$ and $CuMoO_4$-III have various SE and SSE interaction paths involving Cu^{2+} ions [121,122], the strongest spin exchange interactions of which are the SSE interactions involving the most linear $Cu-O\cdots O-Cu$ paths [27]. The $O\cdots O$ distances of these paths are in the range of 2.4 Å, which is considerably shorter than the van der Waals distance, and the two $\angle Cu-O\cdots O$ angles of these paths are identical and are close to $165°$.

For the cases of V^{4+} and Cu^{2+} ions described above, a SSE interaction can be stronger than any SE interaction. Assigning strongly interacting spin exchange paths of magnetic solids should be based on appropriate electronic structure considerations. At least, one should not neglect SSE interactions that possess the structural features leading to strong SSE interactions. When a magnetic solid consists of other magnetic ions with more than one unpaired spin, it becomes more difficult to assess the relative strengths of SSE interactions without appropriate electronic structure calculations. An example of this case is discussed in the next section.

7.3.4. Strongly interacting spin units of $Cu_2Te_2O_5X_2$ ($X=Cl$, Br)

The magnetic compounds $Cu_2Te_2O_5X_2$ ($X=Cl$, Br) consist of layers of tetrahedral clusters $Cu_4O_8X_4$ [123].

Each $Cu_4O_8X_4$ cluster is made up of four "square planar" CuO_3X units, which are joined by oxygen-corner-sharing such that the four Cu^{2+} ions form a tetrahedron and are linked by four SE paths $Cu-O-Cu$ (Fig. 25a). The $Cu_4O_8X_4$ clusters form layers parallel to the ab-plane (Fig. 25b), in which the four $Cu-X$ bonds of each cluster are pointed towards the neighboring clusters so that every four adjacent $Cu_4O_8X_4$ clusters form a X_4 tetrahedron of short $X\cdots X$ contacts. Thus within a layer of $Cu_4O_8X_4$ clusters, there occur SSE interactions between adjacent clusters through the $Cu-X\cdots X-Cu$ paths. Between adjacent layers of $Cu_4O_8X_4$ clusters (Fig. 25c), the clusters interact through short $O\cdots O$ contacts thus forming SSE interaction paths $Cu-O\cdots O-Cu$. The geometrical parameters associated with the various SE and SSE paths of $Cu_2Te_2O_5X_2$ ($X=Cl$, Br) are summarized in Table 10. Spin monomers of $Cu_2Te_2O_5X_2$ ($X=Cl$, Br) are distorted square planar units $(CuO_3X)^{5-}$. Spin dimers with a SE path $Cu-O-Cu$ are represented by $(Cu_2O_5X_2)^{8-}$, and those with a SSE path $Cu-L\cdots L-Cu$ ($L=X$, O) by $(Cu_2O_6X_2)^{10-}$.

The magnetic susceptibility data of $Cu_2Te_2O_5X_2$ ($X=Cl$, Br) were interpreted by supposing [123–125] that the strongly interacting spin units of $Cu_2Te_2O_5X_2$ are $Cu_4O_8X_4$ clusters, and the interactions between clusters are weak. The topology of the spin exchange interactions in an isolated $Cu_4O_8X_4$ cluster is given by a tetrahedron of four spin sites as depicted in Fig. 26, where the four exchange paths J_1 refer to the four SE paths $Cu-O-Cu$, and the two exchange paths J_2 to the two SSE paths $Cu-O\cdots O-Cu$. The fitting analysis of the magnetic susceptibility data using this tetrahedron model show that $J_1 \approx J_2$ for both $Cu_2Te_2O_5Cl_2$ and $Cu_2Te_2O_5Br_2$. This result is quite surprising, as pointed out by Johnson et al. [123]. The magnetic orbital of a CuO_3X square planar unit is contained in the plane so that the two magnetic orbitals associated with a J_2 path should be nearly parallel to each other (Fig. 25a) and hence their overlap should be practically zero. Therefore, the J_2 path should be very weakly antiferromagnetic, if not ferromagnetic. In addition, the $\angle Cu-O-Cu$ angles of the SE paths $Cu-O-Cu$ are much closer to $90°$ than to $180°$ (Table 10a), so that the antiferromagnetic interaction J_1 cannot be strong according to Goodenough rules [24].

The $Cu-X\cdots X-Cu$ paths along the $(a\pm b)$-direction are the most linear SSE paths (Table 10b) [28]. In the most linear $Cu-Cl\cdots Cl-Cu$ path of $Cu_2Te_2O_5Cl_2$, the $Cl\cdots Cl$ distance (3.667 Å) is close to the van der Waals distance (i.e., 3.6 Å) while both $\angle Cu-Cl\cdots Cl$ bond angles are slightly larger than $160°$ (i.e., $164.3°$). In the most linear $Cu-Br\cdots Br-Cu$ path of $Cu_2Te_2O_5Br_2$, the $Br\cdots Br$ distance (3.835 Å) is slightly shorter than the van der Waals distance (i.e., 3.9 Å) while both $\angle Cu-Br\cdots Br$ bond angles are slightly smaller than $160°$ (i.e.,
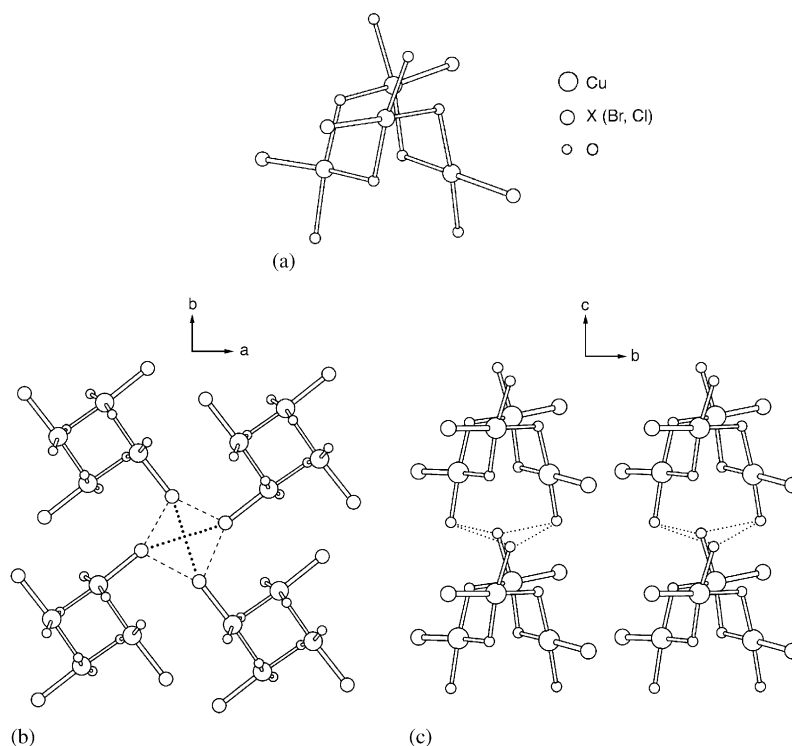
Fig. 25. (a) $Cu_4O_8X_4$ cluster of $Cu_2Te_2O_5X_2$. (b) $X\cdots X$ contacts within a layer of $Cu_4O_8X_4$ clusters parallel to the ab-plane. (c) $O\cdots O$ contacts between neighboring layers of $Cu_4O_8X_4$ clusters.

Table 10
Geometrical parameters (lengths in Å and angles in degrees) associated with the intracluster SE paths and the intercluster SSE paths in $Cu_2Te_2O_5X_2$ ($X = Cl, Br$) (a) Intracluster SE paths $Cu-O-Cu$

Cu–O–Cu	$X = Cl$	$X = Br$
Cu–O	1.971, 1.976	1.964, 2.013
$\angle$ Cu–O–Cu	109.8	106.9
Cu$\cdots$Cu	3.230	3.195

(b) Intercluster SSE paths $Cu-X\cdots X-Cu$

Cu–X$\cdots$X–Cu	$X = Cl$	$X = Br$
Along the $(a\pm b)$-direction		
Cu$\cdots$Cu	8.032	8.439
$X\cdots X$	3.667	3.835
$\angle$ Cu–X$\cdots$X	164.3, 164.3	154.4, 154.4
Along the a- and b-directions		
Cu$\cdots$Cu	6.020	6.289
$X\cdots X$	3.516	3.588
$\angle$ Cu–X$\cdots$X	125.3, 108.1	129.3, 105.5

(c) Intercluster SSE path $Cu-O\cdots O-Cu$

Cu–O$\cdots$O–Cu	$X = Cl$	$X = Br$
Cu$\cdots$Cu	5.015	5.059
O$\cdots$O	3.011	2.998
$\angle$ Cu–O$\cdots$O	83.4, 105.4	85.6, 106.5

154.4°). Consequently, the Cu–$X\cdots X$–Cu paths along the $(a\pm b)$-direction should provide very strong antiferromagnetic interactions and hence should not be neglected [28].
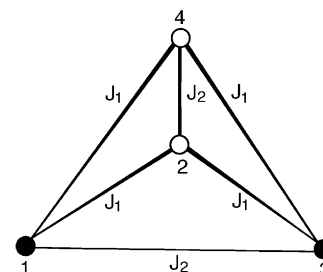
Fig. 26. Tetrahedron model based on an isolated $Cu_4O_8X_4$ cluster of $Cu_2Te_2O_5X_2$, where the circles represent Cu^{2+} ions. The unshaded circles lie above the shaded circles along the c-direction.

The $(\Delta\varepsilon)^2$ values calculated for the intra- and the intercluster spin exchange interactions (Fig. 27) of $Cu_2Te_2O_5Cl_2$ and $Cu_2Te_2O_5Br_2$ are summarized in Table 11 [28]. The $(\Delta\varepsilon)^2$ values for the Cu–O$\cdots$O–Cu paths between adjacent layers of clusters are not listed because they are negligibly small. This result is expected because the $\angle$ Cu–O$\cdots$O angles of the SSE paths Cu–O$\cdots$O–Cu between adjacent layers of tetrahedral clusters (Fig. 25c) are also much closer to 90° than to 180° (Table 10c). The intracluster SSE interaction J_2 of $Cu_2Te_2O_5X_2$ ($X=Cl$, Br) is also negligibly small for the same reason. The intracluster SE interaction J_1 is also weak as anticipated, because the $\angle$ Cu–O–Cu angles of the SE paths Cu–O–Cu are close to 90° (Table 10a).

In $Cu_2Te_2O_5X_2$ ($X=Cl$, Br) the intercluster SSE interaction J_a is by far the strongest spin exchange
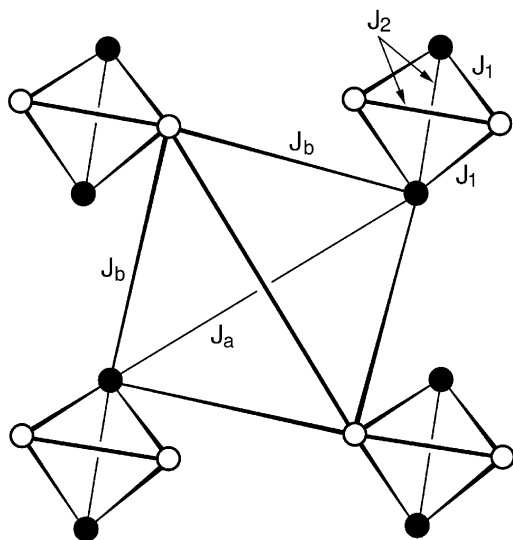
Fig. 27. Spin exchange paths in a layer of $Cu_4O_8X_4$ clusters in $Cu_2Te_2O_5X_2$, where the circles represent Cu^{2+} ions. The unshaded circles lie above the shaded circles along the c-direction. J_1 and J_2 are intracluster spin exchange interactions, and J_a and J_b are intercluster spin exchange interactions.

Table 11
$(\Delta\varepsilon)^2$ values in units of $(meV)^2$ calculated for the various SE and SSE interactions of $Cu_2Te_2O_5X_2$

Interaction	Path	Cu···Cu (Å)	$(\Delta\varepsilon)^2$	Relative strength
(a) $Cu_2Te_2O_5Cl_2$				
SE	J_1	3.230	576	0.10
	J_2	3.591	25	0.00
SSE	J_b	6.020	484	0.08
	J_a	8.032	5746	1.00
(b) $Cu_2Te_2O_5Br_2$				
SE	J_1	3.195	676	0.01
	J_2	3.543	100	0.00
SSE	J_b	6.289	12,410	0.19
	J_a	8.439	63,958	1.00

interaction. As expected, this interaction involves the most linear Cu–X···X–Cu path, which occurs along the $(a \pm b)$-direction in each layer of tetrahedral clusters. The Cu–X···X–Cu paths along the a- and b-directions are significantly less linear than those along the $(a \pm b)$-direction (Table 10b), and hence lead to weaker antiferromagnetic interactions. The $(\Delta\varepsilon)^2$ values of Table 11 suggest that the magnetic properties of $Cu_2Te_2O_5Cl_2$ and $Cu_2Te_2O_5Br_2$ should be slightly different. The relative magnitudes of the J_a, J_b, J_1 and J_2 interactions are given as follows:

$J_a > J_1 \geqslant J_b > J_2$ for $Cu_2Te_2O_5Cl_2$,

$J_a > J_b \gg J_1 > J_2$ for $Cu_2Te_2O_5Br_2$.

Thus, both $Cu_2Te_2O_5Cl_2$ and $Cu_2Te_2O_5Br_2$ are described by weakly interacting dimers. The weak inter-dimer interactions lead to isolated tetrameric units

(defined by J_a and J_b) in $Cu_2Te_2O_5Br_2$, and to a two-dimensional (2D) lattice (defined by J_a, J_1 and J_b) in $Cu_2Te_2O_5Cl_2$. It is important to note that the intracluster SE interaction is much stronger in $Cu_2Te_2O_5Cl_2$ than in $Cu_2Te_2O_5Br_2$. This reflects the fact that the Cu–O–Cu bridge is much more symmetrical in $Cu_2Te_2O_5Cl_2$ than in $Cu_2Te_2O_5Br_2$ (Table 10a) [28].

To examine the validity of a weakly interacting dimer model for $Cu_2Te_2O_5X_2$ ($X = $ Cl, Br) from the viewpoint of simulating the experimental susceptibility curve χ_{exp} of $Cu_2Te_2O_5X_2$ reported by Johnsson et al. [123] it is necessary to fit the χ_{exp} data with the calculated susceptibility curve χ_{calc} with a Weiss correction, i.e., $\chi_{exp} = \chi_{calc}/(1 - \theta\chi_{calc})$, where $\theta = 2zJ'/(Ng^2\beta^2)$ [126]. The calculated susceptibility χ_{calc} is written as $\chi_{calc} = \chi_{vv} + \chi_{TIP} + C/T$, where χ_{vv} is the Van Vleck term that depends on the spin exchange parameters, χ_{TIP} refers to the temperature-independent paramagnetism, and C/T is the term for the paramagnetic impurity. For both $Cu_2Te_2O_5Cl_2$ and $Cu_2Te_2O_5Br_2$, the experimental χ_{exp} data are very well reproduced [127] by using the models in which the relative strengths of the spin exchange parameters are determined by the spin dimer analysis [28]. The key to the success of these simulations is that the strongest antiferromagnetic spin exchange interaction is given by the intercluster spin exchange J_a. Although the tetrahedron model based solely on the intracluster interactions (Fig. 26) provides a good fitting, the two assumptions employed in this model (i.e., the neglect of the strong intercluster interaction J_a and the constraint $J_1 = J_2$) are inconsistent with electronic structure considerations as discussed above.

It is important to note that strongly interacting spin exchange paths are determined by the overlap between magnetic orbitals. For a magnetic solid of any interest, the magnetic orbital(s) are not atomic s-orbitals so that the overlap between adjacent magnetic orbitals in a magnetic solid cannot be isotropic. Consequently, the strongly interacting spin unit of a magnetic solid does not necessarily have the same geometrical feature as the arrangement of its magnetic ions [28]. It is critical to assess the strongly interacting spin exchange paths of magnetic solids on the basis of appropriate electronic structure considerations.

7.3.5. Super-superexchange interactions in $BaLn_2MnS_5$ ($Ln = La$, Ce, Pr)

When a magnetic solid consists of other magnetic ions with more than one unpaired spin, it becomes more difficult to assess the relative strengths of SSE interactions without appropriate electronic structure calculations. An example of this case is discussed in this section.

Quaternary manganese sulfides $BaLn_2MnS_5$ ($Ln = $ La, Ce, Pr) have LnS layers alternating with $BaMnS_4$ layers parallel to the ab-plane (Fig. 28) [128,129]. Each $BaMnS_4$ layer has the NaCl-type arrangement of Ba^{2+}
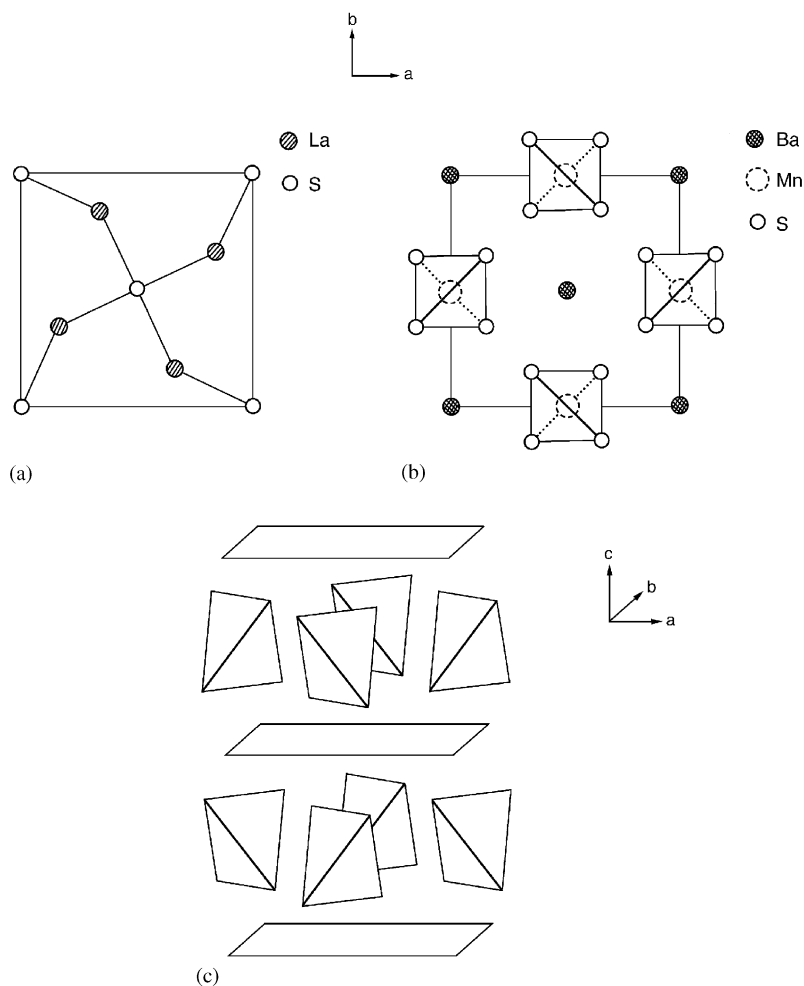
Fig. 28. (a) Arrangement of the Ln and S atoms in the LnS layer of BaLn_2MnS$_5$. (b) Arrangement of the Ba^{2+} ions and tetrahedral (MnS$_4$)$^{6-}$ anions in the BaMnS$_4$ layer of BaLn_2MnS$_5$. The (MnS$_4$)$^{6-}$ anions are elongated along the c-direction, so that the $\angle$ S–Mn–S angles pointed along the c-direction are 94.8°, 93.8° and 92.6° for $Ln =$ La, Ce and Pr, respectively. (c) Schematic view of the arrangement of the LnS and BaMnS$_4$ layers in BaLn_2MnS$_5$, where the LnS layers were represented by planes and Ba^{2+} ions of the BaMnS$_4$ layers were omitted for simplicity.

ions and tetrahedral (MnS$_4$)$^{6-}$ anions elongated along the c-direction. The shortest S$\cdots$S distances between adjacent tetrahedral (MnS$_4$)$^{6-}$ anions are slightly longer than the van der Waals distance (i.e., 3.60 Å) (Fig. 29). Thus the tetrahedral (MnS$_4$)$^{6-}$ anions are well separated from one another, and so are the Mn^{2+} (d^5) ions that are in the high-spin state ($S = 5/2$) [129]. Nevertheless, the Mn^{2+} ions of BaLn_2MnS$_5$ undergo a 3D antiferromagnetic ordering at a reasonably high temperature (i.e., the Néel temperature $T_N = 58.5$, 62.0 and 64.5 K for $Ln =$ La, Ce and Pr, respectively) [129]. Thus the Mn–S$\cdots$S–Mn super-superexchange interactions of BaLn_2MnS$_5$ are substantial not only in the ab-plane but also along the c-direction. There are three adjacent super-superexchange paths (J_1, J_2 and J_3) to consider in BaLn_2MnS$_5$ [130]. The interlayer spin exchange J_2 (between the Mn^{2+} ions along the c-direction) takes place through the intervening LnS layer (Fig. 29b). The powder neutron diffraction study of BaLa$_2$MnS$_5$ at 7 K

reveals that the antiferromagnetic transition doubles the unit cell along each crystallographic direction [130]. The $\langle (\Delta\varepsilon)^2 \rangle$ values calculated for BaLn_2MnS$_5$ are summarized in Table 12 [131]. To compare the relative strengths of these antiferromagnetic spin exchange interactions, the relative J_{AF} values were calculated using the formula $J_{AF} = -\langle (\Delta\varepsilon)^2 \rangle / U_{eff}$ with respect to the largest $\langle (\Delta\varepsilon)^2 \rangle$ value (calculated for BaPr$_2$MnS$_5$) under the assumption that U_{eff} is constant. It was found [131] that the LnS layer is not essential in determining the strength of the interlayer superexchange interaction J_2. The interlayer spin exchange J_2 is stronger than the intralayer spin exchange J_1 (by a factor of ~ 10) because the path J_2 has two short S$\cdots$S contacts whereas the path J_1 has one and because the S$\cdots$S contacts of the path J_2 are shorter than that of the path J_1 (Fig. 29). Thus the strongly interacting spin units of BaLn_2MnS$_5$ are 1D chains made up of the exchange paths J_2, and these 1D chains interact weakly via the
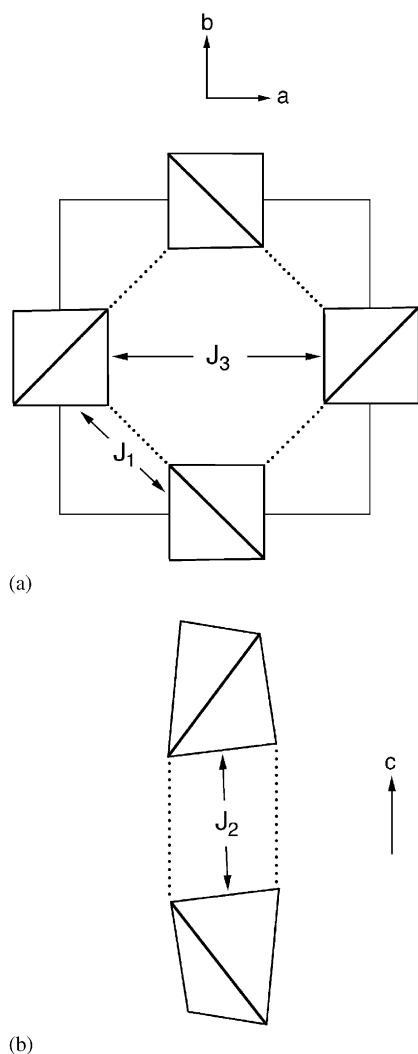
Fig. 29. Spin exchange paths of BaLn_2MnS$_5$ (a) within the BaMnS$_4$ plane and (b) along the c-direction. The dotted lines refer to the short S···S contacts. The S···S distances in (a) are 3.864, 3.869 and 3.905 Å for Ln = La, Ce and Pr, respectively, and those in (b) are 3.754, 3.737 and 3.671 Å for Ln = La, Ce and Pr, respectively.

Table 12
Values of $\langle (\Delta \varepsilon)^2 \rangle$ in (meV)^2 and relative J_{AF} values calculated for BaLn_2MnS$_5$ (Ln = La, Ce, Pr)[a]

Path	BaLa$_2$MnS$_5$		BaCe$_2$MnS$_5$		BaPr$_2$MnS$_5$	
	$\langle (\Delta \varepsilon)^2 \rangle$	Rel. J_{AF}	$\langle (\Delta \varepsilon)^2 \rangle$	Rel. J_{AF}	$\langle (\Delta \varepsilon)^2 \rangle$	Rel. J_{AF}
J_1	216	−0.083	267	−0.102	273	−0.105
J_2	2074	−0.794	2278	−0.872	2612	−1.000
J_3	44	−0.017	59	−0.023	40	−0.015

[a] The relative J_{AF} values were calculated using the expression $J_{AF} = -\langle (\Delta \varepsilon)^2 \rangle / U_{eff}$ with respect to the largest $\langle (\Delta \varepsilon)^2 \rangle$ value (calculated for BaPr$_2$MnS$_5$) under the assumption that U_{eff} is constant.

exchange paths J_1. Since the latter is not negligible compared with the former, the Néel temperatures T_N of BaLn_2MnS$_5$ are reasonably high. Table 12 shows that the strengths of J_{AF} for the J_2 path increase in the order

BaLa$_2$MnS$_5$ < BaCe$_2$MnS$_5$ < BaPr$_2$MnS$_5$, those for the J_1 path increase in the order BaLa$_2$MnS$_5$ < BaCe$_2$MnS$_5$ ≲ BaPr$_2$MnS$_5$. These results are consistent with the experimental finding that the Néel temperatures T_N increase in the order, BaLa$_2$MnS$_5$ < BaCe$_2$MnS$_5$ ≲ BaPr$_2$MnS$_5$. The J_{AF} term for the intralayer spin exchange J_3 is practically zero. This is consistent with the experimental finding that J_3 is ferromagnetic in BaLa$_2$MnS$_5$ [130].

As shown in Fig. 30, each magnetic orbital of a (MnS$_4$)$^{6-}$ anion has S $3p$ orbitals as a minor component. Such p-orbital tails of magnetic orbitals play a crucial role in determining the sign and the magnitude of a spin exchange interaction [26–28]. The strengths of the Mn–S···S–Mn SSE interactions in BaLn_2MnS$_5$ are determined by the overlap between the p-orbital tails in the S···S contacts. The non-bonding S···S contacts in the vicinity of the van der Waals distance are crucial for the SSE interactions.

7.4. Effect of orbital ordering and cooperative Jahn–Teller distortion on spin exchange interaction

7.4.1. Long-range orbital ordering and cooperative Jahn–Teller distortion

Magnetic solids of transition metal ions possessing Jahn–Teller instability exhibit a number of interesting physical phenomena such as charge ordering, orbital ordering, spin ordering and cooperative Jahn–Teller (CJTD) distortion [49,58,132–134]. When such a magnetic solid undergoes a CJTD, an orbital/spin ordering follows as a consequence. It is an interesting question whether or not a CJTD is induced by an orbital ordering that occurs prior to the distortion [49,58]. The orbital/spin ordering and CJTD phenomena have been described on the basis of phenomenological Hamiltonians [58,134,135] and first principles electronic band structure calculations [49,133]. Recently, it was shown [60] that the CJTD and orbital/spin ordering phenomena of magnetic solids can be explained in terms of orbital interactions. In the following we consider cubic perovskite KCuF$_3$ as an example.

In the ideal cubic perovskite AML$_3$ made up of corner-sharing ML$_6$ octahedra, the $M-L-M$ bridges are linear (Fig. 31a), and the A^{n+} cations ($n = 1-3$) occupy the 12-coordinate sites of the 3D ML$_3$ lattice. Fig. 31b shows a projection view of an ideal tetragonal ML$_4$ layer made up of corner-sharing ML$_6$ octahedra. The 3D ML$_3$ lattice is constructed from ML$_4$ layers by sharing their apical ligand atoms. The relative arrangement of the ML$_6$ octahedra in AML$_3$ is determined mainly by the tolerance factor $\tau = r_{A-L}/\sqrt{2} r_{M-L}$ defined by the $A-L$ and $M-L$ distances [132]. The ideal cubic structure is stable when $\tau = 1$. With a small A^{n+} cation for which $\tau < 1$, the ideal cubic structure becomes unstable because the 12-coordinate site is larger in size
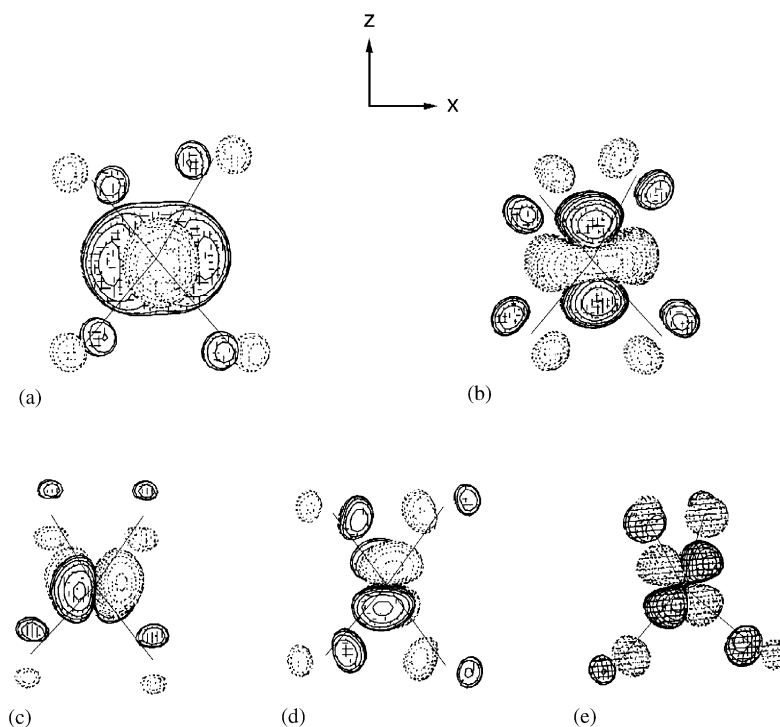
Fig. 30. 1D surface representations of the five magnetic orbitals of a tetrahedral $(MnS_4)^{6-}$ anion: (a, b) e_g orbitals. (c–e) t_{2g} orbitals.

than the A^{n+} cation. Such a perovskite reduces the size of the 12-coordinate site by cooperatively tilting the ML_6 octahedra and bending the $M-L-M$ bridges (Fig. 31c). Another important structural feature of a cubic perovskite is a distortion in the individual ML_6 octahedra, which takes place when each ML_6 octahedron has Jahn–Teller instability. For convenience, we adopt the convention that the 3D ML_3 lattice of each cubic perovskite is constructed from the ML_4 layers parallel to the ab-plane (Fig. 31b) by sharing their apical ligands along the c-direction. In the distorted structures of the cubic perovskites $KCuF_3$ [136,137], the $\angle$ Cu–F–Cu angle is 180° for all the Cu–F–Cu linkages, and there is a strong Cu–F...Cu bond alternation (i.e., 1.889 and 2.253 Å) within each CuF_4 layer while the Cu–F–Cu bridges remain symmetric along the c-direction (i.e., Cu–F = 1.962 Å). In $KCuF_3$, the CuF_4 layers that have the CJTDs shown in Fig. 32a and b alternate along the c-direction [136]. To determine how the distortions of $KCuF_3$ affect the magnetic orbitals of each CuF_6 octahedron, we define the ideal CuF_6 regular octahedron by using the average Cu–F bond length from the corresponding distorted CuF_6 octahedron. The e_g-block levels of the ideal and distorted CuF_6 octahedra are depicted in Fig. 33, where the distorted CuF_6 octahedron is oriented such that the long and short Cu–F bonds in the CuF_4 layer are pointed along the x and y axes, respectively. As expected, the distortion strongly splits the e_g levels.

In perovskites every orbital interaction between adjacent metal sites occurs via the bridging ligand atom of the associated $M-L-M$ bridge. As illustrated in Fig. 34 for a linear symmetric $M-L-M$ bridge, such an orbital interaction can be of $\sigma-$, π- or δ-type in symmetry. The spin–orbital interaction energy Δe is larger for the σ-type than for the π-type orbital interaction, and vanishes for the δ-type orbital interaction. Furthermore, the energy Δe becomes smaller as the bridging ligand atom moves away from the center of the bridge toward one metal atom (to form an asymmetric $M-L\cdots M$ bridge). It is also reduced when the $M-L-M$ bond angle decreases from 180°.

When each CuF_6 octahedron is regular in shape, the e_g-block levels "$x^2 - y^2$" and "$3z^2 - r^2$" are degenerate and accommodate three electrons so that the electronic state of each CuF_6 octahedron is described by the configurations $(3z^2 - r^2)^1 (x^2 - y^2)^2$ and $(3z^2 - r^2)^2 (x^2 - y^2)^1$. If each CuF_6 octahedron adopts the $(3z^2 - r^2)^1 (x^2 - y^2)^2$ configuration, the destabilizing interaction between doubly filled levels is strong in the ab-plane while that between singly filled levels is strong along the c-direction. If each CuF_6 octahedron adopts the $(3z^2 - r^2)^2 (x^2 - y^2)^1$ configuration, the opposite is the case. Fig. 35a and b show two examples of orbital ordering that minimize these destabilizing interactions within each CuF_4 layer parallel to the ab-plane. Between every adjacent Cu^{2+} sites, the doubly filled levels have orthogonal arrangements in each CuF_4 layer and make
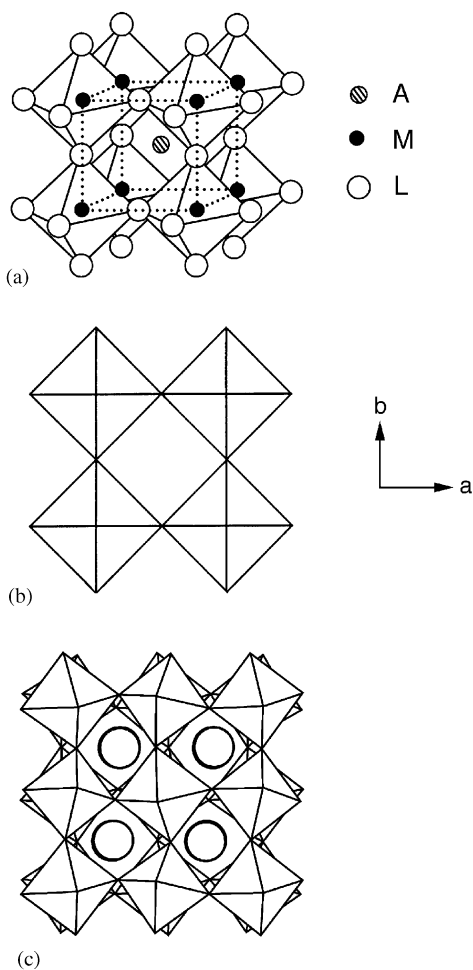
(a)

(b)

(c)

Fig. 31. (a) Perspective view of a simple cubic perovskite AML_3. (b) Projection view of an ideal tetragonal ML_4 layer parallel to the ab-plane. (c) Schematic polyhedral view of a cubic perovskite AML_3 for which $\tau < 1$.
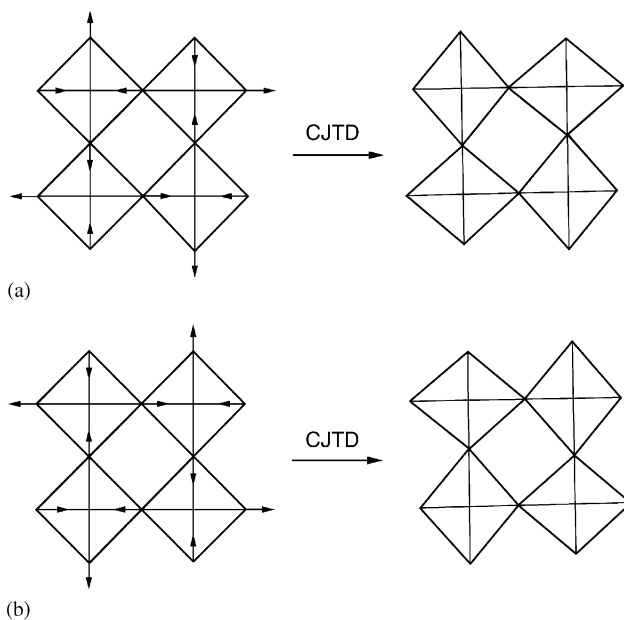

Fig. 32. CJTDs in the two adjacent CuF_4 layers of $KCuF_3$. The directions of the Cu–F bond shortening and elongations are opposite in (a) and (b).
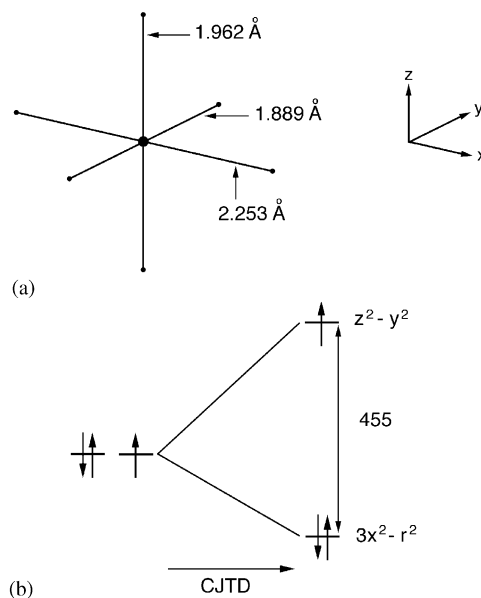

Fig. 33. (a) Cu–F bond lengths of a distorted CuF_6 octahedron in $KCuF_3$. (b) e_g levels of the ideal (left) and distorted (right) CuF_6 octahedra. The energy separation is in meV.

a poor overlap along the c-direction. Thus the four-electron two-orbital destabilizing interaction is minimized in all three directions. The magnetic orbitals (i.e., the singly filled orbitals) have orthogonal arrangements in each CuF_4 layer but leads to a σ-type interaction between adjacent Cu^{2+} sites along the c-direction. Thus the two-electron two-orbital destabilizing interaction is minimized only in the ab-plane. When this orbital ordered state undergoes a CJTD, each Cu^{2+} site lowers the doubly filled level while raising the singly filled level (Figs. 33 and 36) thereby lowering the total energy.

The orbital ordering and CJTD in $KCuF_3$ have an immediate consequence on the spin ordering of $KCuF_3$. As mentioned above, the magnetic orbitals of $KCuF_3$ make a poor overlap in the ab-plane but make a good overlap along the c-direction. Therefore, the J_{AF} term should be negligible in the ab-plane but substantial along the c-direction. This explains why $KCuF_3$ adopts the A-type magnetic structure, i.e., ferromagnetic in the

ab-plane but antiferromagnetic along the c-direction [137].

7.4.2. Short-range orbital ordering and spin exchange interactions of BaVS₃

In $BaVS_3$ the VS_3 chains made up of face-sharing VS_6 octahedra are separated by Ba^{2+} ions, which occupy the 12-coordination sites between three adjacent VS_3 [138].
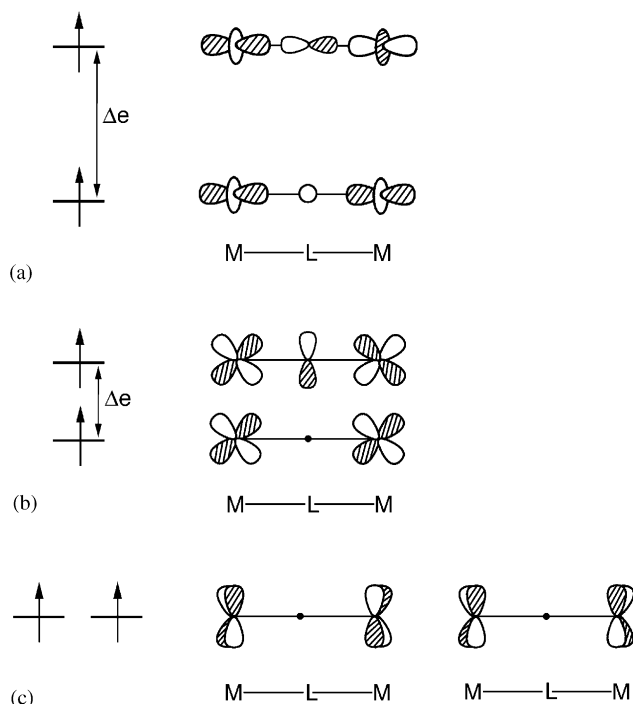
(a)

(b)

Fig. 34. Representative examples of (a) σ-type, (b) π-type and (c) δ-type orbital interactions through a symmetric $M-L-M$ bridge of a cubic perovskite AML_3.

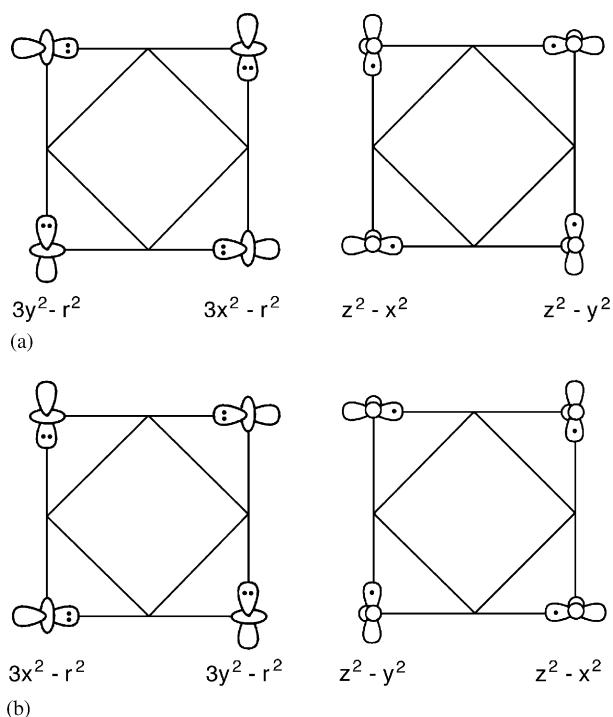$3y^2- r^2$ $3x^2 - r^2$ $z^2 - x^2$ $z^2 - y^2$

(a)

Fig. 36. Orbital ordering that minimizes the orbital interactions between adjacent spin sites in each distorted CuF_4 layer that has unsymmetrical Cu–F$\cdots$Cu bridges.

c

(a)   (b)

b

a

(c)

Fig. 37. Description of the crystal structure of $BaVS_3$: (a) Perspective view of a VS_3 octahedral chain made up of face-sharing VS_6 octahedra in polyhedral representation. (b) Projection view of a VS_3 chain along the chain direction, where the dot represents the position of the V atom. (c) Projection view, along the c-direction, of the arrangements of the VS_3 chains, the V^{4+} ions (dots) and the Ba^{2+} ions (open circles) in the hexagonal structure of $BaVS_3$ at room temperature.

$3y^2- r^2$ $3x^2 - r^2$ $z^2 - x^2$ $z^2 - y^2$

(a)

$3x^2 - r^2$ $3y^2 - r^2$ $z^2 - y^2$ $z^2 - x^2$

(b)

Fig. 35. Two examples of orbital ordering that minimize the orbital interactions between adjacent spin sites in an ideal undistorted CuF_4 layer has symmetric Cu–F–Cu bridges. In both (a) and (b) the arrangement of the doubly filled orbitals is shown on the left, and that of the singly filled orbitals on the right.
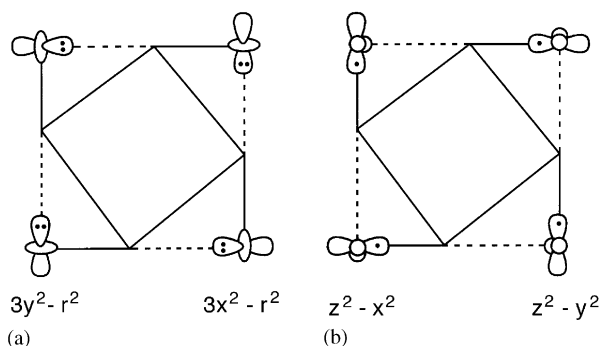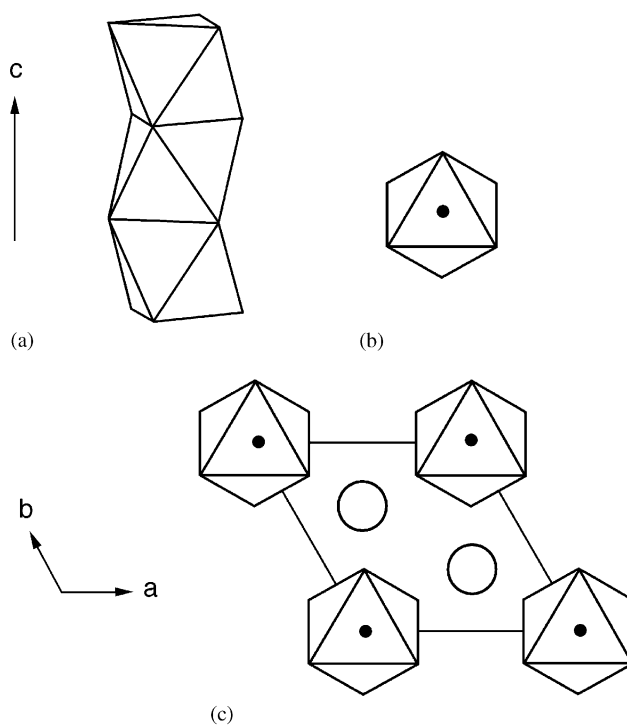
Upon lowering the temperature $BaVS_3$ undergoes three phase transitions; a structural transition at $T_S \approx 240$ K, a metal-insulation (MI) transition at $T_{MI} \approx 70$ K, and a magnetic transition at $T_X \approx 30$ K [139]. At room temperature $BaVS_3$ has the hexagonal perovskite-type structure, and the V^{4+} (d^1) ions in each VS_3 chain form a straight chain (Fig. 37). A powder neutron diffraction study reported that below T_S the V^{4+} (d^1) ions of each VS_3 chain form a zigzag chain in a bc-plane with the
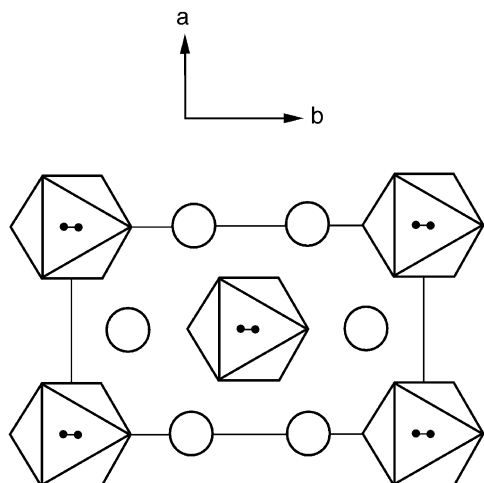
Fig. 38. Projection view, along the c-direction, of the arrangements of the VS$_3$ chains, the V^{4+} ions (dots) and the Ba^{2+} ions (open circles) in the orthorhombic structure of BaVS$_3$ below $\sim$240 K. The zigzagging of the vanadium atoms occurs in a bc-plane.

$\angle$V–V–V angle of $\sim$160° (Fig. 38) [140]. Despite this 1D nature of the structure, the electrical resistivity of BaVS$_3$ is not highly anisotropic but is rather three dimensional [139]. The electrical resistivity of BaVS$_3$ is nearly independent of temperature above T_{MI} and increases sharply below T_{MI} [139,141]. However, a recent X-ray diffraction study [142] of single crystal BaVS$_3$ samples found that there occur superlattice reflections with propagation vector $0.5c^*$ below T_{MI}. Thus, the MI transition involves a spatial order of the lattice and doubles the c-axis length. This work showed that the correct space group for the structure of BaVS$_3$ below T_{MI} is not $Cmc2_1$ [140], but is likely to be $Im2m$ in which two non-equivalent V atoms (say, V$_A$ and V$_B$) repeat as $-$V$_A$–V$_A$–V$_B$–V$_B$–V$_A$–V$_A$–V$_B$–V$_B-$ in each VS$_3$ chain. Subsequently, it was observed [143] that the MI transition of BaVS$_3$ is accompanied by huge 1D structural fluctuations (observable up to 170 K) reminiscent of a pseudo 1D metal.

The magnetic susceptibility of BaVS$_3$ follows a Curie–Weiss behavior above T_{MI} with the reported μ_{eff} values ranging 1.17–1.33 μ_B [144], which amounts to 0.54–0.66 unpaired spin per V. The magnetic susceptibility decreases rapidly below T_{MI} [139,141,144], but ^{51}V NMR and NQR measurements indicate that BaVS$_3$ has a non-magnetic ground state and a spin gap [145]. The latter is explained in terms of an orbital ordering in a spin-singlet state [86,139]. An incommensurate anti-ferromagnetic spin structure sets in below T_X with the ordered magnetic moment of $\sim$0.5 μ_B and the propagation vector $q_{spin} = (0.226a^*, 0.226b^*, 0)$ in the hexagonal setting [146]. Thus the V^{4+} (d^1) sites of BaVS$_3$ are grouped into magnetic and non-magnetic sites in approximately 1:1 ratio [142], and the c-axis length of the ordered spin structure is apparently the same as

that of the room temperature crystal structure (i.e., the c^* component of q_{spin} is zero).

The properties of BaVS$_3$ present a number of puzzling features. The observed electrical resistivity does not exhibit 1D metallic character [139] despite that it consists of 1D chains. Nevertheless, BaVS$_3$ exhibits strong 1D structural fluctuations as if it is a 1D metal. The MI transition doubles the c-axis length in terms of the crystal structure, but the ordered spin structure below T_X appears to have the same c-axis length as does the room temperature crystal structure. With an array of V^{4+} (d^1) ions in each VS$_3$ chain, one might expected a Peierls distortion leading to a V–V$\cdots$V–V$\cdots$ bond alternation, but this does not happen. The 1D structural fluctuations and the superlattice spots of BaVS$_3$ are characterized by the propagation vector $q = 0.5c^*$ [142,143]. For these 1D structural fluctuations to originate from a charge density wave instability, BaVS$_3$ should have a half filled band dispersive mainly along the chain direction (i.e., the c-direction) and the associated Fermi surface should be well nested [147]. These expectations are not supported by the results of the first principles electronic band structure calculations for the normal metallic state of the room temperature structure of BaVS$_3$ [86,148].

The magnetic properties of BaVS$_3$ show that there is 0.54–0.66 spin/V above T_{MI}, and about 0.5 spin/V below T_X. For the discussion of the electronic structure of BaVS$_3$ above T_{MI}, therefore, it is more appropriate to begin from the viewpoint of an electron-localized state in which each V^{4+} site has one localized spin. In discussing the local electronic structure of each V^{4+} site, it is important to note that there are two representations of the t_{2g}-orbitals. For the local coordinate system of a VS$_6$ octahedron in Fig. 39a, the symmetry-adapted t_{2g}-orbitals are given as shown in Fig. 39b–d [86].
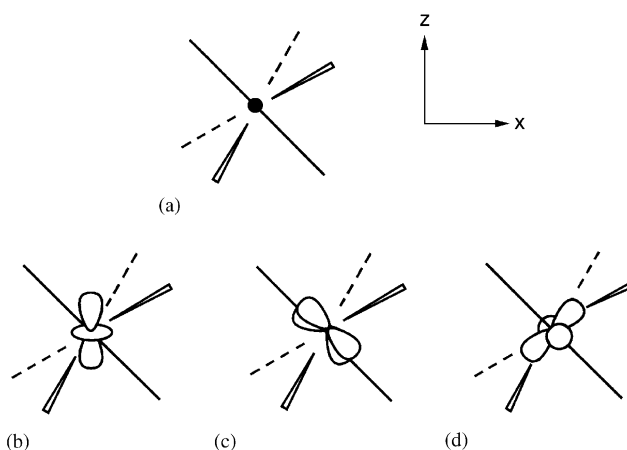

Fig. 39. (a) Local Cartesian coordinate of a VS$_6$ octahedron, in which the z-axis is taken along the three-fold axis of the octahedron. (b–d) d-orbitals contributing to the "symmetry-adapted" t_{2g}-orbitals of a VS$_6$ octahedron. These d-orbitals are $3z^2-r^2$ in (b), $\sqrt{2/3}\,xy - \sqrt{1/3}\,yz$ in (c), and $-\sqrt{2/3}\,(x^2-y^2) - \sqrt{1/3}\,xz$ in (d).
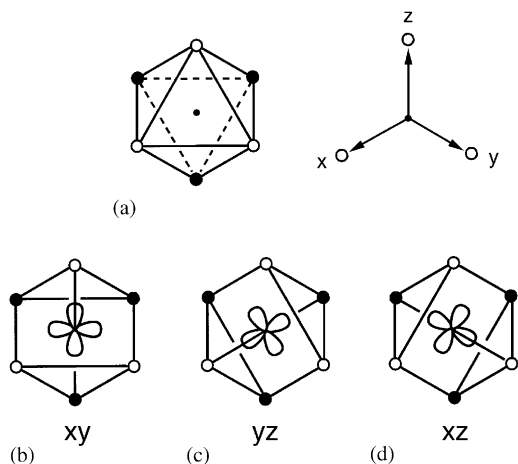
Fig. 40. (a) Alternative choice of the local Cartesian coordinate for a VS$_6$ octahedron. (b–d) d-orbitals contributing to the "symmetry-broken" t_{2g}-block levels of a VS$_6$ octahedron. These d-orbitals are described by xy in (b), yz in (c), and xz in (d).

One of these orbitals is the V $3z^2 - r^2$ orbital (Fig. 39b), which leads to stronger interactions between adjacent V^{4+} ions primarily along the chain direction than along the interchain directions. When the local coordinate system of a VS$_6$ octahedron is chosen as in Fig. 40a, we obtain the "symmetry-broken" t_{2g}-orbitals presented in Fig. 40b–d [86]. The latter have been found useful in describing electronic instabilities such as charge density wave in low-dimensional oxide and chalcogenide metals of transition metal elements [78,147,149].

In the orthorhombic structures of BaVS$_3$, nearest-neighbor "interchain" interactions involving the "symmetry-broken" t_{2g}-orbitals can occur along the $(a + b)$-direction (Fig. 41b), the a-direction (Fig. 41b), and the $(-a + b)$-direction. (The latter is not shown because it is equivalent to that along the $(a + b)$-direction. For simplicity, only the "equatorial" planes containing the "symmetry-broken" t_{2g}-orbitals are shown in Fig. 41a and b.) Each V^{4+} ion has one unpaired spin, which can occupy any one of the three t_{2g}-orbitals. Thus, it is possible that the two t_{2g}-orbitals of Fig. 41a are each singly occupied. Then, as depicted in Fig. 41c, they give rise to an SSE interaction through the V–S$\cdots$S–V paths, for which the overlap between the S $3p$ orbital tails is important. For the V^{4+} (d^1) ion of each spin monomer (VS$_6$)$^{8-}$, the t_{2g}-block levels are singly filled. Suppose that the symmetry-broken t_{2g}-orbitals of (VS$_6$)$^{8-}$ are identified as ξ_1, ξ_2 and ξ_3. Then, according to our discussion of Section 5.4, the strengths of the interchain interactions are estimated in terms of the $\langle (\Delta \varepsilon)^2 \rangle$ values

$$\langle (\Delta \varepsilon)^2 \rangle \approx \frac{1}{9}[(\Delta \varepsilon_{11})^2 + (\Delta \varepsilon_{22})^2 + (\Delta \varepsilon_{33})^2] \quad (7.1)$$

which are calculated by using the spin dimers [(VS$_6$)$^{8-}$]$_2$. The $\langle (\Delta \varepsilon)^2 \rangle$ values calculated for the $(a + b)$- and
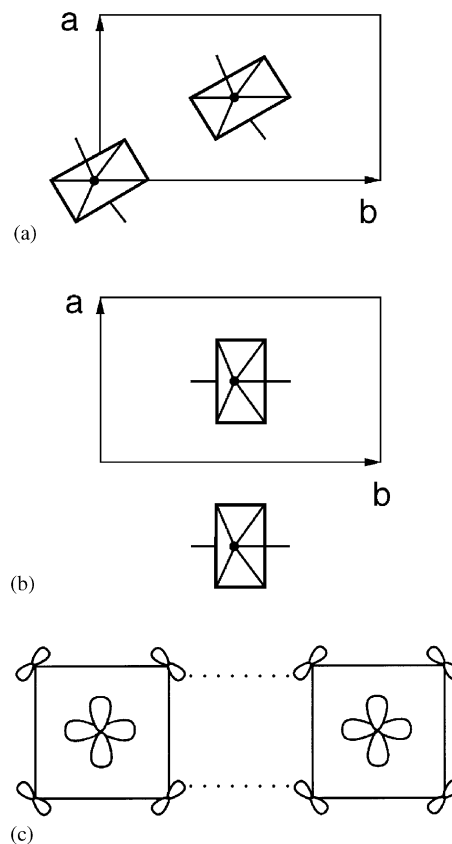

Fig. 41. (a) Arrangement of the "equatorial" planes containing the "symmetry-broken" t_{2g}-orbitals along the $(a + b)$-direction, and (b) that along the a-direction, in the orthorhombic structure of BaVS$_3$. For simplicity, the "symmetry-broken" t_{2g}-orbitals contained in the "equatorial" planes are not shown. The $(a + b)$- and $(-a + b)$-directions are equivalent by symmetry. (c) Overlap between the S $3p$ orbital tails of the magnetic orbitals contained in the "equatorial" planes of (a) and (b). The overlap leads to super-superexchange (V-S$\cdots$S–V) interactions.

Table 13
$\langle (\Delta \varepsilon)^2 \rangle$ values[a] of the interchain spin exchange interactions calculated for the room temperature and 110, 60 and 5 K crystal structures of BaVS$_3$

	Along $(a + b)$	Along a
Room temperature	2400	2400
110 K	5200	3500
60 K	6800	2100
5 K	5800	1900

[a] In units of (meV)^2.

a-directions are summarized in Table 13. It is clear that below 70 K, the antiferromagnetic interaction along the $(a + b)$- and $(-a + b)$-directions are stronger than that along the a-direction by a factor of three. The interchain SSE interaction of any given V^{4+} site may take place along the $(a + b)$-, $(-a + b)$- or a-direction. If such interactions occur randomly in each plane of VS$_6$ octahedra parallel to the ab-plane (e.g., see Fig. 42), then there will be no long range magnetic ordering
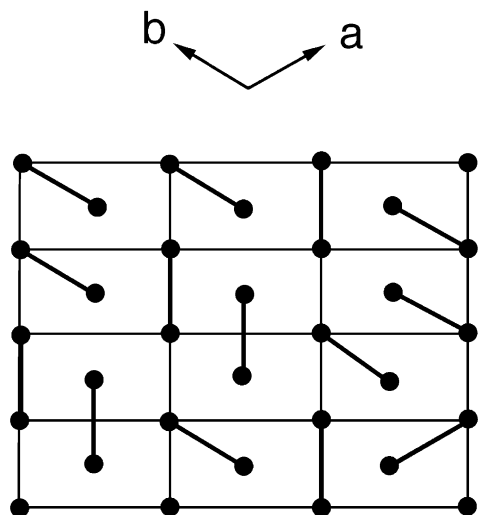
Fig. 42. Random arrangement of antiferromagnetically coupled interchain spin dimers (represented by solid lines) within a layer of VS_6 octahedra parallel to the *ab*-plane, where the repeat vectors **a** and **b** refer to the hexagonal setting. The dots represent the V^{4+} ion positions.

Fig. 43. Two broken-symmetry electronic states of a VS_3 chain, where the V atoms are represented by shaded circles.

although spins are all paired up via nearest-neighbor interchain spin exchange interactions [86,139,145]. Such a state describes the magnetic structure of $BaVS_3$ between T_{MI} and T_X.

If the correct space group of $BaVS_3$ is *Im2m* below T_{MI}, as deduced by Inami et al., [142] two non-equivalent V atoms repeat as $(-V_A-V_A-V_B-V_B-)_\infty$ in each VS_3 chain so that the *c*-axis doubling comes about naturally. To explain the structural and magnetic properties of $BaVS_3$ under the constraint that the V^{4+} (d^1) ions are separated into magnetic and non-magnetic sites in approximately 1:1 ratio, two symmetry-broken electronic structures have been proposed [142,143]. Inami et al. [142] considered the possibility state in which two electrons in one pair of vanadium (e.g., V_A-V_A) form a singlet ground state, and those in the other pair (e.g., V_B-V_B) are localized (*Model* 1) (Fig. 43). As Fagot et al. suggested [143], it is reasonable to suppose that the V_A sites utilize the $3z^2-r^2$ orbitals (symmetry-adapted). These orbitals will produce a σ-bonding level and accommodate two electrons forming a singlet ground state so that each V_A-V_A pair becomes non-magnetic. For the V_B sites to be magnetic, symmetry-broken t_{2g} orbitals are more effective than the symmetry-adapted t_{2g} orbitals because the former diminishes orbital overlap between adjacent V sites [86]. The spin structure of *Model* 1 doubles the *c*-axis length, in apparent disagreement with the ordered spin structure deduced from powder neutron diffraction [146]. Fagot et al. [143] considered an alternative possibility that every second V atom along each chain has one electron in the $3z^2-r^2$ orbital, and each of the remaining V atoms has a localized spin (*Model* 2)
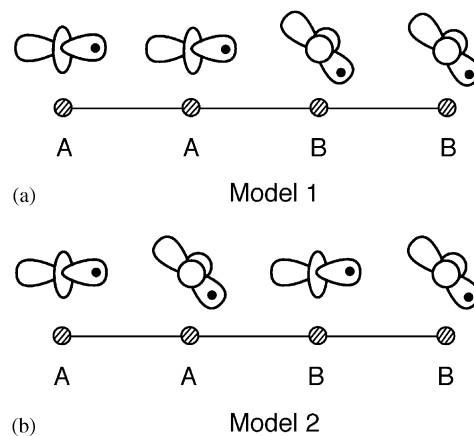
(Fig. 43b). This model does not double the *c*-axis as far as the spin structure is concerned, but is incompatible with the space group *Im2m*, because it generates four non-equivalent V atoms (i.e., two different V_A and two different V_B atoms).

It should be recalled that the ferromagnetic ordering along the *c*-direction (i.e., the c^* component of q_{spin} is zero) was not deduced experimentally, but was rather assumed in order to determine the propagation vector in the *ab*-plane from the powder neutron diffraction data [146]. Therefore, it is critical to know if *Model* 1 is consistent with the vector q_{spin} thus determined. For this purpose, we first consider the possible nature of spin ordering in the *ab*-plane. A 1D arrangement of VS_3 chains appropriate for *Model* 1 is one in which two consecutive sheets of V_AS_6 octahedra (parallel to the *ab*-plane) alternate with two consecutive sheets of V_BS_6 octahedra along the *c*-direction. In $BaVS_3$ each Ba atom is located at the center of a V_6 trigonal prism. The above 1D arrangement of VS_3 chains generates four BaV_6 trigonal prisms for every $V_A-V_A-V_B-V_B$ unit, i.e., one $Ba(V_A)_6$, one $Ba(V_B)_6$ and two $Ba(V_A)_3(V_B)_3$. This is consistent with the expected Ba positions from the space group *Im2m* [142]. Suppose that each V_A-V_A pair along the chain direction forms a σ-bonding level, and the unpaired spins in each sheet of V_BS_6 octahedra order through super-superexchange interactions in the *ab*-plane [86]. The decrease of the magnetic susceptibility below T_{MI} and the lack of long range spin order between T_{MI} and T_X are explained in terms of random arrangements of antiferromagnetically coupled interchain spin dimers $(V_BS_6)_2$ within the sheets of V_BS_6 octahedra (Fig. 42) [86,139]. In this picture, the occurrence of an ordered incommensurate spin structure in each sheet of V_BS_6 octahedra should be a consequence of ordering such spin dimers. Fig. 44 shows an example of a $\sqrt{21} \times \sqrt{21}$ superstructure with repeat vectors $\mathbf{a}' = 5\mathbf{a} + \mathbf{b}$ and $\mathbf{b}' = 4\mathbf{b} - \mathbf{a}$ (here **a** and **b** are the
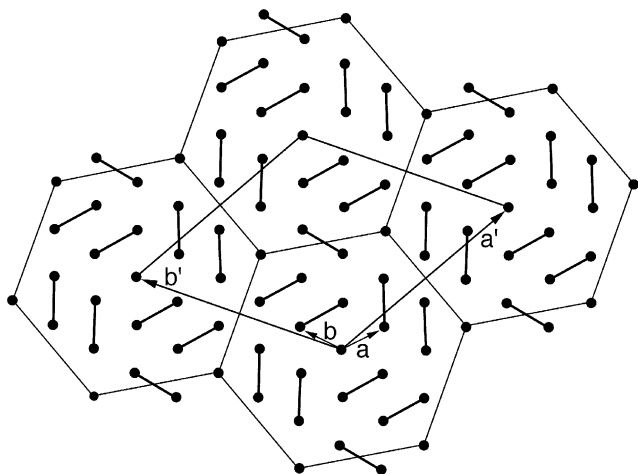
Fig. 44. $\sqrt{21} \times \sqrt{21}$ superstructure of spin dimer ordering, where the repeat vectors **a** and **b** refer to the hexagonal setting. The dots represent the V^{4+} ion positions.

repeat vectors of the hexagonal room temperature structure) [150]. The propagation vector of this superstructure in reciprocal space is $(0.218a^*, 0.218b^*)$, which is close to that of the reported incommensurate structure, i.e., $(0.226a^*, 0.226b^*)$ [146].

The 1D spin structure of $BaVS_3$ below T_X can be described in terms of ordering, along the c-direction, the $\sqrt{21} \times \sqrt{21}$ superstructures formed in the sheets of V_BS_6 octahedra. Spin exchange interactions along the c-direction are possible between adjacent sheets of V_BS_6 octahedra joined by face sharing, but not between those separated by sheets of V_AS_6 octahedra. Along the c-direction, therefore, the $\sqrt{21} \times \sqrt{21}$ superstructures formed in the sheets of V_BS_6 octahedra would propagate without any repeat pattern. Powder neutron diffraction patterns for such a random ordering would be well described by the assumption that the c^* component of the propagation vector is zero. Thus, *Model* 1 is consistent with the vector $q_{\text{spin}} = (0.226a^*, 0.226b^*, 0)$ if the spin ordering along the c-direction is random [150].

Since the properties of $BaVS_3$ are explained in terms of the broken-symmetry electronic state, *Model* 1, it is important to ask why such a state can become the ground state to begin with. For our discussion, it is necessary to consider two opposing energy factors, i.e., lattice strain and cooperative Jahn–Teller distortion [150]. $BaVS_3$ has a close packed hexagonal arrangement of VS_3 chains, and each Ba^{2+} ion is located in a pocket of 12 S atoms in the channels created by three adjacent chains. In addition, the nearest-neighbor V–V distance of the VS_3 chain is very short (i.e., 2.805 Å) due to the face sharing. In this compact structure, a V–V···V–V··· bond alternation along the chain is energetically unfavorable because it forces a change in the V–S bond lengths and a shortening of the Ba–S contact distances and hence leads to severe lattice strain. *Model* 1 requires

every fourth V–V pair of each chain to form a V–V σ-bonding level and induces less severe lattice strain than does the V–V···V–V··· bond alternation. The V^{4+} (d^1) ion of each VS_6 octahedron has Jahn–Teller instability. The crystal structures of $BaVS_3$ determined below T_S [140] (Fig. 38) suggest that the preferred distortion for lifting the t_{2g} level degeneracy is one in which the V atom of each VS_6 octahedron moves toward one S_3 triangle face. Then, at a given VS_6 octahedron of a VS_3 chain, the V atom can move toward a shared face along the chain or toward triangular faces in the direction perpendicular to the chain. In each $V_A - V_A$ pair, it is energetically favorable for the V_A atoms to move toward each other along the chain and form a σ-bonding level. In order to avoid strong lattice strain, the V_B atoms in each $V_B - V_B$ pair cannot follow the same distortion pattern. Then the V_B atoms should move either away from each other along the chain or in the direction perpendicular to the chain. Thus, in a $V_B - V_B$ pair, shortening of the $V_B - V_B$ distance and formation of a σ-bonding are prevented so that the V_B atoms remain magnetic.

The symmetry-broken state, *Model* 1, should arise as a consequence of balancing two opposing energy terms, i.e., stabilization from cooperative Jahn–Teller distortions and destabilization from the associated lattice strain. In terms of *Model* 1, the 1D structural fluctuations in $BaVS_3$ mean that regions of short-range cooperative Jahn–Teller distortions are formed and destroyed dynamically in individual VS_3 chains. The 1D structural fluctuations in each VS_3 chain will reduce the mean free path, and lower the mobility, of electrons mainly along the chain direction. Thus strong 1D metallic conductivity is absent in $BaVS_3$.

7.5. Anisotropy in the spin exchange interactions of AV_3O_7 (M=Cd, Ca, Sr)

AV_3O_7 ($A = \text{Cd, Ca, Sr}$) consists of V_3O_7 layers (Fig. 45a) that are made up of edge-sharing VO_5 square pyramids possessing V^{4+} (d^1) ions [151,152]. The A^{2+} ions occupy the sites of the V_3O_7 layers where V^{4+} ions are missing. Each V_3O_7 layer has two kinds of vanadium atoms and two kinds of oxygen atoms (Fig. 45b). As a function of temperature the magnetic susceptibilities of AV_3O_7 exhibit a broad maximum (Fig. 46) hence indicating the occurrence of an antiferromagnetic ordering [151]. If these susceptibility curves are fitted with a Heisenberg linear antiferromagnetic chain model, one obtains the values of T_{max} at which the magnetic susceptibility curves show a maximum. Then, using the relationship [34]

$$-J/k_B = 1.560\, T_{\text{max}} \tag{7.2}$$

the value of the spin exchange parameter J for the Heisenberg linear antiferromagnetic chain can be

estimated. The T_{max} and J values thus determined for AV_3O_7, along with the ionic radii of the A^{2+} ions, are listed in Table 14 [151]. According to this analysis the
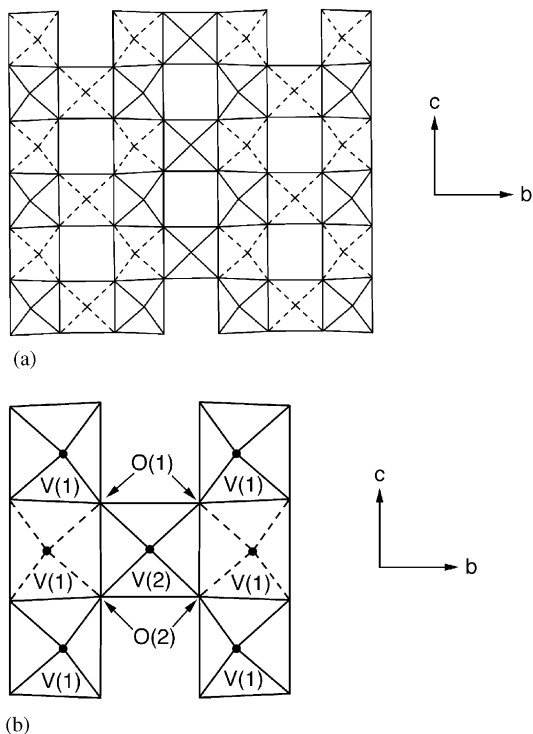

(a)

(b)

Fig. 45. (a) Schematic projection view of the V_3O_7 layer of AV_3O_7 (M = Cd, Ca, Sr). In each square with solid (dashed) diagonal lines, the apical oxygen of a VO_5 square pyramid lies above (below) the basal plane. (b) Definition of the V(1), V(2), O(1) and O(2) atoms in the V_3O_7 layer.

magnitude of J increases in the order, $CdV_3O_7 < CaV_3O_7 < SrV_3O_7$, thereby suggesting that the extent of 1D character increases in the same order. This suggestion is a direct consequence of the 1D model used to analyze the experimental data, and is erroneous as discussed below.

The spin exchange interactions of CaV_3O_7 were examined by DFT calculations using the LDA + U potential [50]. In our earlier spin dimer analysis [154] of AV_3O_7 (A = Cd, Ca, Sr), the crystal structures of Liu and Greedan [151] were used, and the oxygen $2p$ orbital parameters employed for EHTB calculations were not calibrated (Section 6.3). Recently, Nishiguchi et al. [152] reported more accurate crystal structures of CdV_3O_7 and CaV_3O_7 as well as a new crystal structure of $Ca_{0.55}Sr_{0.45}V_3O_7$. Results of spin dimer analysis depend critically on the accuracy of the structural data used [26] and on the diffuseness of the oxygen $2p$ orbitals (Section 6.3) [26,82]. Therefore, we reexamine the spin exchange interactions of AV_3O_7 using these structural data using the calibrated oxygen $2p$ orbital. There are four

Table 14
J and T_{max} values of AV_3O_7 and ionic radius r of A^{2+} [a]

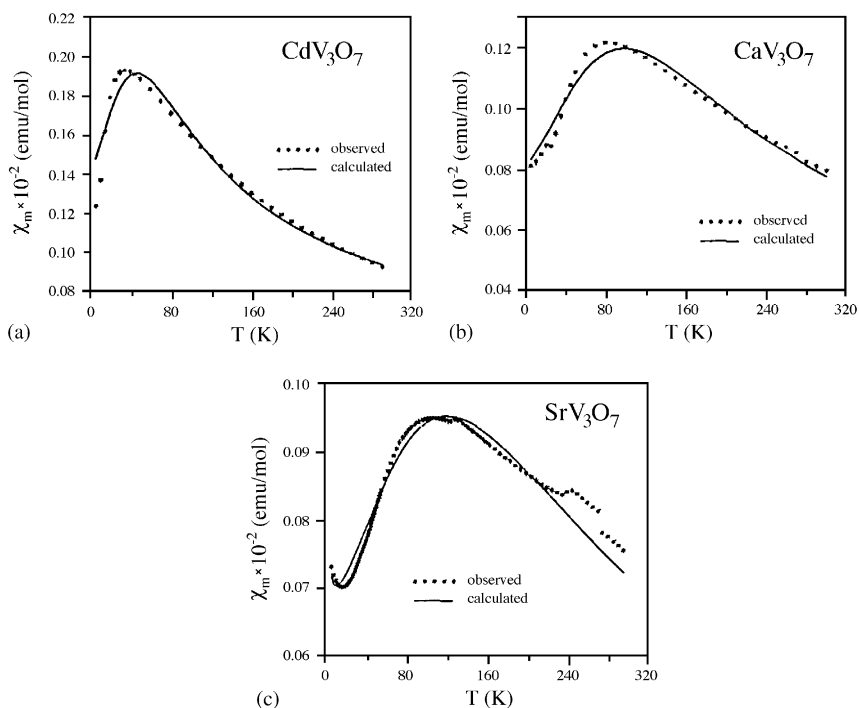|		CdV_3O_7	CaV_3O_7	SrV_3O_7
r (A^{2+})	(Å)	1.17	1.20	1.35
T_{max}	(K)	35	80	110
$-J/k_B$	(K)	37.0	76.6	95.5

[a] Taken from Ref. [151].

(a)

(b)

(c)

Fig. 46. Magnetic susceptibility of AV_3O_7 (M = Cd, Ca, Sr) as a function of temperature. (a) A = Cd, (b) A = Ca, and (c) A = Sr.

exchange paths of AV_3O_7 to consider as specified in Table 15. In Fig. 47 the solid lines refer to corner-sharing SE interactions, and the dotted lines to edge-sharing SE interactions. From the relative $(\Delta\varepsilon)^2$ values of Table 15, the following are observed: (1) The strongly interacting spin units are given by the zigzag chains defined by J_1 and J_2, these chains are practically the same for all three compounds, and J_1 and J_2 are about the same. (2) J_4 is weakest and is practically the same in the three compounds. (3) J_3 increases in the order, $CdV_3O_7 < CaV_3O_7 < Ca_{0.55}Sr_{0.45}V_3O_7$.

The above observations show that the interactions within the strongly interacting spin units are essentially identical in three compounds, while those between the strongly interacting spin units increase in the order $CdV_3O_7 < CaV_3O_7 < SrV_3O_7$. (Here we assume that the trend observed between CaV_3O_7 and $Ca_{0.55}Sr_{0.45}V_3O_7$ will be extended linearly to SrV_3O_7.) Consequently, the observed increase in T_{max} in the order $CdV_3O_7 < CaV_3O_7 < SrV_3O_7$ should be related to the fact that the strength of the interchain interaction increases in the same order. In other words, the 2D character of the magnetic lattice is strongest in SrV_3O_7, and weakest in CdV_3O_7. In order to estimate the spin exchange

Table 15
Relative values of $(\Delta\varepsilon)^2$ in AV_3O_7[a]

	V–O–V bridge	Cd	Ca	$Ca_{0.55}Sr_{0.45}$
J_1	Corner-sharing V(1)–O(2)–V(2)	1.00[a]	0.97	0.97
J_2	Corner-sharing V(1)–O(1)–V(2)	0.90	0.89	0.97
J_3	Edge-sharing V(1)–O(1)–V(1) V(1)–O(2)–V(1)	0.43	0.55	0.70
J_4	Edge-sharing V(1)–O(1)–V(2) V(1)–O(2)–V(2)	0.32	0.27	0.27

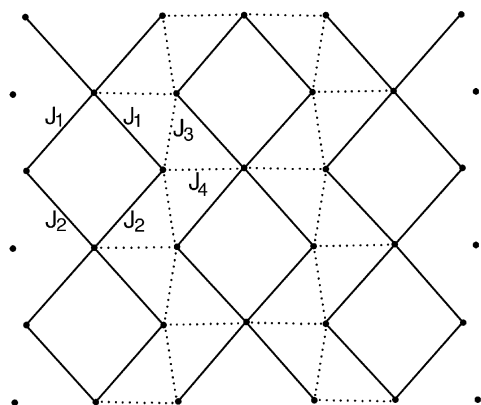[a] $(\Delta\varepsilon)^2 = 17,500\,(meV)^2$ was taken as the reference.

Fig. 47. Four spin exchange paths of the V_3O_7 layer in AV_3O_7. The solid lines refer to corner-sharing SE interactions, and the dotted line edge-sharing SE interactions.

parameters of these compounds, Nishiguchi et al. [156] fitted the magnetic susceptibility data in terms of high-temperature series expansion assuming that $J_1 = J_2$. Their analysis shows that J_1 and J_2 are strongly antiferromagnetic in CdV_3O_7, CaV_3O_7 and SrV_3O_7, that J_4 is ferromagnetic in the three compounds, and that J_3 is ferromagnetic in CdV_3O_7, is antiferromagnetic in CaV_3O_7, and becomes more strongly antiferromagnetic in SrV_3O_7. In the case of SrV_3O_7 the maximum strength of J_3 can be as high as the minimum strength of J_1 and J_2 within the error bounds given [152]. These results are entirely consistent with the relative strengths of the four spin exchange paths summarized in Table 15.

It is of interest to examine why the J_1 and J_2 values are nearly the same in CdV_3O_7, CaV_3O_7 and $Ca_{0.55}Sr_{0.45}V_3O_7$ and why the three compounds are distinguished in the J_3 values. The geometrical parameters of the V–O–V linkages associated with the exchange paths J_1 and J_2 are summarized Table 16. The average V–O lengths increase in the order $CdV_3O_7 < CaV_3O_7 < Ca_{0.55}Sr_{0.45}V_3O_7$, which should weaken [66] the spin exchange interaction in the same order. However, the average $\angle$ V–O–V angles increase in the same order, which should strengthen [24] the spin exchange interaction in the same order. Due to the canceling of the two opposing effects, the J_1 and J_2 values are nearly the same in the three compounds. The geometrical parameters of the V–O–V linkages associated with the exchange path J_3 are summarized Table 17. It is noted that the $\angle$ V–O–V angles are nearly the same in three compounds, and so are the average V–O lengths. However, the extent of the

Table 16
Geometrical parameters of the V–O–V linkages associated with the exchange paths J_1 and J_2

		J_1	J_2
CdV_3O_7	V–O (Å)	1.953, 1.964	1.954, 1.978
	$\angle$ V–O–V (deg)	127.9	131.2
CaV_3O_7	V–O (Å)	1.964, 1.962	1.961, 1.978
	$\angle$ V–O–V (deg)	128.3	132.3
$Ca_{0.55}Sr_{0.45}V_3O_7$	V-O (Å)	1.964, 1.973	1.960, 1.976
	$\angle$ V–O–V (deg)	131.2	133.6

Table 17
Geometrical parameters of the V–O–V linkages associated with the exchange paths J_3

		V(1)–O(1)–V(1)	V(1)–O(2)–V(1)
CdV_3O_7	V–O (Å)	1.953, 1.975	1.954, 1.966
	$\angle$ V–O–V (deg)	99.2	99.4
CaV_3O_7	V–O (Å)	1.964, 1.972	1.960, 1.961
	$\angle$ V–O–V (deg)	98.5	99.0
$Ca_{0.55}Sr_{0.45}V_3O_7$	V–O (Å)	1.964, 1.968	1.960, 1.966
	$\angle$ V–O–V (deg)	98.1	98.3

asymmetry in the V–O lengths of the V(1)–O(1)–V(1) linkage increases in the $CdV_3O_7 < CaV_3O_7 < Ca_{0.55}Sr_{0.45}$ V_3O_7. This explains why the strength of J_3 increases in the same order.

7.6. Trends in the magnetic susceptibilities of AV_4O_9 ($A=Ca$, Cs_2, DPP)

The vanadium oxides AV_4O_9 ($A = Ca, Cs_2$, DPP) consists of V_4O_9 layers that are made up of VO_5 square pyramids containing V^{4+} (d^1) ions [153,155–157], where DPP represents diprotonated piperazine NH_2 $(CH_2CH_2)_2NH_2$. For different cations A^{2+}, the V_4O_9 layers differ in the way the VO_5 square pyramids are condensed as shown in Fig. 48, where each small square with solid (dotted) diagonal lines represents a VO_5 square pyramid having the apical oxygen atom above (below) the basal plane, and each large square consisting of four small squares represents a plaquette. The magnetic susceptibilities of $(DPP)V_4O_9$, CaV_4O_9 and $Cs_2V_4O_9$ show a broad maximum at $T_{max} \approx 30, 100$ and 600, as depicted in Fig. 49 [153,156,157]. The susceptibility plots exhibit several striking features. (1) The T_{max} value shows a wide variation and increases in the order $(DPP)V_4O_9 < CaV_4O_9 < Cs_2V_4O_9$. (2) The susceptibility at T_{max} (i.e., χ_{max}) increases in the opposite order, i.e., $(DPP)V_4O_9 > CaV_4O_9 > Cs_2V_4O_9$. (3) The room

(a) $(DPP)V_4O_9$ (b) CaV_4O_9

(c) $Cs_2V_4O_9$

Fig. 48. Condensation patterns of the V_4O_9 layers of (a) $(DPP)V_4O_9$, (b) CaV_4O_9, and (c) $Cs_2V_4O_9$. Each small square with solid (dotted) diagonal lines represents a VO_5 square pyramid having the apical oxygen atom above (below) the basal plane, and the large square made up of four small squares represents a plaquette.

temperature susceptibility of $(DPP)V_4O_9$ is nearly twice as high as the χ_{max} of CaV_4O_9. In the following we examine these trends by considering the spin exchange interactions of these compounds.

The spin exchange parameters of CaV_4O_9 are known for four exchange paths from the neutron inelastic scattering and magnetic susceptibility studies [158,159] and from first principles electronic structure calculations (Table 18) [50,159]. From the calculated $(\Delta\varepsilon)^2$ for these exchange paths, we estimate the exchange parameters using the relationship $-(\Delta\varepsilon)^2/U_{eff}$, where the U_{eff} value of 1.587 eV is chosen to reproduce the strongest J value [162]. Clearly, the relative strengths of the four experimental J values are well reproduced by the $-(\Delta\varepsilon)^2/U_{eff}$ values (Table 18). Calculations of the $\Delta\varepsilon$ values for AV_4O_9 ($A = $ DPP, Ca, Cs_2) show [162] that the strongest spin exchange interactions form zigzag linear tetramers in $(DPP)V_4O_9$ (Fig. 50a), squares in CaV_4O_9 (Fig. 50b), and dimers in $Cs_2V_4O_9$ (Fig. 50c). To a first approximation, the magnetic excitation energies of AV_4O_9 are largely determined by the energy gap between the ground and the first excited states of their strongly interacting spin units. To estimate the relative magnitudes of these excitation energies, we set up spin Hamiltonians for the strongly interacting spin units using the spin exchange parameters appropriate for the dimer, square and zigzag linear tetramer units shown in Fig. 51.
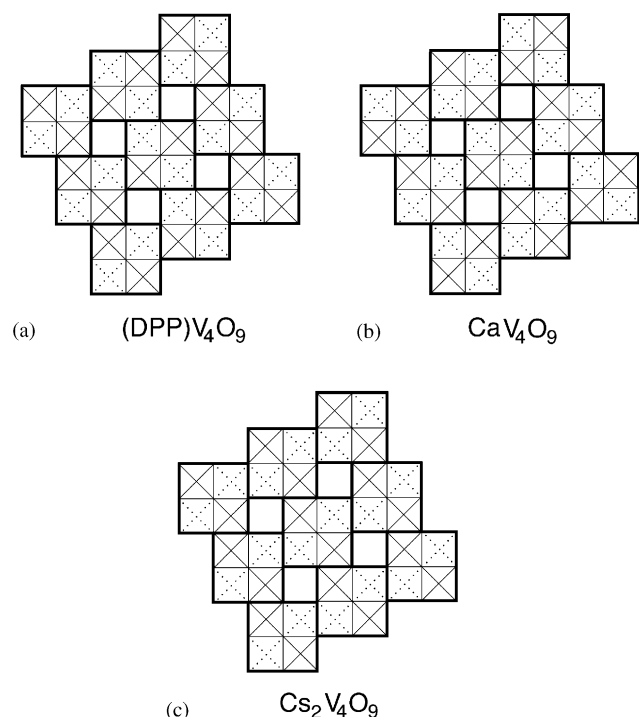
Dimer : $\hat{H}_1 = -J_4\hat{S}_1 \cdot \hat{S}_2$,

Square : $\hat{H}_2 = -J_3(\hat{S}_1 \cdot \hat{S}_2 + \hat{S}_2 \cdot \hat{S}_3 + \hat{S}_3 \cdot \hat{S}_4 + \hat{S}_4 \cdot \hat{S}_1)$,

Zigzag linear tetramer :

$$\hat{H}_3 = -J_2\hat{S}_2 \cdot \hat{S}_3 - J_1(\hat{S}_1 \cdot \hat{S}_2 + \hat{S}_3 \cdot \hat{S}_4).$$

The relative energies of the ground and excited states of the Hamiltonians $\hat{H}_1$ and $\hat{H}_2$ are depicted in Fig. 52. The spin states of the Hamiltonian $\hat{H}_3$ have the following energies

$$E_6 = -\frac{J_1}{2} - \frac{J_2}{4},$$

$$E_5 = \frac{\sqrt{J_1^2 + J_2^2}}{2} + \frac{J_2}{4},$$

$$E_4 = \frac{\sqrt{4J_1^2 - 2J_1J_2 + J_2^2}}{2} + \frac{J_1}{2} + \frac{J_2}{4},$$

$$E_3 = \frac{J_1}{2} - \frac{J_2}{4},$$

$$E_2 = -\frac{\sqrt{J_1^2 + J_2^2}}{2} + \frac{J_2}{4},$$

$$E_1 = -\frac{\sqrt{4J_1^2 - 2J_1J_2 + J_2^2}}{2} + \frac{J_1}{2} + \frac{J_2}{4},$$
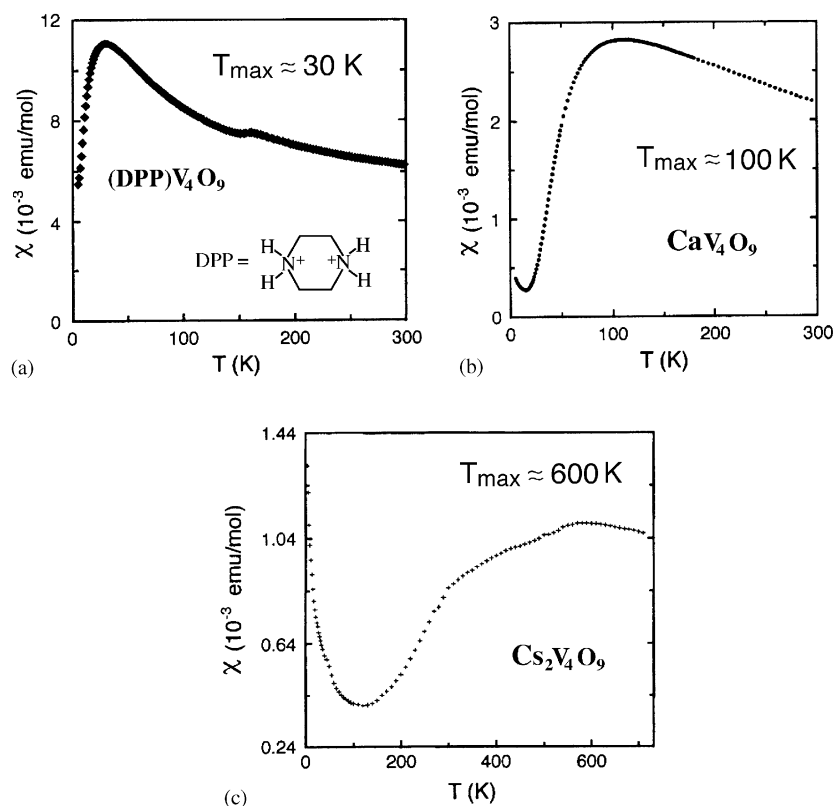
Fig. 49. Magnetic susceptibilities of (a) (DPP)V_4O_9, (b) CaV_4O_9 and (c) $Cs_2V_4O_9$ as a function of temperature.

Table 18
Experimental and calculated spin exchange parameters of CaV_4O_9 (in meV) for the corner- and edge-sharing exchange paths

	Intraplaquette		Interplaquette	
	Edge	Corner	Edge	Corner
(a) Experiment				
Neutron scattering[a]	−5.76	−1.25	−5.76	−14.73
Magnetic susceptibility[b]	−9.3	−3.7	−9.6	−14.2
(b) Electronic structure calculations				
LDA + U[c]	−7.67	−7.84	−5.34	−12.75
LSDA[b]	−8.9	−6.5	−1.1	−23.8
SCAD[b]	−9.7	−3.9	−12.5	−19.3
$-(\Delta\varepsilon)^2/U_{eff}$[d]	−6.36	−4.18	−5.54	−14.73

[a] Taniguchi et al. [158].
[b] Hellberg et al. [159].
[c] Korotin et al. [50].
[d] $U_{eff} = 1.587$ eV.

where E_1 is the ground state if J_1 and J_2 are both antiferromagnetic. Fig. 53 plots how the energies of the four lowest-lying spin states (i.e., E_1, E_2, E_3, E_4) vary as a function of the ratio J_2/J_1 in the range of 1–3. The relative strengths of the parameters J_1, J_2, J_3 and J_4 can be determined by using the corresponding $(\Delta\varepsilon)^2$ values calculated from spin dimer analysis. Use of the uncalibrated O $2p$ orbital leads to $J_2 \approx 4.0J_1$,

(a) (DPP)V_4O_9 (b) CaV_4O_9
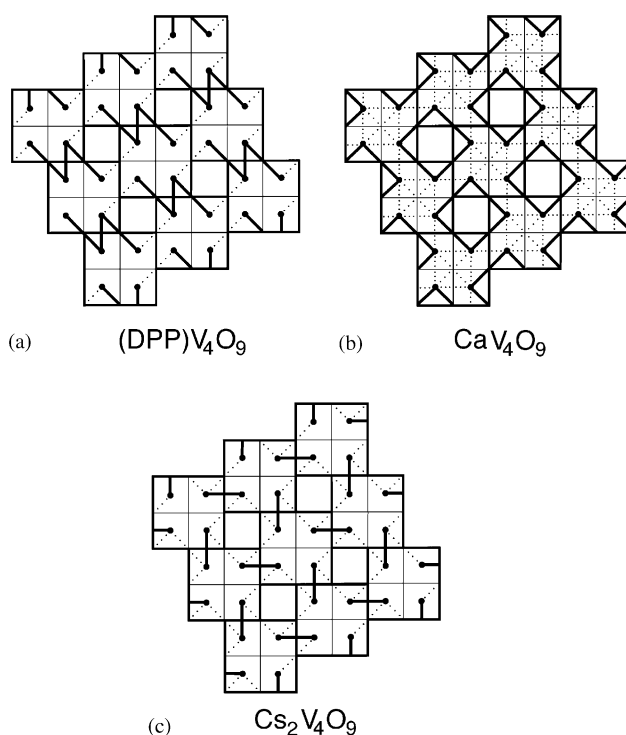
(c) $Cs_2V_4O_9$

Fig. 50. Simplified representation of spin exchange interactions in (a) (DPP)V_4O_9, (b) CaV_4O_9, and (c) $Cs_2V_4O_9$. The solid lines indicate the strongly interacting spin units, and the dotted lines represent the weaker interactions between the strongly interacting spin units.
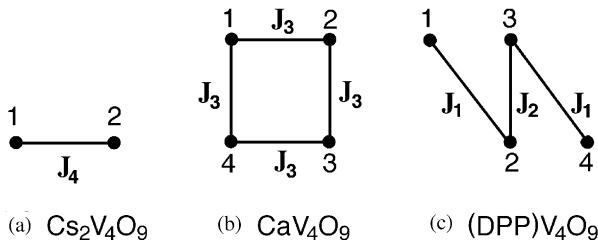
Fig. 51. Spin exchange parameters of the strongly interacting spin units of AV_4O_9: (a) the dimer unit of $Cs_2V_4O_9$, (b) the square unit of CaV_4O_9 and the zigzag linear tetramer unit of $(DPP)V_4O_9$.
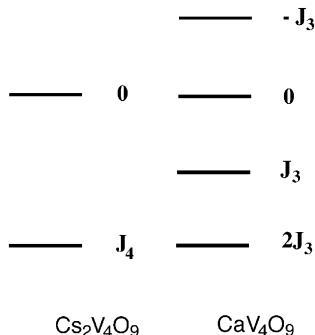

Fig. 52. Energies of the spin states for (a) the dimer unit of $Cs_2V_4O_9$ in terms of J_4 and (b) the square unit of CaV_4O_9 in terms of J_3.
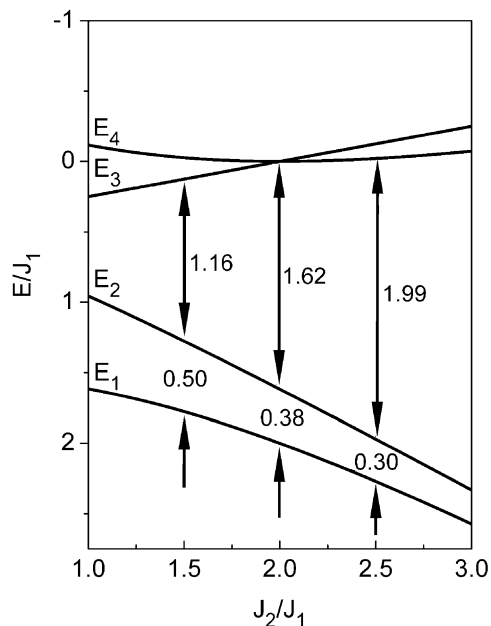

Fig. 53. Energies of the lowest-four spin states of the zigzag linear tetramer unit of $(DPP)V_4O_9$ in terms of J_1 as a function of the ratio J_2/J_1 in the range of 1–3 (both J_1 and J_2 are assumed to be antiferromagnetic).

$J_3 \approx 0.75J_1$, and $J_4 \approx 2.1J_1$ [162], while use of the calibrated O $2p$ orbital leads to $J_2 \approx 1.2J_1$, $J_3 \approx 0.60J_1$, and $J_4 \approx 2.6J_1$ (see Section 6.3). The first excitation energy of the dimer unit in $Cs_2V_4O_9$ is $|J_4|$, which is

greater than $2|J_1|$ in both estimates. The first excitation energy of the square unit in CaV_4O_9 is $|J_3|$, which is approximately $0.7 |J_1|$ in both estimates. The first excitation energy of the zigzag linear tetramer in $(DPP)V_4O_9$ depends on the $|J_2/J_1|$ ratio (Fig. 53), and becomes much smaller than $|J_3|$ if the ratio is increased beyond 1.2. Thus, the first excitation energies of $(DPP)V_4O_9$, CaV_4O_9 and $Cs_2V_4O_9$ are expected to increase in the order $(DPP)V_4O_9 < CaV_4O_9 < Cs_2V_4O_9$. This explains the trends in the magnetic susceptibilities of $(DPP)V_4O_9$, CaV_4O_9 and $Cs_2V_4O_9$ pointed out above.

7.7. Anisotropy in the spin exchange interactions of α'-NaV_2O_5, CaV_2O_5 and MgV_2O_5

The oxides α'-NaV_2O_5 [160,163], CaV_2O_5 [161,164] and MgV_2O_5 [165,166] consist of V_2O_5 layers that are made up of VO_5 square pyramids (Fig. 54). The arrangement of the vanadium atoms in this layer (Fig. 54) may be described as made up of two-leg ladders [167]. In each ladder chain, adjacent VO_5 square pyramids are joined by corner sharing along the legs and in the rungs. Between adjacent ladder chains, neighboring VO_5 square pyramids are joined by edge sharing. All vanadium atoms of CaV_2O_5 and MgV_2O_5 are in the oxidation state $+4$, so there exists one unpaired spin at each vanadium site. The magnetic susceptibility of CaV_2O_5 and MgV_2O_5 is described by three different spin–spin exchange parameters (i.e., J_r, J_l and J_e in Fig. 54) [167,168]. In contrast, there is one unpaired spin per two vanadium atoms in α'-NaV_2O_5, and the magnetic susceptibility of α'-NaV_2O_5 above 100 K is described by one spin exchange parameter [167,169]. It is important to understand how α'-NaV_2O_5 exhibits the magnetic 1D character despite the fact that it has a 2D layered structure as do CaV_2O_5 and MgV_2O_5 [154,170]. It is also interesting to examine if CaV_2O_5 and MgV_2O_5 can be described as a spin ladder system in terms of the spin exchange interactions between spin sites.

A spin monomer in the V_2O_5 layers of CaV_2O_5 and MgV_2O_5 is represented by the $(VO_5)^{6-}$ square pyramid containing a V^{4+} ion. Thus a corner-sharing spin dimer of CaV_2O_5 and MgV_2O_5 is represented by $(V_2O_9)^{10-}$ (Fig. 55a and b), and an edge-sharing spin dimer of CaV_2O_5 and MgV_2O_5 by $(V_2O_8)^{8-}$ (Fig. 55c). For a spin monomer of CaV_2O_5 and MgV_2O_5, the magnetic orbital ψ is represented by the xy orbital (Fig. 56a). In such spin dimers, the two magnetic orbitals ψ interact to form bonding and antibonding levels (ψ_+ and ψ_-, respectively), and these levels are each singly occupied (Fig. 56b).

There is only one unpaired spin per formula unit in α'-NaV_2O_5, and all vanadium atoms are equivalent [154,160]. Therefore, in the spin dimers representing two
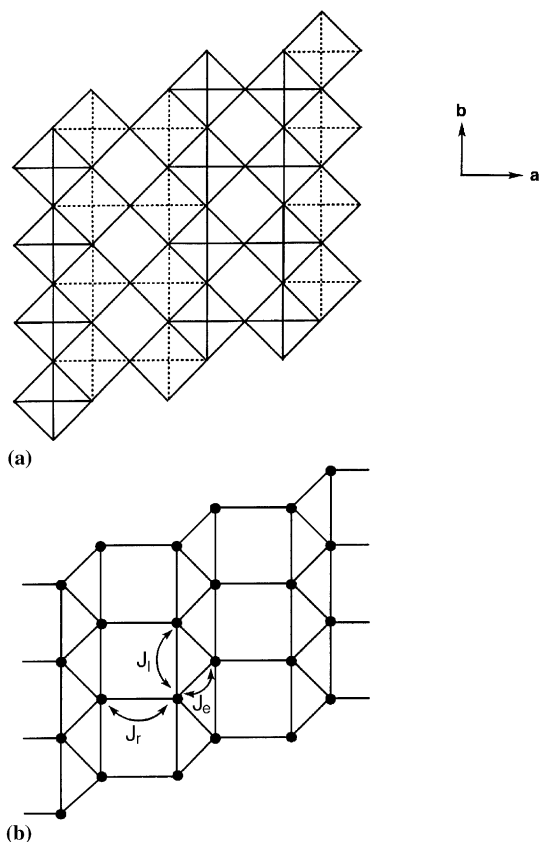
(a)

(b)

Fig. 54. (a) Schematic view of the V_2O_5 layer of AV_2O_5 ($A = Na, Ca, Mg$). (b) Arrangement of the vanadium atoms in the V_2O_5 layer of AV_2O_5 ($A = Na, Ca, Mg$).

Fig. 55. (a–c) Spin dimers of the V_2O_5 layers in CaV_2O_5 and MgV_2O_5. (d, e) Spin dimers of the V_2O_5 layers in α'-NaV_2O_5. (a) Corner-sharing V_2O_9 defining the rung of the ladder chain. (b) Corner-sharing V_2O_9 along the legs of the ladder chain. (c) Edge-sharing V_2O_8 between two adjacent ladder chains. (d) $(V_4O_{20})^{22-}$ spin dimer describing the interaction between two adjacent rungs within a ladder chain. (e) $(V_4O_{22})^{26-}$ spin dimer describing the interaction between two adjacent rungs between neighboring ladder chains.
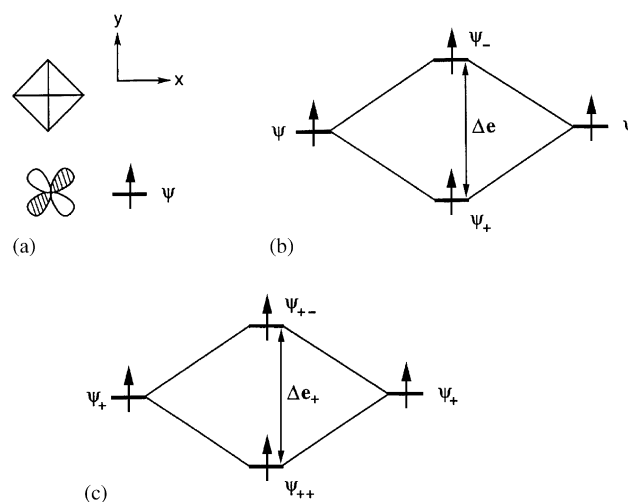
Fig. 56. (a) Magnetic orbital of a spin monomer in CaV_2O_5 and MgV_2O_5. (b) Orbital interaction diagram relevant for the spin dimers of CaV_2O_5 and MgV_2O_5. (c) Orbital interaction diagram relevant for the spin dimers of α'-NaV_2O_5.

adjacent vanadium atoms of α'-NaV_2O_5, namely, $(V_2O_9)^{9-}$ (Fig. 55a and b) and $(V_2O_8)^{7-}$ (Fig. 55c), the ψ_+ level is singly occupied and the ψ_- level is empty so that one of these spin dimers should act as a spin monomer. The energy split between ψ_+ and ψ_- is largest for the corner-sharing spin dimer shown in Fig. 55a (i.e., the rung). Consequently, each rung of the ladder chains is a spin monomer in α'-NaV_2O_5. Thus in discussing the spin exchange interactions in α'-NaV_2O_5, it is necessary to consider only two spin dimers. One is the $(V_4O_{20})^{22-}$ spin dimer (Fig. 55d) for the intraladder interaction, and the other is the $(V_4O_{22})^{26-}$ spin dimer (Fig. 55e) for the interladder interaction. In each of these spin dimers, the two spin orbitals ψ_+ interact to form bonding and antibonding levels ψ_{++} and ψ_{+-}, respectively, as depicted in Fig. 56c. The energy separation Δe_+ between the ψ_{++} and ψ_{+-} levels is the spin orbital interaction energy $\Delta\varepsilon$ needed to discuss the spin exchange interactions in α'-NaV_2O_5. The Δe_+ values calculated for the intra- and interladder interactions are 190 and 10 meV, respectively. Namely, the spin exchange interaction between the rungs is stronger within each ladder than that between adjacent ladder chains by a factor of 360. Thus the spin exchange interactions in α'-NaV_2O_5 are highly 1D along the ladder direction. This explains why
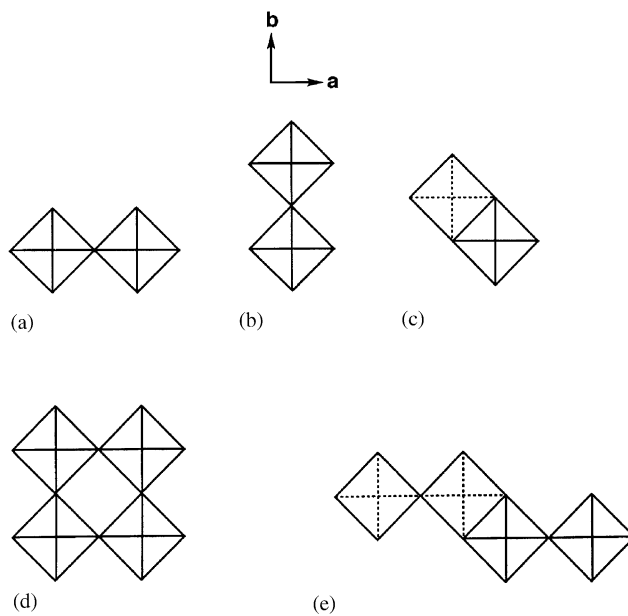
the magnetic susceptibility of this compound above 100 K is well described by a spin 1/2 Heisenberg chain.

Finally, we discuss the spin exchange interactions of CaV_2O_5 and MgV_2O_5. The values of J_r, J_l and J_e determined experimentally [167,171] and theoretically [51] are summarized in Table 19. As for CaV_2O_5, both the first principles study of Korotin et al. [51] and the

Table 19
Experimental and calculated spin exchange parameters (in K/k_B) of CaV_2O_5 and MgV_2O_5

	CaV_2O_5			MgV_2O_5		
	J_r	J_l	J_e	J_r	J_l	J_e
(a) Experimental fitting						
Ueda [167]	−730	−587	−170	−511	−565	−201
Miyahara et al. [171][a]	−670	−67	−45			
Miyahara et al. [171][b]	−665	−135	+25			
(b) Theoretical studies						
LDA + U [51]	−608	−122	+28	−92	−144	−60
$−(\Delta\varepsilon)^2$[c]	−1.00	−0.38	−0.08	−0.29	−0.45	−0.21

[a] Result of the fitting under the constraint of $J_l/J_r = 0.1$.
[b] Result of the fitting under the constraint of $J_l/J_r = 0.2$.
[c] Relative $−(\Delta\varepsilon)^2$ values with respect to the largest value, i.e., $50,600\,(meV)^2$, as the reference.

present EHTB study show that the extent of antiferromagnetic interaction in the three exchange paths decrease in the order, $J_r \gg J_l, \gg J_e$. Thus, CaV_2O_5 is better described as a weakly coupled-dimer system rather than as a ladder system. This result is in agreement with the analysis of Miyahara et al. [171] but not with that of Ueda [167]. Miyahara et al. pointed out [171] that the experimental fitting analysis is affected by the presence impurity phase in the sample. As for MgV_2O_5, the first principles study of Korotin et al. [51] and the present EHTB study show that J_l is the strongest spin exchange path. In addition, both studies produce similar J_r/J_l and J_e/J_l ratios. Since the J_e/J_l ratio (i.e., ~ 0.4) is not negligible compared with the J_r/J_l ratio (i.e., ~ 0.6), MgV_2O_5 cannot be regarded a ladder system. As pointed out earlier [170], the spin exchange interaction of the rung is much weaker in MgV_2O_5 than in CaV_2O_5 because the V–O–V bridge of the rung has a longer V–O bond in MgV_2O_5 than in CaV_2O_5.

In terms of the topological arrangements of their vanadium atoms, the V_2O_5 layers of the three oxides α'-NaV_2O_5, CaV_2O_5 and MgV_2O_5 can be described as constructed from two-leg ladders (Fig. 54b). In terms of the relative strengths of the spin exchange interactions, however, none of these three compounds belongs to a spin ladder system. A similar situation is found for molecular crystals possessing ladder-like arrangements of spin-carrying molecular units, which have been discussed in terms of spin ladders [172–177]. However, a structural ladder is not necessarily a spin ladder in terms of spin exchange interaction because the overlap between magnetic orbitals is not isotropic. Our spin dimer analyses show that many of the molecular solids with ladder-like structural arrangements are not spin ladder systems [178].

7.8. Long range magnetic ordering in paramelaconite Cu_4O_3 and cupric oxide CuO

7.8.1. Paramelaconite Cu_4O_3

Paramelaconite Cu_4O_3 is a mineral with interesting magnetic properties [179]. The Cu_2O_3 lattice of spin-1/2 Cu^{2+} ions results from Cu_4O_3 when the diamagnetic Cu^+ ions are removed (Fig. 57). The building blocks of the Cu_2O_3 lattice are the CuO_2 ribbon chains that are made up of edge-sharing CuO_4 square planes. A neutron diffraction study [180] reveals that Cu_4O_3 undergoes a magnetic phase transition below 42.3 K leading to a supercell $(2a, 2b, 2c)$, namely, the phase transition doubles the unit cell along each crystallographic direction [180]. The magnetic susceptibility shows a maximum around 75 K and a sharp decrease below 42.3 K [180], which suggest an antiferromagnetic phase transition. $Ag_2Cu_2O_3$ is isostructural and isoelectronic with Cu_4O_3 [181–183]. The structure of $Ag_2Cu_2O_3$ results when the Cu^+ ions of Cu_4O_3 are replaced with Ag^+ ions, i.e., $Ag_2Cu_2O_3$ has the same Cu_2O_3 spin lattice as found for Cu_4O_3. The magnetic susceptibility of $Ag_2Cu_2O_3$ shows a broad maximum at ~ 80 K [182,183] and a sharp decrease below 60 K [182], which again suggest an antiferromagnetic phase transition. So far no study has been reported concerning the magnetic structure of $Ag_2Cu_2O_3$ below 60 K.

The magnetic structures of Cu_4O_3 and $Ag_2Cu_2O_3$ raise important questions. Each CuO_2 ribbon chain has two spin-1/2 Cu^{2+} ions per unit cell (Fig. 57b) so that an antiferromagnetic ordering such as $(\uparrow\downarrow)_\infty$ along each chain does not double the unit cell along the a- and b-direction. A unit cell of the Cu_2O_3 lattice has four layers of CuO_2 ribbon chains (parallel to the ab-plane) (Fig. 57b). Thus, an antiferromagnetic ordering such as $(\uparrow\downarrow\uparrow\downarrow)_\infty$ in the successive layers of CuO_2 ribbon chains does not double the unit cell along the
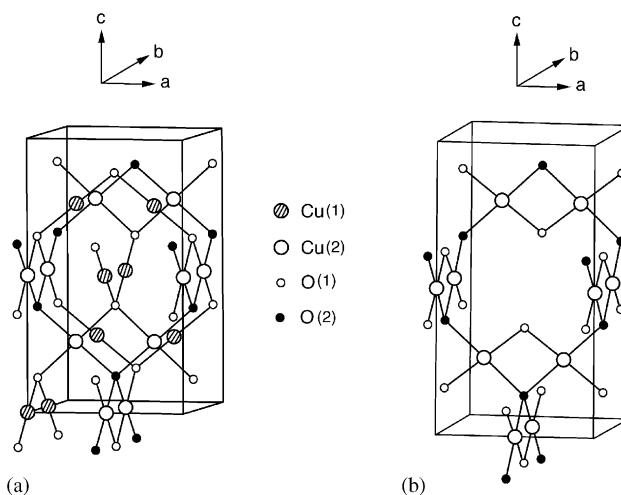

Fig. 57. (a) Perspective view of the crystal structure of Cu_4O_3. (b) Perspective view of the Cu_2O_3 spin lattice of Cu_4O_3.

c-direction. It was examined [79] recently what kind of spin ordering takes place in the Cu_2O_3 lattice below 42.3 K to double the unit cell along each crystallographic direction

Each CuO_4 square plane is a spin monomer of the Cu_2O_3 lattice, in which layers of CuO_2 ribbon chains parallel to the *a*-direction alternate with layers of CuO_2 ribbon chains parallel to the *b*-direction (Fig. 57b). In each layer of CuO_2 ribbon chains the plane of each ribbon chain is perpendicular to the layer. The ribbon chains between adjacent layers are condensed by sharing their O(2) atoms such that each O(2) atom is located at the center of the Cu_4 tetrahedron made up of the four surrounding Cu(2) atoms. There are two kinds of Cu–O–Cu superexchange paths to consider in the Cu_2O_3 lattice, i.e., the intra- and interchain Cu–O–Cu paths. The interchain Cu–O–Cu paths have a significantly larger $\angle$ Cu–O–Cu angle than do the intrachain Cu–O–Cu paths (see below), so the interchain Cu–O–Cu paths provide a stronger antiferromagnetic interaction (Table 20). In each CuO_4 square plane, two O(1) atoms are located at diagonally opposite corners, and two O(2) atoms occupy the remaining corners (Fig. 57b). Thus, the O(1) and O(2) atoms alternate on one edge of each CuO_2 ribbon chain, but the O(2) and O(1) atoms do on the opposite edge. This structural feature of opposite senses of O(1) and O(2) alternation plays a vital role in the spin ordering along the *c*-direction.

Table 20 reveals that the interchain SE interaction is more strongly antiferromagnetic than the intrachain SE interaction because the SE path Cu–O–Cu has a significantly larger $\angle$ Cu–O–Cu angle in the interchain than in the intrachain NN interaction (i.e., 114.8° vs. 95.8° in Cu_4O_3, and 116.9° vs. 104.8° in $Ag_2Cu_2O_3$). Each O(2) atom is the common bridging point of four interchain Cu–O–Cu superexchange paths (Fig. 57b). Fig. 58a shows the most favorable arrangement of four Cu^{2+} spins surrounding a single O(2) atom, which occurs between two adjacent CuO_2 ribbon chains. This spin arrangement around O(2) will be referred to as the ↑↑/↓↓ arrangement. The most energetically favorable arrangement between two adjacent layers of CuO_2 ribbon chains is presented in Fig. 58b, where every

shared O(2) atom the ↑↑/↓↓ arrangement. As a consequence, each CuO_2 ribbon chain adopts the (↑↑↓↓)$_\infty$ spin arrangement (Fig. 58c) hence doubling its repeat distance. Therefore, the unit cell of Cu_4O_3 is doubled along the *a*- and *b*-directions. For convenience, the two layers of CuO_2 ribbon chains of Fig. 58b may be referred to as a ↑↑/↓↓-double-layer.

To consider the spin ordering along the *c*-direction, it should be recalled that the O(1) and O(2) atom alternations on the two edges of a CuO_2 ribbon chain have opposite senses (Fig. 57b). Suppose that another layer of CuO_2 ribbon chains is condensed to a ↑↑/↓↓-double-layer in which each shared O(2) atom has the ↑↑/↓↓ arrangement. Each O(2) atom joining two such layers can have either the ↑↓/↑↓ or ↑↓/↓↑ spin arrangement shown in Fig. 59a. These two arrangements are energetically equivalent. Consequently, the new set of shared O(2) atoms generated by the additional layer can adopt either the spin arrangement of Fig. 59b or that of Fig. 59c, because the two interchain spin arrangements ↑↓/↑↓ and ↑↓/↓↑ available for the O(2) atoms are the same in energy. It is convenient to describe the spin ordering of the Cu_2O_3 lattice along the *c*-direction in terms of stacking ↑↑/↓↓-double-layers. The stacking between two ↑↑/↓↓-double-layers can be achieved by adopting the ↑↓/↑↓ or ↑↓/↓↑ spin arrangement between them. Thus there occur two stacking patterns between adjacent ↑↑/↓↓-double-layers, which we may refer to as the α and β arrangements. Then the stacking of ↑↑/↓↓-double-layers can give rise a large number of repeat patterns.
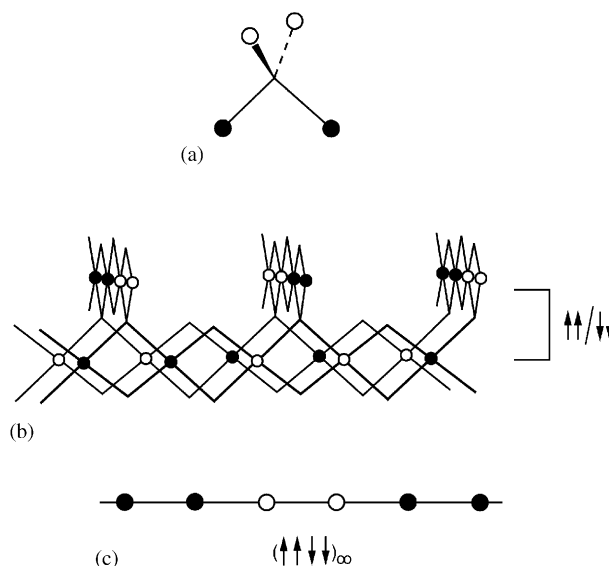
Fig. 58. (a) Most favorable spin arrangement of four Cu^{2+} ions around a shared O(2) atom between adjacent CuO_2 ribbon chains. (b) Most favorable interchain spin arrangement between adjacent layers of CuO_2 ribbon chains. (c) (↑↑↓↓)$_\infty$ arrangement of spins in a CuO_2 ribbon chain. Filled and empty circles represent the Cu^{2+} ions with up- and down-spins, respectively.

Table 20
$\Delta\varepsilon$ and *J* values calculated for the intrachain and interchain SE interactions of the Cu_2O_3 lattices in Cu_4O_3 and $Ag_2Cu_2O_3$[a]

Interaction	Cu_4O_3[b]		$Ag_2Cu_2O_3$[c]	
	$\Delta\varepsilon$ (meV)	J/k_B (K)	$\Delta\varepsilon$ (meV)	J/k_B (K)
Intrachain	51	−17.4	42	−11.8
Interchain	85	−48.3	91	−55.4

[a] The *J* values were calculated using the expression $J = -\langle (\Delta\varepsilon)^2 \rangle / U_{eff}$ with $U_{eff} = 1.74$ eV.
[b] Calculated using the crystal structure of Ref. [179].
[c] Calculated using the crystal structure of Ref. [182].

Fig. 59. (a) $\uparrow\downarrow/\uparrow\downarrow$ and $\uparrow\downarrow/\downarrow\uparrow$ arrangements of spins around each O(2) atom. (b, c) Two equivalent interchain spin arrangements that can be used for the stacking between two $\uparrow\uparrow/\downarrow\downarrow$-double-layers. Filled and empty circles represent the Cu^{2+} ions with up- and down-spins, respectively.

Fig. 60. Stacking arrangement $(\alpha\beta\beta\alpha)_\infty$ in the Cu_2O_3 lattice that doubles the unit cell along the a-, b- and c-dire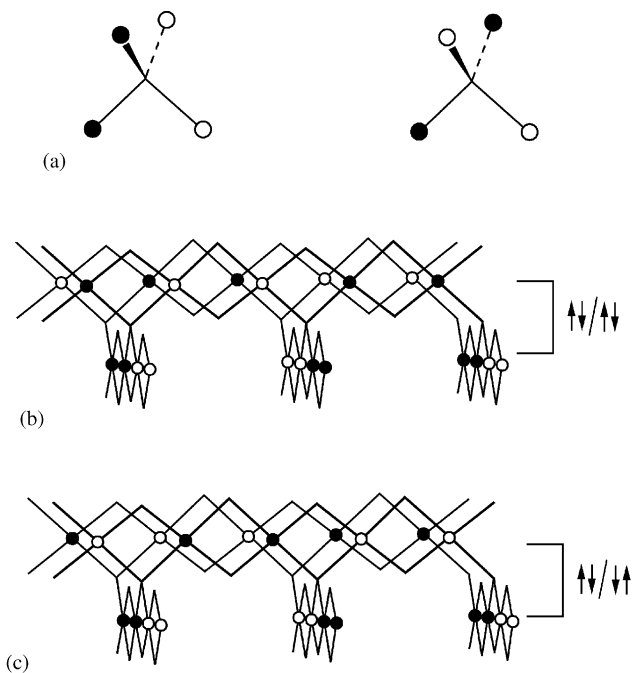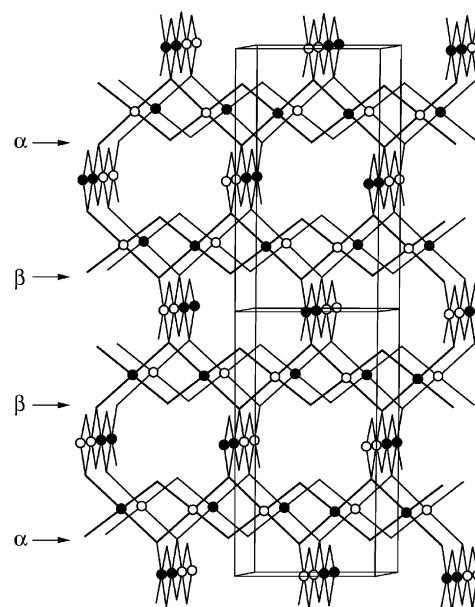ctions. Filled and empty circles represent the Cu^{2+} ions with up- and down-spins, respectively. Each rectangular box represents a unit cell in the absence of the magnetic phase transition.

The patterns such as $(\alpha\alpha)_\infty$ and $(\alpha\beta)_\infty$ do not double the unit cell along the c-direction, while the patterns such as $(\alpha\beta\alpha\alpha)_\infty$, $(\alpha\alpha\beta\alpha)_\infty$, $(\alpha\alpha\alpha\beta)_\infty$, $(\alpha\beta\beta\alpha)_\infty$, and $(\alpha\alpha\beta\beta)_\infty$ do. As an example, Fig. 60 depicts the repeat pattern $(\alpha\beta\beta\alpha)_\infty$. In principle, the unit cell along the c-direction can be increased by a factor of any integer $n \geqslant 2$. Therefore, the experimental observation of the c-axis doubling means that the spin orderings such as $(\alpha\beta\beta\alpha)_\infty$, $(\alpha\alpha\beta\beta)_\infty$, $(\beta\alpha\alpha\beta)_\infty$ and $(\beta\beta\alpha\alpha)_\infty$ are statistically the most probable arrangements, given the fact that the spin arrangements $\uparrow\downarrow/\uparrow\downarrow$ and $\uparrow\downarrow/\downarrow\uparrow$ are equally valid for the stacking between $\uparrow\uparrow/\downarrow\downarrow$-double-layers.

The above discussion of spin ordering along the c-direction leads to two important implications. First, the freedom of choice between the $\uparrow\downarrow/\uparrow\downarrow$ and $\uparrow\downarrow/\downarrow\uparrow$ arrangements for the stacking between $\uparrow\uparrow/\downarrow\downarrow$-double-layers should give rise to spin fluctuation in the Cu_2O_3 spin lattice, and the extent of this spin fluctuation should depend on temperature. Second, the ordered spin arrangements of the Cu_2O_3 lattice that explain the observed superlattice formation differ from conventional antiferromagnetic ordering. Table 20 reveals that the spin exchange parameters J calculated for $Ag_2Cu_2O_3$ are very similar to those calculated for Cu_4O_3. Thus it is expected that the magnetic phase transition of $Ag_2Cu_2O_3$ at 60 K should double the unit cell along each crystallographic direction, and the Cu_2O_3 lattice of $Ag_2Cu_2O_3$ should exhibit spin fluctuation.

7.8.2. Cupric oxide CuO

The magnetic properties of cupric oxide CuO have been examined extensively in studies including magnetic susceptibility [184–188], neutron diffraction [189–191], neutron scattering [192], NMR [193–195] and specific heat measurements [196]. The structural building blocks of cupric oxide are CuO_2 ribbon chains, and the 3D lattice of CuO is constructed from these CuO_2 chains by oxygen corner-sharing (Fig. 61a) [197]. The ribbon planes of every two CuO_2 chains condensed by corner-sharing are not perpendicular to each other (Fig. 61b). Thus each Cu^{2+} site is connected to its 10 adjacent Cu^{2+} sites by four kinds of Cu–O–Cu superexchange paths [i.e., Cu(1)–O–Cu(2), Cu(1)–O–Cu(3), Cu(1)–O–Cu(4) and Cu(1)–O–Cu(5)] (Fig. 61c). Each Cu^{2+} ion is surrounded by two additional Cu^{2+} ions unconnected by a Cu–O–Cu superexchange path (Fig. 61a). The 12 Cu^{2+} ions around each Cu^{2+} ion are grouped into six pairs related by inversion symmetry.

As the temperature is increased above $T_{N1} = 231$ K, the magnetic susceptibility of CuO does not decrease according to the Curie–Weiss law, but increases, passes through a wide maximum at 540 K and then diminishes [184]. Thus, CuO behaves as 1D antiferromagnetic chains above T_{N1}. Below $T_{N1} = 231$ K, CuO becomes a 1D collinear antiferromagnet with a magnetic moment $0.68 \, \mu_B$ per Cu^{2+} ion [189,192], which is considerably smaller than the pure spin value $1 \, \mu_B$. CuO undergoes a phase transition below T_{N1} to form an incommensurate antiferromagnetic structure with propagation vector $(0.506, 0, -0.483)$. Below $T_{N2} = 212.5$ K the latter is
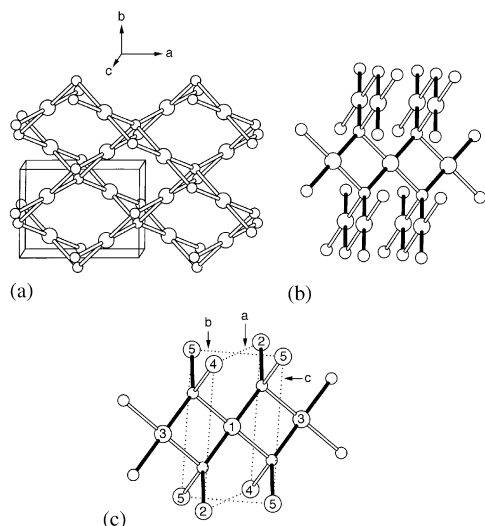
Fig. 61. (a) Perspective view of corner-sharing CuO_2 ribbon chains in cupric oxide CuO. (b) Zoomed-in view of corner-sharing CuO_2 ribbon chains. (c) Zoomed-in view of a CuO_2 ribbon chain showing the unit cell vector directions. The strongly interacting Cu–O–Cu superexchange paths are presented by filled cylinders.

Table 21
Geometrical parameters and $(\Delta\varepsilon)^2$ values associated with the four superexchange paths Cu(1)–O–Cu(j) ($j = 2-5$) of CuO[a,b]

Path	Cu$\cdots$Cu	Cu–O	$\angle$ Cu–O–Cu	$-(\Delta\varepsilon)^2$	$-J_{AF}$
$j = 2$	3.749	1.961, 1961	145.8	51,500	73
$j = 3$	2.901	1.961, 1.951	95.7	3360	4.8
$j = 4$	3.173	1.951, 1.951	108.9	1160	1.6
$j = 5$	3.083	1.951, 1.961	104.0	360	0.5

[a] The distances in Å units, and the angles in degrees.
[b] The $(\Delta\varepsilon)^2$ values are in units of (meV)^2, and the $-J_{AF}$ values in units of meV.

The $(\Delta\varepsilon)^2$ values calculated for the four superexchange interactions of CuO are listed in Table 21, where the corresponding J_{AF} values were calculated using $U_{eff} = 705$ meV. This U_{eff} value reproduces the J value of –73 meV for the 1D antiferromagnetic chain made up of the Cu(1)–O–Cu(2) paths. As expected, the antiferromagnetic exchange interaction through the Cu(1)–O–Cu(2) path is by far the strongest. The second strongest antiferromagnetic exchange interaction occurs through the Cu(1)–O–Cu(3) paths. The remaining two superexchange paths Cu(1)–O–Cu(4) and Cu(1)–O–Cu(5) provide much weaker antiferromagnetic interactions. It is noted that the Cu(1)–O–Cu(3) path has a smaller $\angle$ Cu–O–Cu angle than do the Cu(1)–O–Cu(4) and Cu(1)–O–Cu(5) (i.e., 95.7° vs. 108.9° and 104.0°), but provides a stronger antiferromagnetic interaction. The Cu(1) and Cu(3) atoms are connected by two Cu–O–Cu bridges. In contrast, the Cu(1) and Cu(4) atoms are connected by a single Cu–O–Cu bridge, and so are the Cu(1) and Cu(5) atoms.

It is important to probe what possible commensurate magnetic superstructures of CuO result from ordering of 1D antiferromagnetic chains. For simplicity, we limit our discussion to those orderings that either keep the chemical unit cell (a, b, c) or double the unit cell along the a-, b- or c-direction. With this restriction, there are only eight different ways of ordering the 1D antiferromagnetic chains surrounding a given 1D antiferromagnetic chain (Fig. 62). The two spin arrangements of Fig. 62a retain the chemical unit cell. The three Cu(1)–O–Cu(j) ($j = 3-5$) superexchange interactions, which control the interactions between the 1D antiferromagnetic chains, are weak. Thus, one might speculate that the three interchain superexchange interactions can be either weakly ferromagnetic or weakly antiferromagnetic. Then all the eight possible spin arrangements of Fig. 62 are equally probable. This leads to the prediction that at temperatures below T_{N2}, a unit doubling should be observed not only along the a- and c-directions due to the spin arrangements of Fig. 62b and d, but also along the b-direction due to the spin arrangements of Fig. 62b and c. The latter prediction is inconsistent with the results of the available

transformed into a commensurate antiferromagnetic structure with propagation vector (0.5, 0, −0.5) [189,192]. Thus, the magnetic phase transition below T_{N2} doubles the unit cell along the a- and c-directions. The strongest antiferromagnetic interactions between the adjacent Cu^{2+} ions of CuO occur along the $[10\bar{1}]$ direction through the superexchange paths having the largest $\angle$ Cu–O–Cu angle (145.8°), i.e., Cu(1)–O–Cu(2). (In Fig. 61b and c, the Cu–O bonds representing these paths are indicated by filled cylinders.) The spin exchange parameter $|J|$ for these 1D antiferromagnetic chains was estimated to be 67 ± 20 meV from the spin-wave velocity $v = |J|d = 250 \pm 75$ using the distance d between the nearest neighbor Cu^{2+} ions along the $[1\,0\,\bar{1}]$ direction (i.e., 3.75 Å) [192]. This agrees well with the value of 73 meV [195] estimated from the relationship $|J| = 1.560 \, k_B T_{max}$ for the magnetic susceptibility of a 1D antiferromagnetic Heisenberg chain using $T_{max} = 540$ K [184], where T_{max} is the temperature at which the magnetic susceptibility is maximum.

The spin exchange interactions between the 1D antiferromagnetic chains of CuO have been regarded as weak because the associated $\angle$ Cu–O–Cu angles are much closer to 90° than to 180° (Table 21). To a first approximation, therefore, the incommensurate and commensurate magnetic superstructures of CuO are ordered structures of the 1D antiferromagnetic chains. Recently, we examined [198] whether an ordering of the 1D antiferromagnetic chains gives rise to other magnetic superstructures equally probable as the $(2a, 0, 2c)$ superstructure and whether the interactions between the 1D antiferromagnetic chains possess any energetic or statistical factor favoring the $(2a, 0, 2c)$ superstructure.

(a, b, c)

(a)

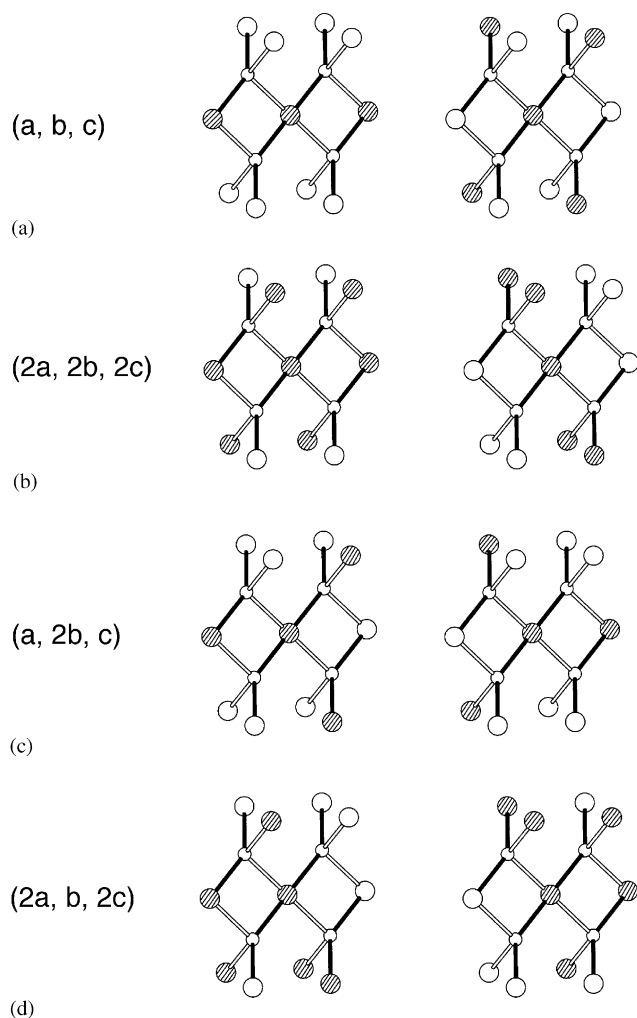(2a, 2b, 2c)

(b)

(a, 2b, c)

(c)

(2a, b, 2c)

(d)

Fig. 62. Eight possible spin arrangements in the 10 Cu^{2+} ions connected, by superexchange paths, to a given Cu^{2+} ion. The up-spin and down-spin Cu^{2+} sites are indicated by shaded and unshaded circles, respectively. For convenience, the central Cu^{2+} ion is assumed to have an up-spin. These arrangements retain the chemical unit cell $(a–c)$ in (a). However, they lead to a $(2a, 2b, 2c)$ supercell in (b), a $(a, 2b, c)$ supercell in (c), and a $(2a, b, 2c)$ supercell in (d).

experiments [189–192]. Consequently, it is necessary to consider that there exists an energetic factor favoring the spin arrangements of Fig. 62d over those of Fig. 62b and c.

Table 22 summarizes the nature of the long-range spin ordering along the directions of the Cu(1)–O–Cu(2), Cu(1)–O–Cu(3), Cu(1)–O–Cu(4) and Cu(1)–O–Cu(5) spin exchange paths in the ordered magnetic structures that result from the eight spin arrangements of Fig. 62. From the consideration of these long range spin orders, it is not clear why CuO prefers the ordered spin structures leading to the $(2a, b, 2c)$ supercell over the other ordered spin structures. Thus we analyze the local spin distributions around each spin site. As already pointed out, each Cu^{2+} ion is surrounded by 12 nearest-neighbor Cu^{2+} ions grouped into six pairs of Cu^{2+} ions

Table 22
Nature of the spin ordering along the Cu(1)−O−Cu(j) (j = 2−5) spin exchange paths in cupric oxide CuO

Superstructure[a]	Cu(1)−O−Cu(j)[a]			
	j = 2	j = 3	j = 4	j = 5
(a, b, c)[b]	AFM	FM	AFM	AFM
(a, b, c)[c]	AFM	AFM	AFM	FM
$(2a, 2b, 2c)$	AFM	AFM & FM	FM	AFM & FM
$(a, 2b, c)$	AFM	$(\uparrow\uparrow\downarrow\downarrow)_\infty$	AFM	$(\uparrow\uparrow\downarrow\downarrow)_\infty$
$(2a, b, 2c)$	AFM	$(\uparrow\uparrow\downarrow\downarrow)_\infty$	FM	$(\uparrow\uparrow\downarrow\downarrow)_\infty$

[a] The Cu(1)−O−Cu(j) superexchange paths are defined in Fig. 61c. The symbols AFM and FM mean antiferromagnetic and ferromagnetic arrangements, respectively.
[b] For the first arrangement of Fig. 62a.
[c] For the second arrangement of Fig. 62a.

Table 23
Local spin distributions around Cu^{2+} ions in the ordered spin structures of CuO that result from the ordering of 1D antiferromagnetic chains

Superstructure	Spin distribution[a]	N_{CSP}[b]	N_{NCSP}[b]
(a, b, c)	$\uparrow$: $(4\uparrow, 8\downarrow)$	0	5
	$\downarrow$: $(8\uparrow, 4\downarrow)$	0	5
$(2a, 2b, 2c)$	$\uparrow$: $(6\uparrow, 6\downarrow)$	0	5
	$\downarrow$: $(6\uparrow, 6\downarrow)$	0	5
$(a, 2b, c)$	$\uparrow$: $(4\uparrow, 8\downarrow)$	4	1
	$\downarrow$: $(8\uparrow, 4\downarrow)$	4	1
$(2a, b, 2c)$	$\uparrow$: $(6\uparrow, 6\downarrow)$	4	1
	$\downarrow$: $(6\uparrow, 6\downarrow)$	4	1

[a] The notations are defined as follows: for example, $\uparrow$: $(m\uparrow, n\downarrow)$ means that the 12 spins surrounding each up-spin Cu^{2+} site divided into m up-spins and n down-spins.
[b] N_{CSP} refers to the number of compensating spin pairs, and N_{NCSP} the number of non-compensating spin pairs.

related by inversion symmetry at the central Cu^{2+} ion. The 10 nearest-neighbor Cu^{2+} ions that are not involved in making a 1D antiferromagnetic chain with the central Cu^{2+} ion lie within the narrow distance range of 2.90–3.17 Å (Fig. 61, Table 21). It is of interest to see how up-spins and down-spins are distributed among the 12 nearest-neighbor spin sites surrounding each spin site. Table 23 summarizes these local spin distributions in the ordered magnetic structures derived from the eight spin arrangements of Fig. 62. The 12 Cu^{2+} ions surrounding each Cu^{2+} ion are divided into equal numbers of up-spin and down-spin ions in the ordered spin structures leading to the $(2a, b, 2c)$ and $(2a, 2b, 2c)$ supercells, but into unequal numbers of up-spin and down-spin ions in the ordered spin structures leading to the $(a, 2b, c)$ supercell or retaining the chemical unit cell (a, b, c). Thus, in terms of the numbers of up-spin and down-spin ions around each spin site, the local spin arrangement around each Cu^{2+} ion is balanced only in the ordered spin structures leading to the $(2a, b, 2c)$ and $(2a, 2b, 2c)$ supercells.

To further distinguish the ordered spin structures possessing the unit cells (a, b, c), $(a, 2b, c)$, $(2a, b, 2c)$ and $(2a, 2b, 2c)$, we examine the nature of spin distribution in each pair of spin sites related by inversion symmetry at each Cu^{2+} site. Of the six pairs of spin sites surrounding around each spin site, one pair is used to form a 1D antiferromagnetic chain with the central Cu^{2+} ion. Thus only the spin arrangements in the remaining five pairs are important for the interchain interactions. In each of these five pairs, the two spins can be either opposite (i.e., compensating) or identical (i.e., non-compensating). The number of compensating spin pairs (N_{CSP}) and that of non-compensating spin pairs (N_{NCSP}) around each spin site in the ordered spin structures are summarized in Table 23. The spin distribution around each spin site is more balanced when N_{CSP} is larger. Thus, in terms of the number of compensating spin pairs around each spin site, the local spin arrangement around each Cu^{2+} ion is much better balanced in the ordered spin structures leading to the unit cells $(2a, b, 2c)$ and $(a, 2b, c)$ supercells than in those leading to the unit cells (a, b, c) and $(2a, 2b, 2c)$.

The above discussion reveals that the local spin arrangement around each Cu^{2+} ion is most balanced in the ordered spin structures leading to the unit cells $(2a, b, 2c)$ both in terms of the numbers of up-spins and down-spins around each spin site and in terms of the number of compensating spin pairs around each spin site. The experimental observation of the $(2a, b, 2c)$ supercell below T_{N2} leads us to conclude that such a balanced local spin distribution around a spin site with inversion symmetry is energetically favorable. If this factor is strong, it should be possible to observe weak magnetic reflection peaks corresponding to the $(a, 2b, c)$ and $(2a, 2b, 2c)$ supercells.

8. Concluding remarks

In this article we reviewed three important features of theoretical studies on the low-energy excitation energies of magnetic solids, namely, analyses of the eigenvalue structures of spin Hamiltonians, quantitative calculations of spin exchange parameters using first principles electronic structure computations, and estimations of the relative strengths of spin exchange parameters using qualitative electronic structure calculations. Details of our results concerning how antisymmetric and anisotropic interactions affect the eigenvalue structures of isotropic spin Hamiltonian are summarized in Appendix A, B, C. Our survey of the spin exchange interactions and magnetic structures of various magnetic solids reveals that the relative strengths of SE and SSE interactions can be estimated almost semiquantitatively in terms of spin dimer analysis based on EHTB calculations. The relative strengths of spin exchange

interactions deduced from this analysis led us to satisfactory explanations of the observed magnetic structures and new questions to explore experimentally. This analysis provides an expedient and reliable way to assign strongly interacting spin exchange paths and correctly interpret results of magnetic susceptibility, inelastic neutron scattering or Raman scattering measurements.

It should be emphasized that strongly interacting spin exchange paths of a magnetic solid are determined by the overlap between its magnetic orbitals. For a magnetic solid of any interest, the magnetic orbital(s) are not made up of atomic s-orbitals. Therefore, the overlap between adjacent magnetic orbitals in a magnetic solid cannot be isotropic. As a consequence, the strongly interacting spin unit of a magnetic solid does not necessarily have the same geometrical feature as the arrangement of its magnetic ions or spin-carrying molecules. Thus electronic structure considerations are essential for selecting a correct set of spin exchange paths to employ. It is anticlimactic to interpret experimental results in terms of a spin lattice model that one can readily prove to be irrelevant on the basis of simple electronic structure considerations.

Appendix A

Nonzero matrix elements $\langle S'\ \ Ms'|\hat{H}_{asym}|S\ \ Ms\rangle$ of the asymmetric Hamiltonian $\hat{H}_{asym}$ for $S_1 = S_2 = 1/2, 1, 3/2, 2$ and $5/2$.

(a) $S_1 = S_2 = 1/2$

$$\langle 0\ \ 0|\hat{H}_{asym}|1\ \ 0\rangle = -\langle 1\ \ 0|\hat{H}_{asym}|0\ \ 0\rangle$$
$$= (1/2)iD.$$

(b) $S_1 = S_2 = 1$

$$\langle 0\ \ 0|\hat{H}_{asym}|1\ \ 0\rangle = -\langle 1\ \ 0|\hat{H}_{asym}|0\ \ 0\rangle$$
$$= \sqrt{2/3}\,iD,$$

$$\langle 1\ \ 0|\hat{H}_{asym}|2\ \ 0\rangle = -\langle 2\ \ 0|\hat{H}_{asym}|1\ \ 0\rangle$$
$$= \sqrt{4/3}\,iD,$$

$\langle 1 \quad \pm 1 | \hat{H}_{\text{asym}} | 2 \quad \pm 1 \rangle$
$= -\langle 2 \quad \pm 1 | \hat{H}_{\text{asym}} | 1 \quad \pm 1 \rangle = \mathrm{i}D.$

(c) $S_1 = S_2 = 3/2$

$\langle 0 \quad 0 | \hat{H}_{\text{asym}} | 1 \quad 0 \rangle$
$= -\langle 1 \quad 0 | \hat{H}_{\text{asym}} | 0 \quad 0 \rangle = \sqrt{5/4}\,\mathrm{i}D,$

$\langle 1 \quad 0 | \hat{H}_{\text{asym}} | 2 \quad 0 \rangle$
$= -\langle 2 \quad 0 | \hat{H}_{\text{asym}} | 1 \quad 0 \rangle = \sqrt{16/5}\,\mathrm{i}D,$

$\langle 2 \quad 0 | \hat{H}_{\text{asym}} | 3 \quad 0 \rangle$
$= -\langle 3 \quad 0 | \hat{H}_{\text{asym}} | 2 \quad 0 \rangle = \sqrt{81/20}\,\mathrm{i}D,$

$\langle 1 \quad \pm 1 | \hat{H}_{asym} | 2 \quad \pm 1 \rangle$
$= -\langle 2 \quad \pm 1 | \hat{H}_{\text{asym}} | 1 \quad \pm 1 \rangle = \sqrt{12/5}\,\mathrm{i}D,$

$\langle 2 \quad \pm 1 | \hat{H}_{\text{asym}} | 3 \quad \pm 1 \rangle$
$= \langle 3 \quad \pm 1 | \hat{H}_{\text{asym}} | 2 \quad \pm 1 \rangle = \sqrt{18/5}\,\mathrm{i}D,$

$\langle 2 \quad \pm 2 | \hat{H}_{\text{asym}} | 3 \quad \pm 2 \rangle$
$= -\langle 3 \quad \pm 2 | \hat{H}_{\text{asym}} | 2 \quad \pm 2 \rangle = (3/2)\mathrm{i}D.$

(d) $S_1 = S_2 = 2$

$\langle 0 \quad 0 | \hat{H}_{\text{asym}} | 1 \quad 0 \rangle$
$= -\langle 1 \quad 0 | \hat{H}_{\text{asym}} | 0 \quad 0 \rangle = \sqrt{2}\,\mathrm{i}D,$

$\langle 1 \quad 0 | \hat{H}_{\text{asym}} | 2 \quad 0 \rangle$
$= -\langle 2 \quad 0 | \hat{H}_{\text{asym}} | 1 \quad 0 \rangle = \sqrt{28/5}\,\mathrm{i}D,$

$\langle 2 \quad 0 | \hat{H}_{\text{asym}} | 3 \quad 0 \rangle$
$= -\langle 3 \quad 0 | \hat{H}_{\text{asym}} | 2 \quad 0 \rangle = \sqrt{324/35}\,\mathrm{i}D,$

$\langle 3 \quad 0 | \hat{H}_{\text{asym}} | 4 \quad 0 \rangle$
$= -\langle 4 \quad 0 | \hat{H}_{\text{asym}} | 3 \quad 0 \rangle = \sqrt{64/7}\,\mathrm{i}D,$

$\langle 1 \quad \pm 1 | \hat{H}_{\text{asym}} | 2 \quad \pm 1 \rangle$
$= -\langle 2 \quad \pm 1 | \hat{H}_{\text{asym}} | 1 \quad \pm 1 \rangle = \sqrt{147/35}\,\mathrm{i}D,$

$\langle 2 \quad \pm 1 | \hat{H}_{\text{asym}} | 3 \quad \pm 1 \rangle$
$= -\langle 3 \quad \pm 1 | \hat{H}_{\text{asym}} | 2 \quad \pm 1 \rangle = \sqrt{288/35}\,\mathrm{i}D,$

$\langle 3 \quad \pm 1 | \hat{H}_{\text{asym}} | 4 \quad \pm 1 \rangle$
$= -\langle 4 \quad \pm 1 | \hat{H}_{\text{asym}} | 3 \quad \pm 1 \rangle = \sqrt{60/7}\,\mathrm{i}D,$

$\langle 2 \quad \pm 2 | \hat{H}_{\text{asym}} | 3 \quad \pm 2 \rangle$
$= -\langle 3 \quad \pm 2 | \hat{H}_{\text{asym}} | 2 \quad \pm 2 \rangle = \sqrt{36/7}\,\mathrm{i}D,$

$\langle 3 \quad \pm 2 | \hat{H}_{\text{asym}} | 4 \quad \pm 2 \rangle$
$= -\langle 4 \quad \pm 2 | \hat{H}_{\text{asym}} | 3 \quad \pm 2 \rangle = \sqrt{48/7}\,\mathrm{i}D,$

$\langle 3 \quad \pm 3 | \hat{H}_{\text{asym}} | 4 \quad \pm 3 \rangle$
$= -\langle 4 \quad \pm 3 | \hat{H}_{\text{asym}} | 3 \quad \pm 3 \rangle = 2\mathrm{i}D.$

(e) $S_1 = S_2 = 5/2$

$\langle 0 \quad 0 | \hat{H}_{\text{asym}} | 1 \quad 0 \rangle$
$= -\langle 1 \quad 0 | \hat{H}_{\text{asym}} | 0 \quad 0 \rangle = \sqrt{35/12}\,\mathrm{i}D,$

$\langle 1 \quad 0 | \hat{H}_{\text{asym}} | 2 \quad 0 \rangle$
$= -\langle 2 \quad 0 | \hat{H}_{\text{asym}} | 1 \quad 0 \rangle = \sqrt{128/15}\,\mathrm{i}D,$

$\langle 2 \quad 0 | \hat{H}_{\text{asym}} | 3 \quad 0 \rangle$
$= -\langle 3 \quad 0 | \hat{H}_{\text{asym}} | 2 \quad 0 \rangle = \sqrt{2187/140}\,\mathrm{i}D,$

$\langle 3 \quad 0 | \hat{H}_{\text{asym}} | 4 \quad 0 \rangle$
$= -\langle 4 \quad 0 | \hat{H}_{\text{asym}} | 3 \quad 0 \rangle = \sqrt{1280/63}\,\mathrm{i}D,$

$\langle 4 \quad 0 | \hat{H}_{\text{asym}} | 5 \quad 0 \rangle$
$= -\langle 5 \quad 0 | \hat{H}_{\text{asym}} | 4 \quad 0 \rangle = (25/6)\mathrm{i}D,$

$\langle 1 \quad \pm 1 | \hat{H}_{\text{asym}} | 2 \quad \pm 1 \rangle$
$= -\langle 2 \quad \pm 1 | \hat{H}_{\text{asym}} | 1 \quad \pm 1 \rangle = \sqrt{32/5}\,\mathrm{i}D.$

$\langle 2 \quad \pm 1 | \hat{H}_{\text{asym}} | 3 \quad \pm 1 \rangle$
$= -\langle 3 \quad \pm 1 | \hat{H}_{\text{asym}} | 2 \quad \pm 1 \rangle = \sqrt{486/35}\,\mathrm{i}D.$

$\langle 3 \quad \pm 1 | \hat{H}_{\text{asym}} | 4 \quad \pm 1 \rangle$
$= -\langle 4 \quad \pm 1 | \hat{H}_{\text{asym}} | 3 \quad \pm 1 \rangle = \sqrt{400/21}\,\mathrm{i}D,$

$\langle 4 \quad \pm 1 | \hat{H}_{\text{asym}} | 5 \quad \pm 1 \rangle$
$= -\langle 5 \quad \pm 1 | \hat{H}_{\text{asym}} | 4 \quad \pm 1 \rangle = \sqrt{50/3}\,\mathrm{i}D,$

$\langle 2 \quad \pm 2 | \hat{H}_{\text{asym}} | 3 \quad \pm 2 \rangle$
$= -\langle 3 \quad \pm 2 | \hat{H}_{\text{asym}} | 2 \quad \pm 2 \rangle = \sqrt{243/28}\,\mathrm{i}D,$

$\langle 3 \quad \pm 2 | \hat{H}_{\text{asym}} | 4 \quad \pm 2 \rangle$
$= -\langle 4 \quad \pm 2 | \hat{H}_{\text{asym}} | 3 \quad \pm 2 \rangle = \sqrt{320/21}\,\mathrm{i}D,$

$\langle 4 \quad \pm 2 | \hat{H}_{\text{asym}} | 5 \quad \pm 2 \rangle$
$= -\langle 5 \quad \pm 2 | \hat{H}_{\text{asym}} | 4 \quad \pm 2 \rangle = \sqrt{175/12}\,\mathrm{i}D,$

$\langle 3 \quad \pm 3 | \hat{H}_{\text{asym}} | 4 \quad \pm 3 \rangle$
$= -\langle 4 \quad \pm 3 | \hat{H}_{\text{asym}} | 3 \quad \pm 3 \rangle = \sqrt{80/9}\,\mathrm{i}D,$

$\langle 4 \quad \pm 3 | \hat{H}_{\text{asym}} | 5 \quad \pm 3 \rangle$
$= \langle 5 \quad \pm 3 | \hat{H}_{\text{asym}} | 4 \quad \pm 3 \rangle = (10/3)\mathrm{i}D,$

$\langle 4 \quad \pm 4 | \hat{H}_{\text{asym}} | 5 \quad \pm 4 \rangle$
$= -\langle 5 \quad \pm 4 | \hat{H}_{\text{asym}} | 4 \quad \pm 4 \rangle = (5/2)\mathrm{i}D.$

Appendix B

Eigenvalues of the Hamiltonian $\hat{H}_{\text{iso/asym}} = \hat{H}_{\text{HDVV}} + \hat{H}_{\text{asym}}$ as a function of the ratio $x = |D/J|$ for $S_1 = S_2 = 1/2, 1, 3/2, 2$ and $5/2$.

(a) $S_1 = S_2 = 1/2$

$$E(0 \quad 0) = J(1/4 + 1/2\sqrt{1 + x^2}),$$

$$E(1 \quad 0) = J\left(1/4 - 1/2\sqrt{1 + x^2}\right),$$

$$E(1 \pm 1) = J(-1/4).$$

(b) $S_1 = S_2 = 1$

$$E(0 \quad 0) = J\left(1 + \sqrt{9 + 8x^2}\right)/2,$$

$$E(1 \quad 0) = J,$$

$$E(2 \quad 0) = J\left(1 - \sqrt{9 + 8x^2}\right)/2,$$

$$E(1 \pm 1) = J\sqrt{1 + x^2},$$

$$E(2 \pm 1) = -J\sqrt{1 + x^2},$$

$$E(2 \pm 2) = -J.$$

(c) $S_1 = S_2 = 3/2$ (Table 24).

$$E(1 \pm 1) = J\left(1/4 + 1/2\sqrt{25 + 24x^2}\right),$$

$$E(2 \pm 1) = J(3/4),$$

$$E(3 \pm 1) = J\left(1/4 - 1/2\sqrt{25 + 24x^2}\right),$$

$$E(2 \pm 2) = J\left(-3/4 + 3/2\sqrt{1 + x^2}\right),$$

$$E(3 \pm 2) = J\left(-3/4 - 3/2\sqrt{1 + x^2}\right),$$

$$E(3 \pm 3) = -(9/4)J.$$

(d) $S_1 = S_2 = 2$ (Table 25)

$$E(3 \quad 0) = -E(1 \quad 0) + 5J,$$

$$E(2 \pm 2) = J\left(-1 + \sqrt{49 - 48x^2}\right)/2,$$

$$E(3 \pm 2) = 0,$$

$$E(4 \pm 2) = J\left(-1 - \sqrt{49 - 48x^2}\right)/2,$$

$$E(3 \pm 3) = 2J\left(-1 + \sqrt{1 + x^2}\right),$$

$$E(4 \pm 3) = 2J\left(-1 - \sqrt{1 + x^2}\right),$$

$$E(4 \pm 4) = -4J.$$

Table 24

x	0–0.5	0.5–1.0	1.0–1.5	1.5–2.0
$E(0 \quad 0)$				
c_0	3.7500	3.7502	3.7592	3.8090
c_1	1.2500	1.2480	1.2159	1.1294
c_2	−0.2291	−0.2216	−0.1770	−0.1193
c_3	0.0725	0.0590	0.0302	0.0126
c_4	−0.0200	−0.0100	−0.0027	−0.0006
sd	3.06×10^{-6}	8.79×10^{-6}	7.20×10^{-5}	4.62×10^{-3}
$E(1 \quad 0)$				
c_0	2.7500	2.7501	2.7532	2.7674
c_1	0.3500	0.3489	0.3378	0.3129
c_2	−0.0694	−0.0650	−0.0491	−0.0324
c_3	0.0278	0.0191	0.0085	0.0034
c_4	−0.0108	−0.0036	−0.0008	−0.0002
sd	1.39×10^{-6}	2.83×10^{-5}	3.37×10^{-4}	3.76×10^{-3}
$E(2 \quad 0)$				
c_0	0.7500	0.7503	0.7541	0.7559
c_1	−0.2500	−0.2534	−0.2684	−0.2727
c_2	−0.0205	−0.0058	0.0177	0.0214
c_3	0.0479	0.0168	−0.0005	−0.0018
c_4	−0.0333	−0.0050	−0.0001	0.0001
sd	1.04×10^{-6}	2.72×10^{-5}	2.12×10^{-4}	3.20×10^{-3}
$E(3 \quad 0)$				
c_0	−2.2500	−2.2506	−2.2665	−2.3323
c_1	−1.3500	−1.3435	−1.2852	−1.1695
c_2	0.3191	0.2924	0.2084	0.1303
c_3	−0.1482	−0.0949	−0.0383	−0.0142
c_4	0.0642	0.0186	0.0036	0.0007
sd	2.99×10^{-6}	1.49×10^{-5}	7.80×10^{-5}	3.77×10^{-3}

(e) $S_1 = S_2 = 5/2$ (Table 26)

$$E(4 \pm 1) = -E(2 \pm 1) + 4.5J,$$

$$E(3 \pm 3) = J\left(-7/4 + \sqrt{81 + 80x^2}/2\right),$$

$$E(4 \pm 3) = J(-5/4),$$

$$E(5 \pm 3) = J\left(-7/4 - \sqrt{81 + 80x^2}/2\right),$$

$$E(4 \pm 4) = J\left(-15/4 + 5/2\sqrt{1 + x^2}\right),$$

$$E(5 \pm 4) = J\left(-15/4 - 5/2\sqrt{1 + x^2}\right),$$

$$E(5 \pm 5) = -(25/4)J.$$

Appendix C

Nonzero matrix elements $\langle S' \quad Ms | \hat{H}_{\text{iso+aniso}} | S \quad Ms \rangle$ of the Hamiltonian $\hat{H}_{\text{iso/aniso}} = -J \, [\alpha \hat{S}_{1z} \hat{S}_{2z} + \beta(\hat{S}_{1x} \hat{S}_{2x} + \hat{S}_{1y} \hat{S}_{2y})]$ for $S_1 = S_2 = 1/2, \quad 1, \quad 3/2, \quad 2$ and $5/2$.

Table 25

x	0–0.5	0.5–1.0	1.0–1.5	1.5–2.0
$E(0\ \ 0)$				
c_0	6.0000	5.9996	6.0053	6.0723
c_1	2.0000	2.0041	1.9874	1.8729
c_2	−0.2672	−0.2859	−0.2685	−0.1934
c_3	0.0071	0.0497	0.0425	0.0201
c_4	0.0371	−0.0043	−0.0036	−0.0010
sd	3.93×10^{-6}	2.71×10^{-5}	4.00×10^{-4}	3.41×10^{-3}
$E(1\ \ 0)$				
c_0	5.0000	5.0001	5.0047	5.0302
c_1	0.8000	0.7988	0.7825	0.7832
c_2	−0.1279	−0.1231	−0.1003	−0.0708
c_3	0.0403	0.0309	0.0161	0.0072
c_4	−0.0127	−0.0052	−0.0014	−0.0004
sd	2.59×10^{-6}	3.00×10^{-5}	2.77×10^{-5}	$.91 \times 10^{-3}$
$E(2\ \ 0)$				
c_0	3.0000	3.0014	3.0234	3.0701
c_1	0.2857	0.2703	0.1855	0.1002
c_2	−0.2825	−0.2171	−0.0882	−0.0283
c_3	0.2508	0.1149	0.0233	0.0042
c_4	−0.1493	−0.0281	−0.0026	−0.0003
sd	1.50×10^{-6}	3.11×10^{-5}	3.21×10^{-4}	5.86×10^{-3}
$E(4\ \ 0)$				
c_0	−4.0000	−4.0011	−4.0287	−4.1423
c_1	−2.2857	−2.2744	−2.1729	−1.9731
c_2	0.5497	0.5030	0.3567	0.2216
c_3	−0.2579	−0.1646	−0.0659	−0.0243
c_4	0.1122	0.0324	0.0062	0.0013
sd	3.93×10^{-6}	5.80×10^{-5}	1.75×10^{-4}	3.41×10^{-3}
$E(1\pm1)$				
c_0	5.0000	5.0008	5.0238	5.1240
c_1	2.1000	2.0916	2.0079	1.8320
c_2	−0.4765	−0.4422	−0.3224	−0.2038
c_3	0.2063	0.1388	0.0586	0.0222
c_4	−0.0833	−0.0266	−0.0054	−0.0012
sd	4.91×10^{-6}	1.78×10^{-5}	4.68×10^{-4}	5.33×10^{-3}
$E(2\pm1)$				
c_0	3.0000	3.0002	3.0071	3.0367
c_1	0.6429	0.6403	0.6153	0.5632
c_2	−0.1431	−0.1324	−0.0966	−0.0615
c_3	0.0626	0.0414	0.0174	0.0067
c_4	−0.0259	−0.0080	−0.0016	−0.0003
sd	5.09×10^{-6}	4.04×10^{-5}	3.51×10^{-5}	7.19×10^{-3}
$E(3\pm1)$				
c_0	0.0000	0.0000	−0.0038	−0.0266
c_1	−0.6000	−0.5997	−0.5866	−0.5470
c_2	0.1021	0.1011	0.0834	0.0570
c_3	−0.0258	−0.0251	−0.0140	−0.0060
c_4	0.0033	0.0040	0.0012	0.0003
sd	1.15×10^{-6}	2.96×10^{-5}	4.32×10^{-4}	1.12×10^{-3}
$E(4\pm1)$				
c_0	−4.0000	−4.0010	−4.0271	−4.1341
c_1	−2.1428	−2.1322	−2.0365	−1.8483
c_2	0.5175	0.4735	0.3356	0.2083
c_3	−0.2431	−0.1551	−0.0620	−0.0229
c_4	0.1058	0.0305	0.0058	0.0012
sd	4.70×10^{-6}	3.82×10^{-5}	9.01×10^{-5}	1.04×10^{-3}

Table 26

x	0–0.5	0.5–1.0	1.0–1.5	1.5–2.0
$E(0\ \ 0)$				
c_0	8.7500	8.7480	8.7408	8.8261
c_1	2.9167	2.9386	2.9767	2.8345
c_2	−0.2127	−0.3079	−0.3822	−0.2915
c_3	−0.2109	−0.0075	0.0564	0.0301
c_4	0.2018	0.0160	−0.0044	−0.0015
sd	5.53×10^{-6}	2.35×10^{-5}	5.11×10^{-4}	1.62×10^{-3}
$E(1\ \ 0)$				
c_0	7.7500	7.7500	7.7523	7.7799
c_1	1.3500	1.3503	1.3426	1.2960
c_2	−0.1524	−0.1537	−0.1442	−0.1140
c_3	0.0220	0.0250	0.0198	0.0109
c_4	0.0004	−0.0027	−0.0015	−0.0005
sd	2.76×10^{-6}	2.57×10^{-5}	4.98×10^{-4}	4.14×10^{-3}
$E(2\ \ 0)$				
c_0	5.7500	5.7536	5.8041	5.9016
c_1	0.9404	0.9014	0.7047	0.5260
c_2	−0.6718	−0.5063	−0.2039	−0.0779
c_3	0.6110	0.2677	0.0503	0.0100
c_4	−0.3715	−0.0666	−0.0055	−0.0006
sd	1.87×10^{-6}	2.03×10^{-5}	3.66×10^{-4}	3.69×10^{-3}
$E(3\ \ 0)$				
c_0	2.7500	2.7505	2.7619	2.7924
c_1	−0.1278	−0.1335	−0.1761	−0.2314
c_2	−0.1283	−0.1048	−0.0418	−0.0033
c_3	0.1050	0.0575	0.0141	0.0019
c_4	−0.0543	−0.0134	−0.0016	−0.0001
sd	1.28×10^{-6}	8.25×10^{-5}	3.02×10^{-4}	5.36×10^{-3}
$E(4\ \ 0)$				
c_0	−1.2500	−1.2505	−1.2649	−1.3316
c_1	−1.6071	−1.6021	−1.5496	−1.4330
c_2	0.3228	0.3025	0.2277	0.1493
c_3	−0.1294	−0.0896	−0.0398	−0.0158
c_4	0.0498	0.0167	0.0036	0.0008
sd	4.10×10^{-6}	2.67×10^{-5}	9.41×10^{-5}	4.73×10^{-4}
$E(5\ \ 0)$				
c_0	−6.2500	−6.2517	−6.2942	−6.4683
c_1	−3.4722	−3.4547	−3.2984	−2.9921
c_2	0.8424	0.7701	0.5445	0.3375
c_3	−0.3978	−0.2530	−0.1008	−0.0371
c_4	0.1738	0.0499	0.0095	0.0019
sd	7.28×10^{-6}	5.55×10^{-5}	2.99×10^{-4}	5.92×10^{-3}
$E(1\pm1)$				
c_0	7.7500	7.7509	7.7817	7.9280
c_1	3.2000	3.1909	3.0797	2.8238
c_2	−0.6762	−0.6401	−0.4830	−0.3110
c_3	0.2582	0.1900	0.0863	0.0337
c_4	−0.0892	−0.0349	−0.0079	−0.0018
sd	7.19×10^{-6}	3.23×10^{-5}	2.83×10^{-4}	5.49×10^{-3}
$E(2\pm1)$				
c_0	5.7500	5.7504	5.7634	5.8241
c_1	1.4286	1.4241	1.3771	1.2709
c_2	−0.2913	−0.2734	−0.2064	−0.1351
c_3	0.1159	0.0807	0.0362	0.0144
c_4	−0.0442	−0.0150	−0.0033	−0.0007
sd	5.83×10^{-6}	9.40×10^{-5}	7.35×10^{-5}	4.77×10^{-3}

Table 26 (*continued*)

x	0–0.5	0.5–1.0	1.0–1.5	1.5–2.0
$E(3\pm1)$				
c_0	2.7500	2.7507	2.7609	2.7821
c_1	0.1333	0.1255	0.0863	0.0475
c_2	−0.1339	−0.1004	−0.0405	−0.0133
c_3	0.1246	0.0535	0.0107	0.0020
c_4	−0.0781	−0.0132	−0.0012	−0.0001
sd	7.13×10^{-7}	2.31×10^{-5}	7.98×10^{-5}	3.30×10^{-3}
$E(5\pm1)$				
c_0	−6.2500	−6.2516	−6.2926	−6.4600
c_1	−3.3333	−3.3164	−3.1660	−2.8713
c_2	0.8101	0.7406	0.5235	0.3243
c_3	−0.3828	−0.2435	−0.0969	−0.0357
c_4	0.1673	0.0480	0.0091	0.0019
sd	7.19×10^{-6}	1.89×10^{-5}	2.83×10^{-4}	2.27×10^{-3}
$E(2\pm2)$				
c_0	5.7500	5.7513	5.7857	5.9293
c_1	2.8928	2.8793	2.7533	2.5007
c_2	−0.6895	−0.6337	−0.4525	−0.2819
c_3	0.3165	0.2053	0.0834	0.0310
c_4	−0.1346	−0.0401	−0.0078	−0.0016
sd	5.75×10^{-6}	2.86×10^{-5}	1.69×10^{-4}	4.91×10^{-3}
$E(3\pm2)$				
c_0	2.7500	2.7504	2.7609	2.8052
c_1	0.9167	0.9125	0.8741	0.7963
c_2	−0.2135	−0.1965	−0.1411	−0.0886
c_3	0.0969	0.0630	0.0258	0.0097
c_4	−0.0411	−0.0123	−0.0024	−0.0005
sd	4.80×10^{-6}	4.59×10^{-5}	2.53×10^{-4}	1.97×10^{-3}
$E(4\pm2)$				
c_0	−1.2500	−1.2503	−1.2590	−1.2995
c_1	−0.8928	−0.8900	−0.8583	−0.7874
c_2	0.1903	0.1789	0.1339	0.0862
c_3	−0.0758	−0.0538	−0.0239	−0.0093
c_4	0.0280	0.0100	0.0022	0.0005
sd	5.75×10^{-6}	1.67×10^{-5}	1.89×10^{-4}	2.79×10^{-3}
$E(5\pm2)$				
c_0	−6.2500	−6.2514	−6.2875	−6.4350
c_1	−2.9166	−2.9018	−2.7691	−2.5096
c_2	0.7127	0.6513	0.4598	0.2844
c_3	−0.3376	−0.2146	−0.0853	−0.0313
c_4	0.1477	0.0424	0.0080	0.0016
sd	5.84×10^{-6}	2.86×10^{-5}	1.69×10^{-4}	4.91×10^{-3}

(a) $S_1 = S_2 = 1/2$

$$\langle 1 \quad \pm 1 | \hat{H} | 1 \quad \pm 1 \rangle = -(\alpha/4)J,$$

$$\langle 1 \quad 0 | \hat{H} | 1 \quad 0 \rangle = (\alpha/4 - \beta/2)J,$$

$$\langle 0 \quad 0 | \hat{H} | 0 \quad 0 \rangle = (\alpha/4 + \beta/2)J.$$

(b) $S_1 = S_2 = 1$

$$\langle 2 \quad \pm 2 | \hat{H} | 2 \quad \pm 2 \rangle = -\alpha J,$$

$$\langle 2 \quad \pm 1 | \hat{H} | 2 \quad \pm 1 \rangle = -\beta J,$$

$$\langle 1 \quad \pm 1 | \hat{H} | 1 \quad \pm 1 \rangle = -\beta J,$$

$$\langle 2 \quad 0 | \hat{H} | 2 \quad 0 \rangle = (\alpha/3 - 4\beta/3)J,$$

$$\langle 1 \quad 0 | \hat{H} | 1 \quad 0 \rangle = \alpha J,$$

$$\langle 0 \quad 0 | \hat{H} | 0 \quad 0 \rangle = (2\alpha/3 + 4\beta/3)J,$$

$$\langle 2 \quad 0 | \hat{H} | 0 \quad 0 \rangle$$
$$= \langle 0 \quad 0 | \hat{H} | 2 \quad 0 \rangle = (\sqrt{2}/3)(\alpha - \beta)J.$$

(c) $S_1 = S_2 = 3/2$

$$\langle 3 \quad \pm 3 | \hat{H} | 3 \quad \pm 3 \rangle = -(9\alpha/4)J,$$

$$\langle 3 \quad \pm 2 | \hat{H} | 3 \quad \pm 2 \rangle = (-3\alpha/4 - 3\beta/2)J,$$

$$\langle 2 \quad \pm 2 | \hat{H} | 2 \quad \pm 2 \rangle = (-3\alpha/4 + 3\beta/2)J,$$

$$\langle 3 \quad \pm 1 | \hat{H} | 3 \quad \pm 1 \rangle = (3\alpha/20 - 12\beta/5)J,$$

$$\langle 2 \quad \pm 1 | \hat{H} | 2 \quad \pm 1 \rangle = (3\alpha/4)J,$$

$$\langle 1 \quad \pm 1 | \hat{H} | 1 \quad \pm 1 \rangle = (7\alpha/20 + 12\beta/5)J,$$

$$\langle 3 \quad \pm 1 | \hat{H} | 1 \quad \pm 1 \rangle$$
$$= \langle 1 \quad \pm 1 | \hat{H} | 3 \quad \pm 1 \rangle = (\sqrt{6}/5)(\alpha - \beta)J,$$

$$\langle 3 \quad 0 | \hat{H} | 3 \quad 0 \rangle = (9\alpha/20 - 27\beta/10)J,$$

$$\langle 2 \quad 0 | \hat{H} | 2 \quad 0 \rangle = (5\alpha/4 - \beta/2)J,$$

$$\langle 1 \quad 0 | \hat{H} | 1 \quad 0 \rangle = (41\alpha/20 + 7\beta/10)J,$$

$$\langle 0 \quad 0 | \hat{H} | 0 \quad 0 \rangle = (5\alpha/4 + 5\beta/2)J,$$

$$\langle 3 \quad 0 | \hat{H} | 1 \quad 0 \rangle = \langle 1 \quad 0 | \hat{H} | 3 \quad 0 \rangle = (3/5)(\alpha - \beta)J,$$

$$\langle 2 \quad 0 | \hat{H} | 0 \quad 0 \rangle = \langle 0 \quad 0 | \hat{H} | 2 \quad 0 \rangle = (\alpha - \beta)J.$$

(d) $S_1 = S_2 = 2$

$$\langle 4 \quad \pm 4 | \hat{H} | 4 \quad \pm 4 \rangle = -4J,$$

$$\langle 4 \quad \pm 3 | \hat{H} | 4 \quad \pm 3 \rangle = -2(\alpha + \beta)J,$$

$$\langle 3 \quad \pm 3 | \hat{H} | 3 \quad \pm 3 \rangle = -2(\alpha - \beta)J,$$

$$\langle 4 \quad \pm 2 | \hat{H} | 4 \quad \pm 2 \rangle = -(4\alpha/7 + 24\beta/7)J,$$

$$\langle 3 \quad \pm 2 | \hat{H} | 3 \quad \pm 2 \rangle = 0,$$

$$\langle 2 \quad \pm 2 | \hat{H} | 2 \quad \pm 2 \rangle = -(3\alpha/7 - 24\beta/7)J,$$

$$\langle 4 \quad \pm 2 | \hat{H} | 2 \quad \pm 2 \rangle$$
$$= \langle 2 \quad \pm 2 | \hat{H} | 4 \quad \pm 2 \rangle = (2\sqrt{3}/7)(\alpha - \beta)J,$$

$$\langle 4 \quad \pm 1 | \hat{H} | 4 \quad \pm 1 \rangle = (2\alpha/7 - 30\beta/7)J,$$

$$\langle 3 \quad \pm 1 | \hat{H} | 3 \quad \pm 1 \rangle = (6/5)(\alpha - \beta)J,$$

$\langle 2 \quad \pm 1 |\hat{H}| 2 \quad \pm 1 \rangle = (12\alpha/7 + 9\beta/7)J,$

$\langle 1 \quad \pm 1 |\hat{H}| 1 \quad \pm 1 \rangle = (4\alpha/5 + 21\beta/5)J,$

$\langle 4 \quad \pm 1 |\hat{H}| 2 \quad \pm 1 \rangle$
$\quad = \langle 2 \quad \pm 1 |\hat{H}| 4 \quad \pm 1 \rangle = (2\sqrt{6}/7)(\alpha - \beta)J,$

$\langle 3 \quad \pm 1 |\hat{H}| 1 \quad \pm 1 \rangle$
$\quad = \langle 1 \quad \pm 1 |\hat{H}| 3 \quad \pm 1 \rangle = (2\sqrt{6}/5)(\alpha - \beta)J,$

$\langle 4 \quad 0 |\hat{H}| 4 \quad 0 \rangle = (4\alpha/7 - 32\beta/7)J,$

$\langle 3 \quad 0 |\hat{H}| 3 \quad 0 \rangle = (8/5)(\alpha - \beta)J,$

$\langle 2 \quad 0 |\hat{H}| 2 \quad 0 \rangle = (17\alpha/7 + 4\beta/7)J,$

$\langle 1 \quad 0 |\hat{H}| 1 \quad 0 \rangle = (17\alpha/5 + 8\beta/5)J,$

$\langle 0 \quad 0 |\hat{H}| 0 \quad 0 \rangle = (2\alpha + 4\beta)J,$

$\langle 4 \quad 0 |\hat{H}| 2 \quad 0 \rangle$
$\quad = \langle 2 \quad 0 |\hat{H}| 4 \quad 0 \rangle = [12/(7\sqrt{5})](\alpha - \beta)J,$

$\langle 3 \quad 0 |\hat{H}| 1 \quad 0 \rangle$
$\quad = \langle 1 \quad 0 |\hat{H}| 3 \quad 0 \rangle = (6/5)(\alpha - \beta)J,$

$\langle 2 \quad 0 |\hat{H}| 0 \quad 0 \rangle$
$\quad = \langle 0 \quad 0 |\hat{H}| 2 \quad 0 \rangle = \sqrt{14}/5(\alpha - \beta)J.$

(e) $S_1 = S_2 = 5/2$

$\langle 5 \quad \pm 5 |\hat{H}| 5 \quad \pm 5 \rangle = (-25\alpha/4)J,$

$\langle 5 \quad \pm 4 |\hat{H}| 5 \quad \pm 4 \rangle = (-15\alpha/4 - 5\beta/2)J,$

$\langle 4 \quad \pm 4 |\hat{H}| 4 \quad \pm 4 \rangle = (-15\alpha/4 + 5\beta/2)J,$

$\langle 5 \quad \pm 3 |\hat{H}| 5 \quad \pm 3 \rangle = (-65\alpha/36 - 40\beta/9)J,$

$\langle 4 \quad \pm 3 |\hat{H}| 4 \quad \pm 3 \rangle = -(5\alpha/4)J,$

$\langle 3 \quad \pm 3 |\hat{H}| 3 \quad \pm 3 \rangle = (-61\alpha/36 + 40\beta/9)J,$

$\langle 5 \quad \pm 3 |\hat{H}| 3 \quad \pm 3 \rangle$
$\quad = \langle 3 \quad \pm 3 |\hat{H}| 5 \quad \pm 3 \rangle = 2\sqrt{5}/9(\alpha - \beta)J,$

$\langle 5 \quad \pm 2 |\hat{H}| 5 \quad \pm 2 \rangle = (-5\alpha/12 - 35\beta/6)J,$

$\langle 4 \quad \pm 2 |\hat{H}| 4 \quad \pm 2 \rangle = (15\alpha/28 - 25\beta/14)J,$

$\langle 3 \quad \pm 2 |\hat{H}| 3 \quad \pm 2 \rangle = (11\alpha/12 + 11\beta/6)J,$

$\langle 2 \quad \pm 2 |\hat{H}| 2 \quad \pm 2 \rangle = (-\alpha/28 + 81\beta/14)J,$

$\langle 5 \quad \pm 2 |\hat{H}| 3 \quad \pm 2 \rangle$
$\quad = \langle 3 \quad \pm 2 |\hat{H}| 5 \quad \pm 2 \rangle = \sqrt{5}/3(\alpha - \beta)J,$

$\langle 4 \quad \pm 2 |\hat{H}| 2 \quad \pm 2 \rangle$
$\quad = \langle 2 \quad \pm 2 |\hat{H}| 4 \quad \pm 2 \rangle = 3\sqrt{5}/7(\alpha - \beta)J,$

$\langle 5 \quad \pm 1 |\hat{H}| 5 \quad \pm 1 \rangle = (5\alpha/12 - 20\beta/3)J,$

$\langle 4 \quad \pm 1 |\hat{H}| 4 \quad \pm 1 \rangle = (45\alpha/28 - 20\beta/7)J,$

$\langle 3 \quad \pm 1 |\hat{H}| 3 \quad \pm 1 \rangle = (149\alpha/60 + 4\beta/15)J,$

$\langle 2 \quad \pm 1 |\hat{H}| 2 \quad \pm 1 \rangle = (81\alpha/28 + 20\beta/7)J,$

$\langle 1 \quad \pm 1 |\hat{H}| 1 \quad \pm 1 \rangle = (27\alpha/20 + 32\beta/5)J,$

$\langle 5 \quad \pm 1 |\hat{H}| 3 \quad \pm 1 \rangle$
$\quad = \langle 3 \quad \pm 1 |\hat{H}| 5 \quad \pm 1 \rangle = 5\sqrt{2/63}(\alpha - \beta)J,$

$\langle 4 \quad \pm 1 |\hat{H}| 2 \quad \pm 1 \rangle$
$\quad = \langle 2 \quad \pm 1 |\hat{H}| 4 \quad \pm 1 \rangle = 3\sqrt{10}/7(\alpha - \beta)J,$

$\langle 3 \quad \pm 1 |\hat{H}| 1 \quad \pm 1 \rangle$
$\quad = \langle 1 \quad \pm 1 |\hat{H}| 3 \quad \pm 1 \rangle = 36/(5\sqrt{21})(\alpha - \beta)J,$

$\langle 5 \quad 0 |\hat{H}| 5 \quad 0 \rangle = (25\alpha/36 - 125\beta/18)J,$

$\langle 4 \quad 0 |\hat{H}| 4 \quad 0 \rangle = (55\alpha/28 - 45\beta/14)J,$

$\langle 3 \quad 0 |\hat{H}| 3 \quad 0 \rangle = (541\alpha/180 - 23\beta/90)J,$

$\langle 2 \quad 0 |\hat{H}| 2 \quad 0 \rangle = (325\alpha/84 + 79\beta/42)J,$

$\langle 1 \quad 0 |\hat{H}| 1 \quad 0 \rangle = (101\alpha/20 + 27\beta/10)J,$

$\langle 0 \quad 0 |\hat{H}| 0 \quad 0 \rangle = (35\alpha/12 + 35\beta/6)J,$

$\langle 5 \quad 0 |\hat{H}| 3 \quad 0 \rangle$
$\quad = \langle 3 \quad 0 |\hat{H}| 5 \quad 0 \rangle = [(10/9)\sqrt{5/7}](\alpha - \beta)J,$

$\langle 4 \quad 0 |\hat{H}| 2 \quad 0 \rangle$
$\quad = \langle 2 \quad 0 |\hat{H}| 4 \quad 0 \rangle = [(18/7)\sqrt{1/3}](\alpha - \beta)J,$

$\langle 3 \quad 0 |\hat{H}| 1 \quad 0 \rangle$
$\quad = \langle 1 \quad 0 |\hat{H}| 3 \quad 0 \rangle = (36/5)\sqrt{1/14}(\alpha - \beta)J,$

$\langle 2 \quad 0 |\hat{H}| 0 \quad 0 \rangle$
$\quad = \langle 0 \quad 0 |\hat{H}| 2 \quad 0 \rangle = 2\sqrt{14}/3(\alpha - \beta)J.$

Appendix D

Eigenvalues (in unit of J) of the Hamiltonian $\hat{H}_{\text{iso/aniso}} = -J[\alpha \hat{S}_{1z}\hat{S}_{2z} + \beta(\hat{S}_{1x}\hat{S}_{2x} + \hat{S}_{1y}\hat{S}_{2y})]$ (Table 27).

Table 27

Character	E	$(\alpha=1, \beta=0)$	$(\alpha=\beta=1)$	$(\alpha=0, \beta=1)$
(a) $S_1 = S_2 = 1/2$				
$\lvert 1\pm 1\rangle$	$-\alpha/4$	$-1/4$	$-1/4$	0
$\lvert 1\ \ 0\rangle$	$\alpha/4 - \beta/2$	$1/4$	$-1/4$	$-1/2$
$\lvert 0\ \ 0\rangle$	$\alpha/4 + \beta/2$	$1/4$	$3/4$	$1/2$
(b) $S_1 = S_2 = 1$				
$\lvert 2\pm 2\rangle$	$-\alpha$	-1	-1	0
$\lvert 2\pm 1\rangle$	$-\beta$	0	-1	-1
$\lvert 1\pm 1\rangle$	β	0	1	1
$\lvert 2\ \ 0\rangle$ & $\lvert 0\ \ 0\rangle$	$\alpha/2 - \sqrt{9\alpha^2 + 8\alpha\beta + 64\beta^2}/6$	0	-1	$-4/3$
	$\alpha/2 + \sqrt{9\alpha^2 + 8\alpha\beta + 64\beta^2}/6$	1	2	$4/3$
$\lvert 1\ \ 0\rangle$	α	1	1	0
(c) $S_1 = S_2 = 3/2$				
$\lvert 3\pm 3\rangle$	$-9\alpha/4$	$-9/4$	$-9/4$	0
$\lvert 3\pm 2\rangle$	$-3\alpha/4 - 3\beta/2$	$-3/4$	$-9/4$	$-3/2$
$\lvert 2\pm 2\rangle$	$-3\alpha/4 + 3\beta/2$	$-3/4$	$3/4$	$3/2$
$\lvert 2\pm 1\rangle$	$3\alpha/4$	$3/4$	$3/4$	0
$\lvert 3\pm 1\rangle$ & $\lvert 1\pm 1\rangle$	$\alpha/4 - \sqrt{\alpha^2 + 24\beta^2}/2$	$-1/4$	$-9/4$	$-\sqrt{6}$
	$\alpha/4 + \sqrt{\alpha^2 + 24\beta^2}/2$	$3/4$	$11/4$	$\sqrt{6}$
$\lvert 3\ \ 0\rangle$ & $\lvert 1\ \ 0\rangle$	$5\alpha/4 - \beta - \sqrt{4\alpha^2 + 8\alpha\beta + 13\beta^2}/2$	$1/4$	$-9/4$	$-1 - \sqrt{13}/2$
	$5\alpha/4 - \beta + \sqrt{4\alpha^2 + 8\alpha\beta + 13\beta^2}/2$	$9/4$	$11/4$	$-1 + \sqrt{13}/2$
$\lvert 2\ \ 0\rangle$ & $\lvert 0\ \ 0\rangle$	$5\alpha/4 + \beta - \sqrt{4\alpha^2 - 8\alpha\beta + 13\beta^2}/2$	$1/4$	$3/4$	$1 - \sqrt{13}/2$
	$5\alpha/4 + \beta + \sqrt{4\alpha^2 - 8\alpha\beta + 13\beta^2}/2$	$9/4$	$15/4$	$1 + \sqrt{13}/2$
(d) $S_1 = S_2 = 2$				
$\lvert 4\pm 4\rangle$	-4α	-4	-4	0
$\lvert 4\pm 3\rangle$	$-2\alpha - 2\beta$	-2	-4	-2
$\lvert 3\pm 3\rangle$	$-2\alpha + 2\beta$	-2	0	2
$\lvert 3\pm 2\rangle$	0	0	0	0
$\lvert 4\pm 2\rangle$ & $\lvert 2\pm 2\rangle$	$-\alpha/2 - \sqrt{\alpha^2 + 48\beta^2}/2$	-1	-4	$-2\sqrt{3}$
	$-\alpha/2 + \sqrt{\alpha^2 + 48\beta^2}/2$	0	3	$2\sqrt{3}$
$\lvert 4\pm 1\rangle$ & $\lvert 2\pm 1\rangle$	$\alpha - 3\beta/2 - \sqrt{4\alpha^2 + 12\alpha\beta + 33\beta^2}/2$	0	-4	$-3/2 - \sqrt{33}/2$
	$\alpha - 3\beta/2 + \sqrt{4\alpha^2 + 12\alpha\beta + 33\beta^2}/2$	2	3	$-3/2 + \sqrt{33}/2$
$\lvert 3\pm 1\rangle$ & $\lvert 1\pm 1\rangle$	$\alpha + 3\beta/2 - \sqrt{4\alpha^2 - 12\alpha\beta + 33\beta^2}/2$	0	0	$3/2 - \sqrt{33}/2$
	$\alpha + 3\beta/2 + \sqrt{4\alpha^2 - 12\alpha\beta + 33\beta^2}/2$	2	5	$3/2 + \sqrt{33}/2$
$\lvert 4\ \ 0\rangle, \lvert 2\ \ 0\rangle$ & $\lvert 0\ \ 0\rangle$	$5\alpha/3 + n\cos(t + 2\pi/3)$[a]	0	-4	$-\sqrt{22/3}$
	$5\alpha/3 + n\cos(t + 4\pi/3)$[a]	1	3	$-\sqrt{22/3}$
	$5\alpha/3 + n\cos(t)$[a]	4	6	$2\sqrt{22/3}$
$\lvert 3\ \ 0\rangle$ & $\lvert 1\ \ 0\rangle$	$5\alpha/2 - \sqrt{9\alpha^2 + 16\beta^2}/2$	1	0	-2
	$5\alpha/2 + \sqrt{9\alpha^2 + 16\beta^2}/2$	4	5	2

[1] $n = \sqrt{52\alpha^2/9 + 88\beta^2/3}$, $t = \arccos[(280\alpha^3/27 - 424\alpha\beta^2/3)/n^3]/3$.

Character	E	$(\alpha=1, \beta=0)$	$(\alpha=\beta=1)$	$(\alpha=0, \beta=1)$
(e) $S_1 = S_2 = 5/2$				
$\lvert 5\pm 5\rangle$	$-25\alpha/4$	$-25/4$	$-25/4$	0
$\lvert 5\pm 4\rangle$	$-15\alpha/4 - 5\beta/2$	$-15/4$	$-25/4$	$-5/2$
$\lvert 4\pm 4\rangle$	$-15\alpha/4 + 5\beta/2$	$-15/4$	$-5/4$	$5/2$
$\lvert 4\pm 3\rangle$	$-5\alpha/4$	$-5/4$	$-5/4$	0
$\lvert 5\pm 3\rangle$ & $\lvert 3\pm 3\rangle$	$-7\alpha/4 - \sqrt{\alpha^2 + 80\beta^2}/2$	$-9/4$	$-25/4$	$-2\sqrt{5}$
	$-7\alpha/4 + \sqrt{\alpha^2 + 80\beta^2}/2$	$-5/4$	$11/4$	$2\sqrt{5}$

Table 27 (*continued*)

Character	E	$(\alpha = 1,\ \beta = 0)$	$(\alpha = \beta = 1)$	$(\alpha = 0,\ \beta = 1)$
$\lvert 5\pm 2\rangle$ & $\lvert 3\pm 2\rangle$	$\alpha/4 - 2\beta - \sqrt{4\alpha^2 + 16\alpha\beta + 61\beta^2}/2$	$-3/4$	$-25/4$	$-\sqrt{61}/2$
	$\alpha/4 - 2\beta + \sqrt{4\alpha^2 + 16\alpha\beta + 61\beta^2}/2$	$5/4$	$11/4$	$\sqrt{61}/2$
$\lvert 4\pm 2\rangle$ & $\lvert 2\pm 2\rangle$	$\alpha/4 + 2\beta - \sqrt{4\alpha^2 - 16\alpha\beta + 61\beta^2}/2$	$-3/4$	$-5/4$	$-\sqrt{61}/2$
	$\alpha/4 + 2\beta + \sqrt{4\alpha^2 - 16\alpha\beta + 61\beta^2}/2$	$5/4$	$23/4$	$\sqrt{61}/2$
$\lvert 5\pm 1\rangle$, $\lvert 3\pm 1\rangle$ & $\lvert 1\pm 1\rangle$	$17\alpha/12 + n\cos(t + 2\pi/3)$[a]	$-1/4$	$-25/4$	$-\sqrt{46}$
	$17\alpha/12 + n\cos(t + 4\pi/3)$[a]	$3/4$	$11/4$	0
	$17\alpha/12 + n\cos(t)$[b]	$15/4$	$31/4$	$\sqrt{46}$
$\lvert 4\pm 1\rangle$ & $\lvert 2\pm 1\rangle$	$9\alpha/4 - \sqrt{9\alpha^2 + 40\beta^2}/2$	$3/4$	$-5/4$	$-\sqrt{10}$
	$9\alpha/4 + \sqrt{9\alpha^2 + 40\beta^2}/2$	$15/4$	$23/4$	$\sqrt{10}$
$\lvert 5\ \ 0\rangle$, $\lvert 3\ \ 0\rangle$ & $\lvert 1\ \ 0\rangle$	$35\alpha/12 - 3\beta/2 + n\cos(t + 2\pi/3)$[b]	$1/4$	$-25/4$	≈ -7.0812
	$35\alpha/12 - 3\beta/2 + n\cos(t + 4\pi/3)$[b]	$9/4$	$11/4$	≈ -1.0837
	$35\alpha/12 - 3\beta/2 + n\cos(t)$[b]	$25/4$	$31/4$	≈ 3.6449
$\lvert 4\ \ 0\rangle$, $\lvert 2\ \ 0\rangle$ & $\lvert 0\ \ 0\rangle$	$35\alpha/12 + 3\beta/2 + n\cos(t + 2\pi/3)$[c]	$1/4$	$-5/4$	≈ -3.6449
	$35\alpha/12 + 3\beta/2 + n\cos(t + 4\pi/3)$[c]	$9/4$	$23/4$	≈ 1.0837
	$35\alpha/12 + 3\beta/2 + n\cos(t)$[c]	$25/4$	$35/4$	≈ 7.0812

[a] $n = [52\alpha^2/9 + 184\beta^2/3]^{1/2}$, $t = \arccos[(280\alpha^3/27 - 808\alpha\beta^2/3)/n^3]/3$.

[b] $n = [112\alpha^2/9 + 16\alpha\beta + 116\beta^2/3]^{1/2}$, $t = \arccos[(640\alpha^3/27 - 2897\alpha^2\beta/12 + 27\alpha\beta^2/4 - 48\beta^3)/n^3]/3$.

[c] $n = [112\alpha^2/9 - 16\alpha\beta + 116\beta^2/3]^{1/2}$, $t = \arccos[(640\alpha^3/27 + 16\alpha^2\beta - 656\alpha\beta^2/3 + 48\beta^3)/n^3]/3$.

References

[1] J.B. Goodenough, Phys. Rev. B 100 (1955) 564;
J.B. Goodenough, J. Phys. Chem. Solids 6 (1958) 287.

[2] J. Kanamori, J. Phys. Chem. Solids 10 (1959) 87.

[3] P.W. Anderson, Phys. Rev. 115 (1959) 2;
P.W. Anderson, Solid State Phys. 14 (1963) 99.

[4] T. Moriya, Phys. Rev. 120 (1960) 91;
T. Moriya, Phys. Rev. Lett. 4 (1960) 228.

[5] P. Erdös, J. Phys. Chem. Solids 27 (1966) 1705.

[6] N. Uryû, S. Friedberg, Phys. Rev. A 140 (1965) 1803.

[7] J.S. Griffith, Struct. Bonding 10 (1972) 87.

[8] P.J. Hay, J.C. Thibeault, R. Hoffmann, J. Am. Chem. Soc. 97 (1975) 4884.

[9] O. Kahn, B. Briat, J. Chem. Soc. Faraday Trans. II 72 (1976) 268.

[10] L. Noodleman, J. Chem. Phys. 74 (1981) 5737.

[11] L. Noodleman, E.R. Davidson, Chem. Phys. 109 (1986) 131.

[12] A.J.W. Wachters, W.C. Nieupoort, in: E. Clementi (Ed.), Selected topics in Molecular Physics, Verlag-Chemie, Weinheim, 1972, pp. 135–142.

[13] Ph. De Loth, P. Cassoux, J.P. Daudley, J.P. Malrieu, J. Am. Chem. Soc. 103 (1981) 4007.

[14] J. Miralles, J.P. Daudley, R. Caballol, Chem. Phys. Lett. 198 (1992) 555.

[15] J. Miralles, O. Castell, R. Caballol, J.P. Malrieu, Chem. Phys. 172 (1993) 33.

[16] F. Illas, J. Casanovas, M.A. Garcia-Bach, R. Caballol, O. Castell, Phys. Rev. Lett. 71 (1993) 3549.

[17] C. de Graaf, I. de, P.R. Moreira, F. Illas, R.L. Martin, Phys. Rev. B 60 (1999) 3457.

[18] R. Caballol, O. Castel, F. Illas, I. de, P.R. Moreira, J.P. Malrieu, J. Phys. Chem. A 101 (1997) 7860.

[19] A. Bencini, F. Totti, C.A. Daul, K. Doclo, P. Fantucci, V. Barone, Inorg. Chem. 36 (1977) 5022.

[20] F. Illas, R.L. Martin, J. Chem. Phys. 108 (1998) 2519.

[21] A. Chartier, P. D'Arco, R. Dovesi, V.R. Saunders, Phys. Rev. B 60 (1999) 14042 and the references cited therein.

[22] F. Illas, I. de P.R. Moreira, C. de Graaf, V. Barone, Theor. Chem. Acc. 104 (2000) 265.

[23] D. Dai, M.-H. Whangbo, J. Chem. Phys. 114 (2001) 2887.

[24] J.B. Goodenough, Magnetism and the Chemical Bond, Wiley, Cambridge, 1963.

[25] D.C. Johnston, T. Saito, M. Azuma, M. Takano, T. Yamauchi, Y. Ueda, Phys. Rev. B 64 (2001) 134403 and the references cited therein.

[26] H.-J. Koo, M.-H. Whangbo, P.D. VerNooy, C.C. Torardi, W.J. Marshall, Inorg. Chem. 41 (2002) 4664 and the references cited therein.

[27] H.-J. Koo, M.-H. Whangbo, Inorg. Chem. 40 (2001) 2169.

[28] M.-H. Whangbo, H.-J. Koo, D. Dai, D. Jung, Inorg. Chem. 42 (2003) 3898.

[29] R. Hoffmann, J. Chem. Phys. 39 (1963) 1397.

[30] A.P. Ginsberg, Inorg. Chim. Acta Rev. 5 (1971) 45.

[31] W.E. Hatfield, in: E.A. Boudreaux, L.N. Mulay (Eds.), Theory and Applications of Molecular Paramagnetism, Wiley Interscience, New York, 1976, pp. 381–385.

[32] R.M. White, Quantum Theory of Magnetism, McGraw-Hill, New York, 1970.

[33] A. Bencini, D. Gatteschi, EPR of Exchange Coupled Systems, Springer, Berlin, 1990.

[34] O. Kahn, Molecular Magnetism, VCH, New York, 1993.

[35] D. Dai, M.-H. Whangbo, J. Chem. Phys. 118 (2003) 29.

[36] J.C. Slater, Quantum Theory of Atomic Structure, Vol. II, McGraw-Hill, New York, 1960, pp. 87–91.

[37] M. Rotenberg, R. Bivins, N. Metropolis, J.K. Wooten Jr., The 3-j and 6-j Symbols, The Technology Press, MIT, Cambridge, MA, 1959.

[38] J.C. Slater, Quantum Theory of Atomic Structure, Vol. I, McGraw-Hill, New York, 1960, p. 249.

[39] A. Voigt, J. Richter, P. Tomczak, Physica A 299 (2001) 107.

[40] T. Tonegawa, T. Nakao, M. Kaburagi, J. Phys. Soc. Jpn. 65 (1996) 3317.

[41] T. Moriya, in: G.T. Rado, H. Suhl (Eds.), Magnetism, Vol. I, Academic Press, New York, 1963, pp. 85–125.

[42] M.E. Lines, Phys. Rev. 131 (1963) 546.

[43] T. Oguchi, J. Phys. Soc. Jpn. 20 (1965) 2236.
[44] H. Kageyama, K. Yoshimura, K. Kosuge, M. Azuma, M. Takano, H. Mitamura, T. Goto, J. Phys. Soc. Jpn. 66 (1997) 3996.
[45] H. Grime, J.A. Santos, Z. Kristallogr. 88 (1935) 136.
[46] B. Bleany, K.W. Stevens, Rep. Progr. Phys. 16 (1953) 107.
[47] M. Tinkham, Proc. Roy. Soc. (London) A 236 (1956) 549.
[48] A.I. Liechtenstein, M.I. Katsnelson, V.P. Antropov, V.A. Gubanov, J. Mag. Mag. Mater. 67 (1987) 65.
[49] A.I. Liechtenstein, V.I. Anisimov, J. Zaanen, Phys. Rev. B 52 (1995) R5467.
[50] M.A. Korotin, I.S. Elfimov, V.I. Anisimov, M. Troyer, D.I. Khomskii, Phys. Rev. Lett. 83 (1999) 1387.
[51] M.A. Korotin, V.I. Anisimov, T. Saha-Dasgupta, I. Dasgupta, J. Phys.: Condens. Matter 12 (2000) 113.
[52] O.K. Andersen, C. Arcaangeli, R.W. Tank, T. Dasgupta, G. Krier, O.K. Jepsen, I. Dasgupta, in: P.E.A. Turchi, A. Gonis, L. Colombo (Eds.), Tight-Binding Approach to Computational Materials Science, Materials Research Society, Warrendale, 1997, pp. 3–34.
[53] V.I. Anisimov, J. Zaanen, O.K. Andersen, Phys. Rev. B 44 (1991) 943.
[54] B.R. Judd, Operator Techniques in Atomic Spectroscopy, McGraw-Hill, New York, 1963.
[55] M.-H. Whangbo, J. Chem. Phys. 70 (1979) 4963.
[56] T.A. Albright, J.K. Burdett, M.-H. Whangbo, Orbital Interactions in Chemistry, Wiley, New York, 1985 Chapter 8.
[57] N.F. Mott, Metal-Insulator Transitions, 2nd Edition, Taylor & Francis, New York, 1990.
[58] K.I. Kugel, D.I. Khomskii, Sov. Phys. Usp. 25 (1982) 231.
[59] K. Terakura, J. Lee, J. Yu, I.V. Solovyev, H. Sawada, Mater. Sci. Eng. B 63 (1999) 11 and the references cited therein.
[60] M.-H. Whangbo, H.-J. Koo, Solid State Sci. 4 (2002) 335.
[61] P. Tola, O. Kahn, C. Chauvel, H. Coudanne, Nouv. J. Chim. 1 (1977) 467.
[62] M.-H. Whangbo, H.B. Schlegel, S. Wolfe, J. Am. Chem. Soc. 99 (1977) 1296.
[63] M.F. Charlot, O. Kahn, Nouv. J. Chim. 4 (1980) 567.
[64] H.-J. Koo, M.-H. Whangbo, S. Coste, S. Jobic, J. Solid State Chem. 156 (2001) 464.
[65] D. Dai, H.-J. Koo, M.-H. Whangbo, in: M.J. Geselbracht, J.E. Greedan, D.C. Johnson and M.A. Subramanian (Eds.), Materials Research Society, Vol. 658, Warrendale, PA, 2001, GG5.3.1-5.3.11, MRS Symposium Proceedings.
[66] M.-H. Whangbo, H.-J. Koo, D. Dai, D. Jung, Inorg. Chem. 41 (2002) 5575.
[67] M.-H. Whangbo, H.-J. Koo, J. Dumas, M.A. Continentino, Inorg. Chem. 41 (2002) 2193.
[68] R. Valentí, T. Saha-DasGupta, Phys. Rev. B 65 (2001) 144445.
[69] M.-H. Whangbo, Theor. Chem. Acc. 103 (2000) 252.
[70] M. Wolfsberg, L. Helmholz, J. Chem. Phys. 20 (1952) 837.
[71] C.J. Ballhausen, H.B. Gray, Molecular Orbital Theory, Benjamin, New York, 1965.
[72] J.H. Ammeter, H.-B. Bürgi, J. Thibeault, R. Hoffmann, J. Am. Chem. Soc. 100 (1978) 3686.
[73] M.-H. Whangbo, R. Hoffmann, J. Chem. Phys. 68 (1978) 5498.
[74] E. Clementi, C. Roetti, Atomic Data Nucl. Data Tables 14 (1974) 177.
[75] A.D. McLean, R.S. McLean, Atomic Data Nuclear Data Tables 26 (1981) 197.
[76] J.M. Williams, J.R. Ferraro, R.J. Thorn, K.D. Carlson, U. Geiser, H.H. Wang, A.M. Kini, M.-H. Whangbo, Organic Superconductors, Prentice Hall, New York, 1992.
[77] C. Sousa, J. Casanovas, J. Rubio, F. Illas, J. Comp. Chem. 14 (1993) 680 and references cited therein.
[78] E. Canadell, M.-H. Whangbo, Chem. Rev. 91 (1991) 965 and the references cited therein.
[79] Z.-T. Zhu, J.M. Musfeldt, H.-J. Koo, M.-H. Whangbo, Z.S. Teweldemedhin, M. Greenblatt, Chem. Mater. 14 (2002) 2607.
[80] E. Sandré, P. Foury-Leylekian, S. Ravy, J.-P. Pouget, Phys. Rev. Lett. 86 (2001) 5100.
[81] H.-J. Koo, M.-H. Whangbo, J. Dong, I. Olejniczak, J.L. Musfeldt, J.A. Schlueter, U. Geiser, Solid State Commun. 112 (1999) 403.
[82] M.-H. Whangbo, H.-J. Koo, Inorg. Chem. 41 (2002) 3570.
[83] E. Wimmer, in: J.K. Labanowski, J.W. Andzelm (Eds.), Density Functional Methods in Chemistry, Springer-Verlag, New York, 1991 Chapter 2.
[84] S. Jobic, R. Brec, A. Pasturel, H.-J. Koo, M.-H. Whangbo, J. Solid State Chem. 162 (2001) 63.
[85] M.-H. Whangbo, H.-J. Koo, A. Villesuzanne, M. Pouchard, Inorg. Chem. 41 (2002) 1920.
[86] M.-H. Whangbo, H.-J. Koo, D. Dai, A. Villesuzanne, J. Solid State Chem. 165 (2002) 345.
[87] I. de, P.R. Moreiro, F. Illas, Phys. Rev. B 60 (1999) 5179.
[88] J. Casanovas, F. Illas, J. Chem. Phys. 100 (1994) 8257.
[89] J. Casanovas, J. Rubio, F. Illas, Phys. Rev. B 53 (1996) 945.
[90] I. de, P.R. Moreiro, F. Illas, C.J. Calzado, J.F. Sanz, J.-P. Malrieu, N.B. Amor, D. Maynau, Phys. Rev. B 59 (1999) 6593.
[91] A.B. van Oosten, R. Broer, W.C. Nieuwpoort, Chem. Phys. Lett. 257 (1996) 207.
[92] M.E. Lines, Phys. Rev. 164 (1967) 736.
[93] L.J. de Jongh, R. Miedema, Adv. Phys. 23 (1974) 1.
[94] S. Katoda, I. Yamada, S. Yoneyama, K. Hirakawa, J. Phys. Soc. Jpn. 23 (1967) 751.
[95] M.T. Hutchings, E.J. Samuelson, G. Shirane, K. Hirakawa, Phys. Rev. 188 (1969) 919.
[96] S.K. Satija, J.D. Axe, G. Shirane, H. Yonezawa, K. Hirakawa, Phys. Rev. B 21 (1980) 2001.
[97] I. Yamada, J. Phys. Soc. Jpn. 33 (1972) 979.
[98] K. Hirakawa, H. Ikeda, J. Phys. Soc. Jpn. 35 (1973) 1328.
[99] R.R.P. Singh, P.A. Fleury, K.B. Lyons, P.E. Sulewski, Phys. Rev. Lett. 62 (1989) 2736.
[100] G. Aeppli, S.M. hayden, H.A. Mook, Z. Fisk, S.-W. Cheong, D. Rytz, J.P. Remeika, G.P. Espinosa, A.S. Cooper, Phys. Rev. Lett. 62 (1989) 2052.
[101] K. Knox, Acta Cryst. 14 (1961) 583.
[102] D. Balz, Naturwiss. 40 (1953) 241.
[103] E. Herdtweck, D. Babel, Z. anorg. Allg. Chem. 474 (1981) 113.
[104] B. Grande, Hk. Müller-Buschbaum, M. Schweitzer, Z. anorg. Allg. Chem. 428 (1977) 120.
[105] R.H. Buttner, E.N. Maslen, N. Spadaccini, Acta Cryst. B 46 (1990) 131.
[106] P. Núñez, T. Roisnel, J. Solid State Chem. 124 (338) (1996) 21.
[107] D.R. Sears, J.L. Hoard, J. Chem. Phys. 50 (1969) 1066.
[108] J. Pebler, W. Massa, H. Lass, B. Ziegler, J. Solid State Chem. 71 (1987) 87.
[109] W. Massa, Acta Crystallogr. C 42 (1986) 644.
[110] S. Emori, M. Inoue, M. Kishita, M. Kubo, Inorg. Chem. 8 (1969) 1385.
[111] C.D. Ling, J.J. Neumeier, D.N. Argyriou, J. Solid State Chem. 160 (2000) 167.
[112] R.S. Eccleston, T. Barnes, J. Brody, J.W. Johnson, Phys. Rev. Lett. 73 (1994) 2626.
[113] T. Barnes, J. Riera, Phys. Rev. B 50 (1994) 6817.
[114] A.W. Garret, S.E. Nagler, D.A. Tennant, B.C. Sales, T. Barnes, Phys. Rev. Lett. 79 (1997) 745.
[115] D.C. Johnston, J.W. Johnson, D.P. Goshorn, A.J. Jacobson, Phys. Rev. B 35 (1987) 219.
[116] J. Kikuchi, K. Motoya, T. Yamauchi, Y. Ueda, Phys. Rev. B 60 (1999) 6731.

[117] H.-J. Koo, M.-H. Whangbo, Inorg. Chem. 39 (2000) 3599.

[118] S. Geupel, K. Pilz, S. van Smaalen, F. Büllesfeld, A. Prokofiev, W. Assmus, Acta Crystallogr. C 58 (2002) i9.

[119] J.W. Johnson, D.C. Johnston, A.J. Jacobson, J.F. Brody, J. Am. Chem. Soc. 106 (1984) 8123.

[120] D.A. Tennant, S.E. Nagler, A.W. Garrett, T. Barnes, C.C. Torardi, Phys. Rev. Lett. 78 (1997) 4998.

[121] B. Lake, D.A. Tennant, R.A. Cowley, J.D. Axe, C.K. Chen, J. Phys.: Condens. Matter 8 (1996) 8613.

[122] H. Ehrenberg, M. Wiesmann, J. Garcia-Jaca, H. Weitzel, H. Fuess, J. Magn. Magn. Mater. 182 (1998) 152.

[123] M. Johnsson, K.W. Törnroos, F. Mila, P. Millet, Chem. Mater. 12 (2000) 2853.

[124] P. Lemmens, K.-Y. Choi, G. Güntherodt, M. Johnsson, P. Millet, F. Mila, R. Valenti, C. Gros, W. Brenig, J. Phys. Chem. Solids 63 (2002) 1115.

[125] P. Lemmens, K.-Y. Choi, E.E. Kaul, C. Geibel, K. Becker, W. Brenig, R. Valenti, C. Gros, M. Johnsson, P. Millet, F. Mila, Phys. Rev. Lett. 87 (2001) 227201.

[126] C.J. O'Connor, Prog. Inorg. Chem. 29 (1982) 203.

[127] D. Dai, M.-H. Whangbo, Our fitting analysis was carried out using the MAGFIT program package, 2003.

[128] H. Masuda, T. Fujino, N. Sato, K. Yamada, J. Solid State Chem. 146 (1999) 336.

[129] M. Wakeshima, Y. Hinatsu, J. Solid State Chem. 153 (2000) 330.

[130] M. Wakeshima, Y. Hinatsu, K. Oikawa, Y. Shimojo, Y. Morii, J. Mater. Chem. 10 (2000) 2183.

[131] H.-J. Koo, M.-H. Whangbo, K.-S. Lee, J. Solid State Chem. 169 (2002) 143.

[132] J.B. Goodenough, J.-S. Zhou, Chem. Mater. 10 (1998) 2980.

[133] K. Terakura, J. Lee, J. Yu, I.V. Solovyev, H. Sawada, Mater. Sci. Eng. B 63 (1999) 11 and the references cited therein.

[134] L.E. Gontchar, A.E. Nikiforov, S.E. Popov, J. Magn. Magn. Mater. 223 (2001) 175.

[135] M.D. Kaplan, B.G. Vekhter, Cooperative Phenomena in Jahn–Teller Crystals, Plenum, New York, 1995.

[136] R.H. Buttner, E.N. Maslen, N. Spadaccini, Acta Cryst. B 46 (1990) 131.

[137] I. Yamada, J. Phys. Soc. Jpn. 33 (1972) 979.

[138] R.A. Gardner, M. Vlasse, A. Wold, Acta Crystallogr. B 25 (1969) 781.

[139] G. Mihály, I. Kézsmárki, F. Zámborsky, M. Miljak, K. Penc, P. Fazekas, H. Berger, L. Forró, Phys. Rev. B 61 (2000) R7831.

[140] M. Ghedira, M. Anne, J. Chenavas, M. Marezio, F. Sayetat, J. Phys. C: Solid State Phys. 19 (1986) 6489 and the papers cited therein.

[141] M. Nakamura, A. Sekiyama, H. Namatame, A. Fujimori, H. Yoshihara, T. Ohtani, A. Misu, M. Takano, Phys. Rev. B 49 (1994) 16191 and the references cited therein.

[142] T. Inami, K. Ohwada, H. Kimura, M. Watanabe, Y. Noda, H. Nakamura, T. Yamasaki, M. Shiga, N. Ikeda, Y. Murakami, Phys. Rev. B 66 (2002) 073108.

[143] S. Fagot, P. Foury-Leylekian, S. Ravy, J.-P. Pouget, Phys. Rev. Lett., submitted for publication.

[144] T. Graf, D. Mandrus, J.M. Lawrence, J.D. Thompson, P.C. Canfield, S.-W. Cheong, L.W. Rupp Jr., Phys. Rev. B 51 (1995) 2037.

[145] H. Nakamura, H. Imai, M. Shiga, Phys. Rev. Lett. 79 (1997) 3779.

[146] H. Nakamura, T. Yamasaki, S. Giri, H. Imai, M. Shiga, K. Kojima, M. Hishi, K. Kakurai, N. Metoki, J. Phys. Soc. Jpn. 69 (2000) 2763.

[147] M.-H. Whangbo, E. Canadell, J. Am. Chem. Soc. 114 (1992) 9587.

[148] L.F. Mattheiss, Solid State Commun. 93 (1995) 791.

[149] M.-H. Whangbo, E. Canadell, P. Foury, J.-P. Pouget, Science 252 (1991) 96.

[150] M.-H. Whangbo, H.-J. Koo, D. Dai, A. Villesuzanne, J. Solid State Chem., in press.

[151] G. Liu, J.E. Greedan, J. Solid State Chem. 103 (1993) 139.

[152] N. Nishiguchi, M. Onoda, K. Kubo, J. Phys.: Condens. Matter 14 (2002) 5731.

[153] Y. Oka, T. Yao, N. Yamamoto, M. Ueda, S. Maegawa, J. Solid State Chem. 149 (2000) 414.

[154] M.-H. Whangbo, H.-J. Koo, K.-S. Lee, Solid State Commun. 114 (2000) 27.

[155] J.-C. Bouloux, J. Galy, Acta Cryst. B 29 (1973) 1335.

[156] G. Liu, J.E. Greedan, J. Solid State Chem. 115 (1995) 174.

[157] Y. Zhang, C.J. Warren, R.C. Haushalter, A. Clearfield, D.-K. Seo, M.-H. Whangbo, Chem. Mater. 10 (1998) 1059.

[158] S. Taniguchi, T. Nishikawa, Y. Yasui, Y. Kobayashi, M. Sato, T. Nishioka, M. Kontani, K. Sano, J. Phys. Soc. Jpn. 64 (1996) 2758.

[159] C.S. Hellberg, W.E. Pickett, L.L. Boyer, H.T. Stokes, M.J. Mehl, J. Phys. Soc. Jpn. 68 (1999) 3489.

[160] H.G. von Schnering, Yu. Grin, M. Kaupp, R.K. Kremer, O. Jepsen, T. Chatterji, M. Weiden, Z. Kristal. New Crystal Struct. 213 (1998) 243.

[161] J.-C. Bouloux, J. Galy, J. Solid State Chem. 16 (1976) 385.

[162] H.-J. Koo, M.-H. Whangbo, J. Solid State Chem. 153 (2000) 263.

[163] A. Carpy, J. Galy, Acta Cryst. B 31 (1975) 1481.

[164] M. Onoda, N. Nishiguchi, J. Solid State Chem. 127 (1996) 359.

[165] J.-C. Bouloux, I. Milosevic, J. Galy, J. Solid State Chem. 16 (1976) 393.

[166] M. Onoda, A. Ohyama, J. Phys.: Condens. Matter 10 (1998) 1229.

[167] Y. Ueda, Chem. Mater. 10 (1998) 2653.

[168] H. Iwase, M. Isobe, Y. Ueda, H. Yasuoka, J. Phys. Soc. Jpn. 65 (1997) 2397.

[169] F. Mila, P. Millet, J. Bonvoisin, Phys. Rev. B 54 (1996) 11925.

[170] H.-J. Koo, M.-H. Whangbo, Solid State Commun. 111 (1999) 353.

[171] S. Miyahara, M. Troyer, D.C. Johnston, K. Ueda, J. Phys. Soc. Jpn. 67 (1998) 3918.

[172] T. Komatsu, N. Kojima, G. Saito, Solid State Commun. 103 (1997) 519;
T. Komatsu, N. Kojima, G. Saito, Synth. Met. 103 (1999) 1923.

[173] T. Nakamura, K. Takahashi, T. Shirahata, M. Uruichi, K. Yakushi, T. Mori, J. Phys. Soc. Jpn. 71 (2002) 2022 and the references cited therein.

[174] B. Domercq, C. Coulon, M. Fourmigué, Inorg. Chem. 40 (2001) 371.

[175] C. Rovira, Chem. Eur. J. 6 (2000) 1723 and the references cited therein.

[176] H. Imai, T. Inabe, Phys. Rev. B 54 (1996) R6838.

[177] P. Zhou, J.E. Drumheller, G.V. Rubenacker, K. Halvorson, R.D. Willet, J. Appl. Phys. 69 (1991) 5804.

[178] H.-J. Koo, M.-H. Whangbo, unpublished results.

[179] M. O'Keeffe, J.-O. Bovin, Am. Mineral. 63 (1978) 180.

[180] J. Pinsard-Gaudart, J. Rodriguez-Carvajal, A. Gukasov, P. Monod, M. Dechamps, J. Jegoudez, Propriétés magnétiques de Cu_4O_3-Un reseau pyrochlore à spin 1/2, presented at Colloque Oxydes à Propriétés Remarquables: Ordre de spins, ordre de charges et phénomènes coopératifs; Organized by C. Berthier, G. Collin and J.-P. Doumerc; Bombannes, June 6–8, 2001. The abstracts of the meeting are collected in the report GDR 2069.

[181] P. Gómez-Romero, E.M. Tejada-Rosales, M.R. Palacín, Angew. Chem. Int. Ed. 38 (1999) 524.

[182] K. Adelsberger, J. Curda, S. Vensky, M. Jansen, J. Solid State Chem. 158 (2001) 82.

[183] E.M. Tejada-Rosales, J. Rodriguez-Carvajal, M.R. Palacin, P. Gómez-Romero, Mater. Sci. Forum 378–381 (2001) 606.

[184] M. O'Keeffe, F.S. Stone, J. Phys. Chem. Solids 23 (1962) 261.

[185] O. Kondo, M. Ono, E. Sugiura, K. Sugiyama, M. Data, J. Phys. Soc. Jpn. 57 (1988) 3293.

[186] U. Köbler, T. Chattopadhyay, Z. Phys. B 82 (1991) 383.

[187] T.I. Arbuzova, A.A. Samokhvalov, I.B. Smolyak, B.V. Karpenko, N.M. Chebotaev, S.V. Naumov, J. Magn. Magn. Mater. 95 (1991) 168.

[188] T.I. Arbuzova, I.B. Smolyak, A.A. Samokhvalov, S.V. Naumov, J. Exp. Theor. Phys. 86 (1998) 559.

[189] J.B. Forsyth, P.J. Brown, B.M. Wanklyn, J. Phys. C: Solid State Phys. 21 (1988) 2917.

[190] P.J. Brown, T. Chattopadhyay, J.B. Forsyth, V. Nunez, F. Tasset, J. Phys. C: Condens. Matter 3 (1991) 4281.

[191] M. Aïn, A. Menelle, B.M. Wanklyn, E.F. Bertaut, J. Phys.: Condens. Matter 4 (1992) 5327.

[192] B.X. Yang, T.R. Thurston, J.M. Tranquada, G. Shirane, Phys. Rev. B 39 (1989) 4343.

[193] T. Tsuda, T. Shimizu, H. Yasuoka, K. Kishio, K. Kitazawa, J. Phys. Soc. Jpn. 57 (1988) 2908.

[194] J. Ziolo, F. Borsa, M. Corti, A. Rigamonti, F. Parmigiani, J. Appl. Phys. 67 (1990) 5864.

[195] T. Shimizu, T. Matsumoto, A. Goto, K. Yoshimura, K. Kosuge, Physica B 259–261 (1999) 573.

[196] J.W. Loram, K.A. Mirza, C.P. Joyce, A.J. Osborne, Europhys. Lett. 8 (1989) 263.

[197] S. Åsbrink, L.-J. Norrby, Acta Crystallogr. B 26 (1970) 8.

[198] H.-J. Koo, M.-H. Whangbo, Inorg. Chem. 42 (2003) 1187.